

LABORATORY STUDIES OF STATIONARY AND NON-STATIONARY STRUCTURES IN FLOWING COMPLEX PLASMAS

By

GARIMA ARORA

PHYS06201504004

Institute for Plasma Research, Gandhinagar

*A thesis submitted to the
Board of Studies in Physical Sciences*

*In partial fulfillment of the requirements
for the Degree of*

DOCTOR OF PHILOSOPHY

of

HOMI BHABHA NATIONAL INSTITUTE



June, 2020



Homi Bhabha National Institute

1. **Name of the Student:** Garima Arora
2. **Name of the Constituent Institution:** Institute for Plasma Research
3. **Enrolment No. :** PHYS06201504004
4. **Title of the Thesis:** Laboratory studies of stationary and non-stationary structures in flowing complex plasma
5. **Board of Studies:** Physical Sciences

Certificate of changes

This is to certify that Ms. Garima Arora has incorporated all the changes in his Ph.D. thesis as per suggestions given by both the, Indian Examiner Prof. Nilakshi Das (Department of Physics, Tezpur University Napaam, Tezpur) and the foreign examiner Dr. Mierk Schwabe (DLR, Germany). She has satisfactorily answered the questions raised by the Indian examiner and the audience during his Thesis Viva-Voce.

Dr. Pintu Bandyopadhyay

(Guide)

CERTIFICATION ON ACADEMIC INTEGRITY

1. I Garima Arora HBNI Enrolment No. PHYS06201504004 hereby undertake that, the Thesis titled "*Laboratory studies of stationary and non-stationary structures in flowing complex plasmas*" is prepared by me and is the original work undertaken by me and free of any plagiarism. That the document has been duly checked through a plagiarism detection tool and the document is plagiarism free.
2. I am aware and undertake that if plagiarism is detected in my thesis at any stage in future, suitable penalty will be imposed as per the applicable guidelines of the Institute/UGC.

Garima

Signature of Student

Endorsed by the thesis Supervisor:

(I certify that the work done by the Researcher is plagiarism free)

Signature

Pintu

Name: Dr. Pintu Bandyopadhyay

Designation: Asso. Professor - E

Department/Centre: Head, Dusty Plasma Section

Name of CI/OCC: Institute for Plasma Research, Gandhinagar

STATEMENT BY AUTHOR

This dissertation has been submitted in partial fulfilment of requirements for an advanced degree at Homi Bhabha National Institute (HBNI) and is deposited in the Library to be made available to borrowers under rules of the HBNI.

Brief quotations from this dissertation are allowable without special permission, provided that accurate acknowledgement of source is made. Requests for permission for extended quotation from or reproduction of this manuscript in whole or in part may be granted by the Competent Authority of HBNI when in his or her judgement the proposed use of the material is in the interests of scholarship. In all other instances, however, permission must be obtained from the author.



GARIMA ARORA

DECLARATION

I, hereby declare that the investigation presented in the thesis has been carried out by me. The work is original and has not been submitted earlier as a whole or in part for a degree/diploma at this or any other Institution/University.

Garima

Garima Arora

List of Publications arising from the thesis

Journals:

- **“Micro-dynamics of neutral flow induced dusty plasma flow”**,
[Garima Arora](#), P. Bandyopadhyay, M. G. Hariprasad, and A. Sen,
Physics of Plasmas (26), 023701 (2019)
- **“A dust particle based technique to measure potential profiles in a plasma”**,
[Garima Arora](#), P. Bandyopadhyay, M. G. Hariprasad, and A. Sen,
Physics of Plasmas (25), 083711 (2018)
- **“Effect of size and shape of a moving charged object on the propagation characteristics of precursor solitons”**,
[Garima Arora](#), P. Bandyopadhyay, M. G. Hariprasad, and A. Sen,
Physics of Plasmas (26), 093701 (2019)
- **“Excitation of dust acoustic shock waves in an in-homogeneous dusty plasma”**,
[Garima Arora](#), P. Bandyopadhyay, M. G. Hariprasad, and A. Sen,
Physics of Plasmas (27), 083703 (2020)

Conferences and Schools

International Participation:

- **Garima Arora**, Pintu Bandyopadhyay, M. G. Hariprasad and Abhijit Sen, “Effect of the size of a charged object on the propagation characteristics of precursor solitons ”, (Poster Presentation)", 46th European Physical Society Conference on Plasma Physics, EPS 2019, University of Milan-Bicocca (UNIMIB), 08-12th July, 2019, Milan (Italy), Italy.

- **Garima Arora**, Pintu Bandyopadhyay, M. G. Hariprasad and Abhijit Sen, “Propagation characteristics of nonlinear dust acoustic waves in inhomogeneous complex plasmas ”, (Poster Presentation) 61st Annual Meeting of the APS Division of Plasma Physics, APS 2019, 21-25th October, 2019, Fort Lauderdale, Florida, USA.
- **Garima Arora**, Pintu Bandyopadhyay, M. G. Hariprasad and Abhijit Sen, “Experimental study of coalescence of two nonlinear DAW waves in flowing dusty plasma ”, (Poster Presentation), 12th International Conference on Plasma Science and Applications, ICPSA 2019, University of Lucknow, 11-14th November, 2019, Lucknow, India.

National Participation:

- **Garima Arora**, Pintu Bandyopadhyay, Abhijit Sen, “Effect of Polarization Force on the Head-On Collision of Two Dust Acoustic Solitary Waves in Complex Plasmas ”, (Poster Presentation) International Symposium on Non Linear Waves in Fluids And Plasmas, Buti fest, Institute of Technology (IIT) Delhi, 03-05th march, 2017, Delhi (Delhi), India.
- **Garima Arora**, Pintu Bandyopadhyay, M. G. Hariprasad and Abhijit Sen, “Dynamics of dust particles in flowing complex plasmas ”, (Poster Presentation) 32nd National Symposium on Plasma Science & Technology, PSSI 2017, Institute for Plasma Research (IPR), 07-10th November, 2017, Gandhinagar (Gujarat), India.
- **Garima Arora**, Pintu Bandyopadhyay, M. G. Hariprasad and Abhijit Sen, “A dust particle based technique to measure the potential profile in a plasmas ”, (Poster Presentation) 33rd National Symposium on Plasma Science & Technology", PSSI 2018, University of Delhi (DU), 04-07th December, 2018, Delhi (Delhi), India.
- **Garima Arora**, Pintu Bandyopadhyay, M. G. Hariprasad and Abhijit Sen, “Excitation of pinned structures in flowing complex plasmas", (Oral Presentation) 34th National Symposium on Plasma Science & Technology", PSSI

2019, Vellore Institute of technology (VIT), Chennai, 03-06th December, 2019, Chennai, India.

- DST-SERB School on Plasma Theory, IASST, Guwahati, India, 9th - 29th November, 2016.
- **Garima Arora**, Pintu Bandyopadhyay, M. G. Hariprasad and Abhijit Sen, "Stationary and dynamic structures in flowing complex plasmas ", (Oral Presentation) 7th PSSI-PLASMA SCHOLARS COLLOQUIUM (PSC-2019), PSC 2019, Institute for Advanced Research ", 08-10th August, 2019, Gandhinagar (Gujarat), India.

Garima

GARIMA ARORA

Dedicated to

my parents, sister and husband...

ACKNOWLEDGEMENTS

First and foremost I want to convey my sincere thanks to all those who supported and guided me during my thesis work. I convey my heartiest gratitude to my thesis supervisor Dr. Pintu Bandyopadhyay for his invaluable guidance, support, and discussions during the entire period of PhD work. His experimental skills, guidance during the experiments made this journey much easier. I am also thankful to him for providing excellent support in laboratory experiments as well as helping me in writing papers. Sir, I am very thankful to you for everything you have done for me.

I am also gratefully thankful to my thesis co-supervisor Prof. Abhijit Sen who has a significant contribution to this thesis for providing me motivational ideas, theoretical background of all my experiments and fruitful suggestions for improving my first draft of each manuscript. He also taught me how to give talks, seminar, writing experimental proposals. His deep insights towards the research problems, tackling problems and good writing skills have always been great source of inspiration and I cant imagine my Ph.D journey without him.

I am obliged to all my doctoral committee members Prof. Shishir P. Deshpande, Prof. Prabal K. Chattopadhyay, Dr. Joydeep Ghosh and Dr. Devendra Sharma for their valuable discussions and suggestions during annual academic reviews.

I would like to thank Dr. Subroto Mukherjee, Dr. Prabal Kumar Chattopadhyay, Prof. Sudip Sengupta, Dr. Mrityunjay Kundu, Dr. R. Ganesh, Dr. Devendra Sharma, Dr. N. Ramasubramanian, Dr. G. Ravi, Dr. V. P. Anitha, Dr. S. K. Pathak, Dr. Shantanu Kumar Karkari, Dr. Asim Kumar Chattopadhyay, Dr. Nir-mal K Bisai, and Dr. P. V. Subhash, for teaching me plasma physics and support during my first-year course-work at IPR.

I also want to thank the library staff, computer centre staff and administrative staff and of IPR for their cooperation. I want to convey my thanks to workshop, drafting staff especially Prajapati ji and stores staff for their support during my entire PhD tenure. I would also like to thank Mrs. Minsha Shah for her help in designing and developing the necessary electronic circuits for my experiments.

I thank my seniors Dr. Arun Pandey, Dr. Sandeep Shukla, Dr. Sonu Yadav, Dr. Umesh Shukla, Dr. Debraj Mondal , Dr. Akanksha Gupta, Dr. Vidhi Goel, Dr.

Vara Prasad, Dr. Neeraj Chaubey, Dr. Bibhu Sahoo, Dr. Mangilal Chaudhary, Dr. Deepa Verma, Dr. Ratan, Dr. Arghya, Dr. Bhumika, Dr. Amit Patel, Dr. Narayan Behra, Ms. Meenakshee, Dr. Prabhakar, Dr. Pallavi and all other IPR scholars for their help whenever I needed and making friendly environment at IPR campus.

I am very thankful to my friends Srimanta, Preeti, Dipshika, Neeraj, Mayank, Peeyush, Neha, Arun, Arnab for their best wishes and care. I want to thank my colleagues Hari, Krishan, Saravanan, Swarnima for their constant support and discussion with them.

I would also like to acknowledge DST and HBNI for granting me travel support to attend international conference and IPR for providing me fund to attend national schools and conferences during my Ph.D tenure.

Finally, I want to give my deep thanks to my mother Sunita Arora and father Kanwaljeet Arora and my sweet sister Gitika Arora for their blessings and constant moral support to achieve my goal. I am grateful to my husband Dr. Srimanta Maity for his love and support and for always being with me in happy, bad and frustrating days.

Contents

Summary	vii
List of Figures	ix
List of Tables	xix
1 Introduction	1
1.1 Introduction and Motivation	1
1.2 Characteristics of dusty or complex plasma	9
1.2.1 Typical length scales	9
1.2.1.1 Debye length	10
1.2.1.2 Radius of dust particle	10
1.2.1.3 Inter-particle distance	11
1.2.2 Typical time scales	11
1.2.2.1 Dust plasma frequency	11
1.2.2.2 Collisional frequency	12
1.2.3 Dust charge	12
1.2.4 Dust surface potential	13
1.2.4.1 Orbital Motion Limited (OML) theory	14
1.2.4.2 Collision Enhanced plasma Collection (CEC) theory	15
1.2.5 Quasi-neutrality condition	15
1.2.6 Coulomb coupling parameter	16
1.2.7 Forces on dust particles	17
1.2.7.1 Electromagnetic force (\vec{F}_{EB})	17
1.2.7.2 Gravitational force (\vec{F}_g)	18
1.2.7.3 Ion Drag force (\vec{F}_{id})	18
1.2.7.4 Neutral drag force (\vec{F}_{nd})	19
1.2.7.5 Thermophoretic force (\vec{F}_{th})	20
1.2.7.6 Radiation pressure force (\vec{F}_{rad})	21
1.2.7.7 Polarization force (\vec{F}_p)	21
1.3 An overview of earlier works	22
1.4 Scope and outline of this thesis	27

2	Experimental set-up, production and characterization of plasma and dusty plasma	31
2.1	Experimental set-up	32
2.1.1	Vacuum chamber	33
2.1.2	Pumping and gas feeding system	34
2.1.3	Powered electrodes	35
2.1.4	Confining strips	36
2.1.5	Plasma discharge power supply	37
2.1.6	Dust particles	37
2.1.7	Dust dispenser	38
2.2	Diagnostics of plasma	39
2.2.1	Langmuir probe	39
2.2.2	Emissive probe	40
2.3	Diagnostics of dusty plasma	42
2.3.1	Imaging of dust particles	43
2.3.2	Data storage and analysis	44
2.4	Plasma production and its characterization	45
2.5	Characterization of plasma	45
2.5.1	Measurements of radial profile by Langmuir probe	49
2.5.2	Distribution function	51
2.5.3	Measurements of plasma potential and floating potential by emissive probe	53
2.6	Characterization of dusty plasma	57
2.6.1	Mass	60
2.6.2	Charge	61
2.6.3	Inter-particle distance and dust density	64
2.6.4	Temperature	64
2.6.5	Coulomb coupling parameter	65
2.7	Flow generation	65
2.7.1	Single Gas Injection (SGI) technique	66
2.7.2	Dual Gas Injection (DGI) technique	66
2.7.3	Altering potential hill technique	67
2.8	Measurements of flow velocities	69
2.8.1	Particle Image Velocimetry (PIV)	69

2.8.2	super Particle Identification Tracking (sPIT)	71
2.9	Conclusions	72
3	Dynamics of dust particles in a flowing dusty plasma	75
3.1	Introduction	75
3.2	Experimental Set-up and procedure	77
3.3	Flow generation and velocity measurements	78
3.4	Results and discussion	80
3.4.1	Influence of gas flow rate	80
3.4.2	Influence of background pressure	83
3.4.3	Influence of size of dust particle	83
3.4.4	Influence of neutral particles	86
3.5	Estimation of various forces	87
3.5.1	Coulomb force:	88
3.5.2	Ion drag force:	89
3.5.3	Neutral streaming force:	90
3.6	Theoretical model	91
3.7	Conclusions	94
4	Measurement of potential profiles around a charged object	97
4.1	Introduction	97
4.2	Experimental set-up and procedure	101
4.3	Results and discussion	103
4.3.1	Generation of flow and closest approach	103
4.3.2	Particle trajectory	105
4.3.3	Variation of size of the potential hill with discharge parameters	106
4.3.4	Energy conservation and estimation of potential	107
4.3.5	Estimation of radial and axial potential profiles around the charged object	111
4.4	Conclusion	113
5	Excitation of precursor solitons, its dependence on the shape and the size of the charged object	115
5.1	Introduction	115
5.2	Experimental set-up and procedure	118

5.2.1	Generation of flow in the dust fluid	121
5.3	Results and Discussion	122
5.3.1	Excitation of precursor solitons and wakes	122
5.3.2	Theoretical model for the precursor solitons	124
5.3.3	Effect of size of charged object on the excitation of precursor solitons	126
5.3.4	Effect of shape of charged object on the excitation of precursor solitons	131
5.4	Conclusions	135
6	Excitation of pinned solitons	139
6.1	Introduction	139
6.2	Experimental set-up and procedure	142
6.3	Results and discussion	147
6.3.1	Excitation of pinned solitons and wakes	147
6.3.2	Time evolution of the pinned solitons and wakes	149
6.3.3	Comparison with model f-KdV equation	151
6.4	Conclusions	154
7	Excitation of shock waves in an inhomogeneous dusty plasma	157
7.1	Introduction	157
7.2	Experimental set-up and procedure	160
7.3	Creation of an inhomogeneous dusty plasma	162
7.4	Excitation of Dust Acoustic Shock Waves	165
7.5	Experimental Results	167
7.5.1	Characterisation of Dust Acoustic Shock Waves	167
7.5.2	Merging of two shock fronts	171
7.5.3	Modification on the propagation characteristics of DASWs due to dust density inhomogeneity	172
7.6	Theoretical Modelling	176
7.7	Conclusions	182
8	Summary and Future Scope	185
8.1	Summary	185
8.2	Future Scope	193

Bibliography

197

List of Figures

1.1	Picture representing the explosion of solar nebulae. Credit: Hernan Canellas.	3
1.2	Spokes observed in Saturn's ring as seen by Voyagers 2. Credit: Cassini Imaging Team.	4
2.1	A schematic of the experimental set up for performing flowing dusty plasma experiments. Ports P1 and P2 are used for Gas feeding. Port P3 is used either for installation of different probes or Gauge. Port P4 is used to attach Dust Dispenser. Port P5 is made for Pumping port and used to attach the rotary pump. Gauges are attached in Ports P6 and P8. Anode is hung axially through Port P7. Ports P9 and P11 are closed. Port P10 is used for cathode insertion and for shining the laser axially.	33
2.2	Schematic of (a) anode and (b) cathode electrodes used to generate the plasma	35
2.3	Photograph of Langmuir probe exposing the tip only and covered with ceramic is shown.	40
2.4	A schematic of the Langmuir probe circuit.	40
2.5	A photograph of emissive probe used in the experiments.	41
2.6	A schematic diagram of emissive probe circuit operated in floating-point technique.	42
2.7	The ideal I-V characteristics of Langmuir probe.	46

2.8	Variation of (a) bias voltage applied to the probe (b) current drawn by the probe with time. (c) Typical characteristics of a Single Langmuir probe.	47
2.9	A plot showing the variation of floating potential and plasma potential with discharge voltage.	48
2.10	A plot showing the variation of plasma density and electron temperature with background pressure.	49
2.11	A plot of plasma density and electron temperature for different discharge voltages.	50
2.12	A plot of plasma density and electron temperature at different radial locations.	50
2.13	A plot of electron energy probability distribution function (EEPF) for $p = 14$ Pa and $V = 300$ V	51
2.14	Maxwell, Druyvesteyn and experimentally obtained distribution functions.	53
2.15	Measurement of plasma potential using emissive probe by floating point technique.	54
2.16	Radial profile of plasma potential for three different pressure and discharge voltage 360 V.	55
2.17	Radial profile of plasma potential for three different discharge voltages and fixed background pressure 14 Pa.	56
2.18	A photograph showing the levitation of dust particles in DPEx device.	60
2.19	Variation of dust charge calculated using OML and CEC theories with pressure.	62

2.20	Schematic diagram to show the generation of flow by altering the potential hill technique. a) The confinement of dust particles by a grounded wire and b) the flow of particles over the floating wire.	68
2.21	Modulating the height and the width of the hill by attaching resistances in between the wire and the ground.	68
2.22	The magnitude and velocity vector of dust fluid analyzed using PIV technique.	70
2.23	Color plot showing the trajectory of particles when analyzed using spit code.	71
3.1	A schematic of the experimental set up for performing flowing dusty plasma experiments.	77
3.2	Color plot showing the trajectories of two particles where the flow is generated using (a) Single Gas Injection Technique (SGI) (b) Dual Gas Injection Technique (DGI).	79
3.3	Time evolution of 10.66 μm particle at a fixed pressure of $p=12$ Pa and discharge voltage of 300 V when the flow is generated by Single Gas Injection Technique (SGI).	81
3.4	Variation of asymptotic velocity of 10.66 μm particle with flow rate difference for three different gas pressures.	82
3.5	Variation of constant velocity with pressure for three different micro particles of diameter 10.66 μm , 8.90 μm and 4.38 μm when the flow is generated by SGI technique	84
3.6	(a) Time evolution and (b) variation of constant velocity with pressure of 8.90 and 4.38 μm micro particle when flow is generated by Dual Gas Injection (DGI) technique.	85

3.7	Variation of constant velocity with pressure for Krypton, Argon, Neon gases.	87
3.8	Theoretical plot of time evolution of 10.66, 8.90 and 4.38 μm particles.	92
4.1	A schematic diagram of dusty plasma experimental (DPEx) setup. .	101
4.2	Variation of (a) the closest approach and (b) the height achieved by a 4.45 μm particle above the charged wire versus the velocity of the micro particle.	104
4.3	Color plot showing the trajectory of the particle, having radius $r_d = 4.45 \mu\text{m}$, while crossing the charged wire at a pressure of $p=12 \text{ Pa}$ and a discharge voltage $V_d = 320 \text{ V}$. The filled circle represents the location of the wire whereas the arrow represents the direction of flow.	105
4.4	A plot showing the trajectories of a particle of radius $a = 4.45 \mu\text{m}$ for different (a) discharge voltages and (b) background neutral pressures.	106
4.5	Variation of width (star) and height (open circle) of the potential hill created by the charged wire with (a) discharge voltages and (b) background neutral gas pressure.	107
4.6	Time evolution of (a) kinetic energy, (b) gravitational potential energy and (c) energy loss due to neutral drag force (d) electric potential of a particle of radius $r_d = 4.45 \mu\text{m}$ while riding over a charged object for a given pressure $p = 12 \text{ Pa}$ and voltage $V_d = 320 \text{ V}$	108
4.7	Variation of maximum potential calculated from potential profiles for different discharge (a) voltages and (b) gas pressure.	109
4.8	A plot showing the variation of (a) the height of the potential with flow rate difference and (b) the maximum potential.	112

4.9	(a) Radial potential profiles at $z=0$, $z= 6$ mm and $z=16$ mm. $z=0$ corresponds to the location of the wire. and (b) Axial potential profiles at $y=6.6$, $y=5.58$ mm, $y=4.57$ mm, $y=3.56$ mm	113
5.1	A schematic diagram of dusty plasma experimental (DPEX) setup.	119
5.2	(a) Equilibrium configuration of dust cloud before generating the flow. (b) Dust flow initiated by lowering the potential hill suddenly by making it floating. The yellow circle represents the location of charged object and flow is generated from right to left.	121
5.3	Propagation of wakes in the direction of flow (in downstream direction) for the case of subsonic flow. The position of wire is represented by the yellow dashed line.	122
5.4	(a) Propagation of solitons against the direction of flow (in upstream direction) and wakes in the direction of flow (in downstream direction) for the case of supersonic flow. The position of wire is represented by the yellow dashed line. (b) The intensity profile of the solitons and wakes.	123
5.5	(a) Source function (b) Precursor solitons and wakes obtained from the numerical solution of f-KdV equation.	125
5.6	(a) Variation of height (represented by red open circles) and width (represented by blue star) of the potential hill with V_{wg} . (b) Power law fit on the height and width of the electrostatic potential created by the charged wire.	126
5.7	Excitation of precursor solitons for (a) 5 V, (b) 75 V, (c) 132 V by varying the voltage across the hill created by the charged wire. . . .	127

5.8	Variation of (a) amplitude (represented by red open circles), width (represented by blue star) and (b) velocity of the excited precursor solitons for the case of supersonic fluid flow with the voltage drop V_{wg} across the resistance.	128
5.9	Variation of amplitude of solitons with (a) amplitude of source, (b) width of source numerically obtained from the solution of f-KdV.	130
5.10	Equilibrium configuration of dust cloud before generating the flow for two different shapes of the charged object.	131
5.11	(a) Generation of non linear wakes in the direction of flow when the flow is initiated and facing rising slope of the potential hill (b) Intensity profile of Fig. 5.11(a).	132
5.12	Time evolution of numerical solution of f-KdV equation using the source function half Gaussian function as Source function to replicate the triangular shaped object.	133
5.13	(a) Generation of wakes and solitons when the flow faces sharp rise of the potential hill (b) intensity profiles of these wakes and solitons extracted from Fig. 5.13(a).	134
5.14	(a) Source function (b) Time evolution of numerical solution of f-KdV equation by reversing the source function as shown in Fig. 5.12(a).	135
6.1	A schematic diagram of dusty plasma experimental (DPEx) setup.	142
6.2	(a) Equilibrium configuration of dust cloud before generating the flow. (b) Flow in the dust fluid is initiated from right to left by lowering the potential hill suddenly. The yellow circle represents the location of charged object.	144

6.3	(a) A typical experimental image of excitation of single pinned soliton. The dashed vertical line marks the position of the wire. (b) Axial profile of compression factor of density perturbation extracted from 6.3(a).	147
6.4	Typical images of excitation of (a) double (b) four and (c) many pinned solitons along with the wakes. The yellow dashed line represents the location of the charged object.	148
6.5	Density compression factor of (a) two, (b) four and (c) many sharp peaks extracted from Fig. 6.4(a), (b) and (c). The dashed line represents the location of the wire.	149
6.6	(a) Intensity profile of pinned solitons and wakes over time. The dashed lines show that the higher amplitude solitons remain stationary in the laboratory frame, whereas the wakes move along the flow. (b) The zoomed version of Fig. 6.6(a), which clearly shows that the wakes move from right to left.	150
6.7	Variation of maximum density compression n_{dmax}/n_{d0} with the normalized flow velocity M	151
6.8	Time evolution of pinned solitons (solid lines) as well as a source function (dashed lines) obtained numerically by solving the f-KdV equation.	152
6.9	A plot for one, three, many pinned solitons (represented by solid line) from the numerical solutions of forced KdV equation for three different amplitude, width and velocity of source functions for $t=24$. Dashed lines represent the source functions.	154
7.1	A schematic diagram of dusty plasma experimental (DPEx) device.	160

7.2	(a) An experimental image of equilibrium dust cloud with linear decreasing dust density. (b) Intensity profile extracted from Fig. 7.2 (a).	163
7.3	Equilibrium dust density extracted from the intensity profile as shown in Fig. 7.2 and few measurements of dust density (closed circles) at z 18–32 mm.	165
7.4	(a) Experimental image of density crests in an inhomogeneous dust cloud. (b) Intensity profile of high amplitude density crests extracted from Fig. 7.4(a). The arrow represents the direction of propagation of the shock fronts.	168
7.5	Sequence of images: (a) Stable unperturbed inhomogeneous dust cloud, (b–e) spontaneously excited dust acoustic waves in the compressed dust cloud, (f–i) excitation and propagation of nonlinear shock waves. (j) image of dust cloud when the gas flow rate is restored.	169
7.6	(a) Amplitude and (b) Space time graph of two colliding non-linear waves.	171
7.7	(a) Time evolution of shock wave front in space. (b) Variation of amplitude and width of that particular shock front in space as shown in Fig. 7.7(a).	172
7.8	Variation of (a) amplitude and (b) width of shock fronts along z -position.	174
7.9	Spatial variation of compression factors obtained experimentally and theoretically.	175

7.10 Typical shock wave train obtained from the numerical solution of m-KdV-Burger equation. Inset shows the same that is obtained experimentally.	180
7.11 (a) Amplitude and (b) Width profile estimated from the numerical solution of m-KdV Burger equation.	181

List of Tables

2.1 Discharge and plasma parameters	57
2.2 Dusty plasma parameters	65

8

Summary and Future Scope

8.1 Summary

The thesis addresses the experimental studies on the excitation of non-linear waves in a flowing dusty plasma past a charged obstacle. In particular the modifications in the propagation characteristics of precursor solitons due to the different shapes and sizes of the charged object over which the dust fluid flows. This study is extended further to excite the pinned solitons in a flowing dusty plasma when the fluid is made to flow over the charged object with highly supersonic velocity. Further, we have also investigated the propagation characteristics of shock waves in an inhomogeneous dusty plasma. Various experimental investigations analogous to hydrodynamic experiments and are associated with transcritical flows have been carried out in the dusty plasmas. Few notable examples are - the excitations of wakes or Mach cones [41] behind a moving charged object, bow shocks formation

in a flowing dusty plasma around an obstacle. All these studies in the past were only focussed on the downstream region or the region behind the moving charged object. Surprisingly, the fore-wake phenomena in the upstream region ahead of a fast-moving object, a spectacular phenomenon in hydrodynamics, have not been paid much attention by the plasma as well as the dusty plasma physics community. Recently, Jaiswal *et al.* [48] reported the first experimental observation of precursor solitons in a flowing dusty plasma. The nonlinear coherent solitary structures are excited by a supersonic flow of the dust particles over an electrostatic potential hill. In a frame where the fluid is stationary and the hill is moving the solitons propagate in the upstream direction as precursors while wake structures consisting of linear DAWs are seen to propagate in the downstream region. A theoretical explanation of these excitations based on the forced Korteweg de Vries (f-KdV) model equation is provided. However, in the past experiments of Jaiswal *et al.* [48], the nature of the potential profile around the charged object over which the dust fluid flows was not precisely known. As a result, they were unable to study further the propagation characteristics of the precursor solitons by varying the shape and size of the charged object. Besides, the earlier experiments were carried out for a flow that was slightly supersonic ($M = 1-1.2$). This essentially prevented the authors from getting a complete picture of the fore-wake excitation in the case when the fluid flows over the charged object with highly supersonic velocity. All the earlier studies of excitations of non-linear structures have been carried out in a homogeneous dusty plasma medium. However, in an experimental situation, density inhomogeneity is likely to be present when one performs experiments with large size dusty plasma. The present thesis is motivated by seeking answers to some of these unexplored issues by further in-depth experiments on fore-wake excitations

in a flowing dusty plasma. The experimental and supportive theoretical results provide a consolidated and extended picture of this phenomenon covering a wide range of excitation conditions.

All the experiments in this thesis work are carried out in a versatile tabletop Dusty Plasma Experimental (DPEX) device. It is basically a Π -shaped Pyrex glass tube which consists of three cylindrical glass tubes. The glass tube mounted horizontally on the optical table acts as the main chamber whereas the other two cylindrical glass tubes serve as auxiliary chambers. The device geometry of DPEX device is similar to PK-4 device but the dimensions of chamber, electrodes geometry and their arrangement, as well as the plasma generation, are completely different from PK-4. The main chamber is used for performing the experiments and for optical diagnostics whereas the two auxiliary chambers are used for venting the system, electrode connection, gas inlets, etc.. A rotary pump is used to evacuate the vessel and a mass flow controller is used for feeding the gas into the chamber in a controlled way. A circular disc acts as an anode whereas a long tray electrode is placed in the main chamber serves as a grounded cathode. The two sides of the cathode are bent to provide the radial confinement to charged dust particles whereas two SS strips placed at the two ends of the cathode confine the particles in the axial direction. Melamine Formaldehyde (MF) particles, as well as Kaolin particles, are used to create a dusty plasma. Mono-dispersive Melamine Formaldehyde (MF) dust particles are inserted by a dust dispenser whereas poly-dispersive Kaolin particles are sprayed on the cathode before closing the chamber. The bent ends of the cathode also provide the facility to install a wire in a radial direction which acts as a charged object for most of the experiments. In some of the experiments, a triangular-shaped object is also used. For the experimental

convenience, rather than moving a charged object in the plasma, we have chosen a configuration in which the dusty plasma flows over an electrostatic potential hill representing a stationary charged object.

To begin with, the experimental chamber is pumped down to its base pressure by the rotary pump and then argon gas is introduced into the chamber to set the working pressure in the range of 9–16 Pa. A Direct Current (DC) glow discharge Argon plasma is then produced in between the asymmetrically shaped electrodes by applying a DC voltage in the range of 280–400 V in between the anode and cathode. The plasma is characterized thoroughly by measuring the plasma parameters such as plasma density, electron temperature, floating and plasma potential by using a single Langmuir probe and an emissive probe in absence of dust particles. Typical experimental values are plasma density $n_i \sim 1 - 3 \times 10^{15} \text{ m}^{-3}$, electron temperature $T_e \sim 2 - 5 \text{ eV}$, plasma potential 260–350 V and floating potential 230–300 V over the range of discharge conditions. The radial profiles for a range of discharge conditions are used to estimate the sheath electric fields. The earlier measurements of plasma density, electron temperature, and plasma potential in axial direction suggest that the plasma remains almost uniform along the axis of the main chamber.

After characterizing the plasma, a dusty plasma is created by introducing the micron-sized Kaolin/Melamine Formaldehyde particles into the plasma. In the plasma environment, these particles acquire a negative charge by collecting more electrons than ions and levitate in the sheath region where the gravitational force gets balanced by the sheath electric field force. These charged particles are then confined in an electrostatic potential well provided by the bent edges of cathode and two axial confining strips. The equilibrium dust cloud is formed by adjust-

ing precisely the pumping speed and the gas feeding rate. The particles in the cloud are seen by shining a laser and their dynamics are captured using a CCD camera and the images are stored in a computer for further analysis. The equilibrium dusty plasma parameters like inter grain distance, dust density, dust charge, dust temperature, and Coulomb coupling parameters are measured/estimated by tracking individual particles for a less dense dusty plasma. The range of dusty plasma parameters such as density, temperature, dust charge, coupling parameters are $n_d \sim 1 - 10 \times 10^9 \text{ m}^{-3}$, $T_d \sim 0.03 - 0.1 \text{ eV}$, $Q_d \sim 5 - 20 \times 10^3 e$, $\Gamma \sim 10 - 100$, respectively. Since the experiments are aimed to study the fore-wake excitations in a flowing dusty plasma over a charged object, three different techniques of flow generation e.g. (i) Single Gas Injection (SGI) technique, (ii) Dual Gas Injection (DGI) technique and (iii) Altering the potential technique are employed to create a flow in a dusty plasma. The flow velocities in the dust fluid are measured using either a Particle Image Velocimetry (PIV) technique [119] or by using an IDL based super Particle Identification Technique (sPIT) [118] depending upon the experimental requirements. The details of flow generation and measurement techniques are discussed in detail in Ref. [137].

As discussed, SGI and DGI techniques are extensively used to initiate the flow in the dust fluid for studying the excitation of linear and nonlinear structures/waves in the DPEx device. It is already reported that in both the techniques the flow of neutral plays a crucial role to determine the dynamics of dust particles. However, a quantitative assessment of the influence of the neutral streaming force on particle transport is still missing. In order to elucidate the details of the dust flow dynamics, a systemic study is carried out over a range of gas flow conditions, background neutral pressures, different species of background neutrals, and differ-

ent dust particle sizes. Extensive visual images of the dust particle trajectories have been collected and analyzed to trace their trajectories. In the SGI technique, the particles start from rest and accelerate to finally reach an asymptotic steady-state velocity, whereas, in the DGI technique, the dust particles start their journey from the asymptotic velocity. It is found that this steady-state velocity is strongly dependent on the gas flow and background neutral pressure-it increases with an increase in the flow velocity and decreases with an increase in the neutral pressure. It is also observed that although lighter dust particles accelerate faster, the final steady-state velocity value is independent of the size of the particles when all other conditions are kept the same. The size of the neutral particles, however, directly impacts the velocity-it decreases with an increase in the mass of the neutral species. Theoretical estimates of the various forces acting on the dust particles reveal that the neutral streaming force is the dominant one in inducing the flow. A simple model equation based on such a force is used to provide a qualitative description of the dust motion and a physical understanding of the dynamics.

This thesis work mostly deals with the excitation of fore-wake phenomena in a flowing dusty plasma when the flow in the dust fluid is initiated over a charged object having different shapes and sizes. Hence, before performing any physics experiment, it is essential to have a clear understanding of the potential structure around the charged object and its dependency on the discharge parameters. In this thesis, we have demonstrated a novel technique to measure the potential profile around a charged object by using a dust particle as a dynamic microprobe. Initially, a few micron-sized dust particles are introduced into the plasma, which was found to float in between the grounded wire (charged object) and the right confining strip. A steady-state equilibrium of the dust particles is achieved by fine-tuning of

the pumping speed and gas flow rate. A flow of these dust particles is then initiated using the SGI technique. Due to the sudden change in the gas flow, the particles travel over the grounded wire which is placed on the path of the particles. From the knowledge of the instantaneous position of the particles and their velocities, their potential and kinetic energies are estimated over a wide range of discharge parameters. The axial and radial electrostatic potential around the charged object is then estimated by employing the conservation of total energy. It is found that the potential around the charged object is symmetric in axial direction and parabolic in the radial direction. The size of potential around a charged object shrinks with the increase in background pressure and discharge voltage. In this technique, the particles act as dynamic micro-probes and measure the potential very precisely without significantly perturbing the potential around the charged object.

From the knowledge of our earlier experiments, a detailed study is then carried out on the modifications in the propagation characteristics of precursor solitons by using different shapes and sizes of the charged object over which the dust fluid flows. A floating copper wire installed radially on the cathode, acts as a charged object in the plasma environment. The flow on the dust fluid is initiated by suddenly lowering the potential of the charged object from grounded potential to close to floating potential. The size (height and width) of the potential hill is then varied by drawing current from the wire through a variable resistance. With a decrease in the height of the potential hill, the amplitude, velocity, and number of excited precursor solitons are found to decrease, whereas the widths of the solitons are seen to increase. It is found that below a threshold value, these solitary waves are not excited, and the dust fluid simply flows over the hill. To examine the effect due to the shape of the potential profiles, the wire is replaced by a triangular

object. Only trailing wakes are seen to be excited when the dust fluid faces the linearly increasing slope of the potential profile, whereas both solitons and wakes get excited when the object is placed with the sharp edge facing the flow. All the experimental findings qualitatively agree with numerical solutions obtained with different source terms in the forced-Korteweg de Vries (f-KdV) model equation.

In another set of experiments, a new class of driven nonlinear structures called pinned solitons are excited experimentally by making the dust fluid flow in a highly supersonic ($M \sim 1.5 - 3$) manner over the same charged object. A highly supersonic flow is generated by performing the experiments in a very low discharge voltage and background pressure and the flow is generated by using the altering confining potential. The highly supersonic flow of dust fluid generates multiple nonlinear stationary structures in the laboratory frame, whereas in the frame of fluid, these structures are seen to attach with the moving object and are hence called “pinned solitons”. To understand the propagation characteristics of these structures, the flow velocity of the dust fluid is tuned by changing the size of the charged object. It is found that the number of excited structures and their amplitude increases with the increase of the flow velocity of the dust fluid. The variation of structures amplitude shows a parabolic increase with the increase of fluid flow velocity similar to the simulation study of Tiwari *et al.* [50]. The experimental findings are then qualitatively compared with the numerical solutions of forced Korteweg de Vries (f-KdV) equations.

Lastly, an experimental investigation of propagation characteristics of shock waves in an inhomogeneous dusty plasma is carried out. A homogeneous dusty plasma, made up of poly-dispersive Kaolin particles, is formed in the DC glow discharge Argon plasma by maintaining a dynamic equilibrium of pumping speed

and gas feeding rate. Later, an equilibrium density inhomogeneity in the dust density is created by an imbalance of their dynamic equilibrium. The wave structures are then excited in this inhomogeneous dusty plasma by a sudden compression in the dust fluid. These structures are characterized thoroughly and the frequent merging of two such wave fronts with different amplitudes and velocities essentially confirms that these structures are shock waves in nature. To investigate the modification in the propagation characteristics, the amplitude and the width are measured spatially. The amplitudes of the shock waves increase whereas width broadens up as the shock structure propagates downhill along the density gradient. A modified-KdV-Burger equation is derived by including bulk viscosity and density inhomogeneity in the momentum equation and used to provide a theoretical explanation of the results including the power-law scaling of the changes in the amplitude and width as a function of the background density.

8.2 Future Scope

The experiments discussed in this thesis can form the basis for further in-depth studies of flow-induced excitations of non-linear waves and structures especially the fore-wake phenomena in dusty plasmas and can motivate new experimental, theoretical and simulation studies. We discuss a few possible future directions of research in this area:

- Our experiments on the excitation of precursor solitons is carried out by flowing the dust fluid over a stationary potential hill. These fore-wake phenomena can also be performed by moving the charged object supersonically through a stationary dust fluid to replicate the experiments that were carried

out in hydrodynamics. This set of experiments will minimize the changes of plasma parameters during the generation of flow.

- The interaction of the wake-field with the precursor solitons is another interesting extension of our work that can be usefully carried out. In these controlled experiments, the flow of dust fluid will be generated over two stationary charged objects in such a way that the wakes excited by the first object in the downstream region will interact with the precursors excited by the second object in the upstream region.
- All the experiments presented in this theses are carried out in a weakly coupled dusty plasma. It would be useful to give an attempt to investigate the modification in the propagation characteristics of the nonlinear waves and structures in a strongly coupled flowing dusty plasma having considerably high values of the Coulomb coupling parameter (Γ).
- Interactions of these for-wake excitations with an additional stationary potential barrier in the upstream regime can be studied further. The changes in the propagation characteristics of these nonlinear waves can be investigated by precisely tuning the strength of the potential hill.
- Our experimental results of the excitation of precursor/pined soliton are qualitatively compared with f-KdV soliton solutions. The nonlinear structures excited in the experiments are purely 2-dimensional whereas the solution of the f-KdV equation gives a 1-dimensional solution. For a better comparison, one needs to formulate and solve the *forced*-KP (Kadomtsev Petviashvili) equation instead of a *forced*-KdV equation.
- In our flowing dusty plasma experiments, the dynamics of dust particles are

studied by tracking the individual particles. The electric field is measured using a couple of emissive probes at two axial locations to get an idea of ion drag force that acts on the particles. However, to get a clear picture of plasma flow, a Mach probe measurement is indeed needed.

SUMMARY

Transcritical plasma flows is a common situation in astrophysical as well as laboratory plasmas. Interaction of flowing plasmas with stationary objects leads to excitations of many interesting structures such as bow shocks, solitons, wakes, etc. An attempt is made to study these spectacular phenomena in the laboratory by using flowing complex plasmas. The presence of micron or sub-micron charged particles in the electron-ion plasmas increases the complexity of the system and has led to the development of the new field of dusty or complex plasmas. The experiments are carried out in the Dusty Plasma Experimental (DPEX) device in which a DC glow discharge Argon plasma is produced in between a circular anode and a grounded tray cathode. A dusty plasma is then generated either using mono-dispersive MF particles or poly-dispersive Kaolin particles. The flow in the dust fluid ranging from subsonic to supersonic over an electrostatic potential is achieved by using different techniques. The characteristics of the dust dynamics are investigated as a function of the differential gas flow rate, the background neutral pressure, the dust particle size, and the neutral species of the gas. The asymptotic steady state flow velocity of the injected micron sized dust particles is found to increase with an increase in neutral flow velocity and decrease with an increase in the background pressure. Excitations of nonlinear structures and their propagation characteristics for various range of flows are studied. Subsonic flow generates normal wake patterns whereas a slightly supersonic flow leads to excitations of various structures in the fore-wake region called precursor solitons. The shape and size of the charged object over which the dust fluid flows play an important role to determine the characteristics of the precursor solitons and there exists a threshold value of object height below which the dust fluid simply flows

over the object without exciting any nonlinear structures. The shape and size of the charged object is measured by using dust as a microprobe. In this technique, the particles act as dynamic micro-probes and measure the potential very precisely without significantly perturbing the potential around the charged object. Generation of highly supersonic flow changes the complete dynamics of fore wake structures which leads to the excitation of stationary structures called pinned solitons. It is found that the number of excited structures and their amplitude increases with the increase of the flow velocity of the dust fluid. The variation of structures amplitude shows a parabolic increase with the increase of fluid flow velocity. The experimental findings of precursor and pinned solitons are qualitatively compared with the numerical model of the forced-KdV equation. The study of the nonlinear structures in an inhomogeneous dusty plasma is also carried out by investigating the propagation characteristics of shock waves when they travel downhill along a density gradient. The modified-KdV-Burger equation is derived for such a case and numerically solved for a dusty plasma medium with a dust density gradient and where the dissipation effect comes from the strong coupling induced viscosity as well as neutral induced damping. The amplitudes of the shock waves increase whereas width broadens up as the shock structure propagates downhill along the density gradient. The theoretical and numerical explanation of the results including the power-law scaling of the changes in the amplitude and width as a function of the background density.

1

Introduction

1.1 Introduction and Motivation

A plasma is partially or fully ionized gas consisting of electrons, ions and neutral particles which move randomly in such a way that they always maintain a quasi-neutrality condition. Plasma has often been referred to as the fourth state of matter and 99% of our universe is made up of plasma. Plasmas occur naturally as well as can be made artificially. Naturally occurring plasmas can be Earth-based i.e., terrestrial plasma or space-based i.e., astrophysical plasma. The examples of terrestrial plasmas are lighting, Auroras, ionosphere, extremely hot flames, etc., whereas some of the astrophysical plasmas are stars, galaxies, solar wind, interstellar nebulae, space between stars and planets, etc.. In contrast, artificial or man-made plasmas include fluorescent light-bulbs, neon signs, and plasma displays like television or computer screens. Artificial plasmas are often made in

laboratories to understand some of the naturally occurring plasmas.

The existence of highly charged and massive dust particles is ubiquitous in astrophysical plasmas. These particles either get charged by collecting electrons and ions from the ambient background plasma or get directly ionized in the astrophysical environment and behave in a very different manner compared to a ‘pure’ electron-ion plasma. The mixture of these charged dust particles with the conventional plasma is known as dusty plasma [1, 2]. Due to the additional complexity of studying plasmas with charged dust particles, dusty plasmas sometimes are also called complex plasmas. Dusty plasmas also share several physical concepts and similarities with colloidal suspensions, where plastic charged particles are immersed in an aqueous solution. In analogy to these systems, dusty plasmas are also referred to as “colloidal plasmas”. One of the distinct advantages of investigating a dusty plasma system is the ability to track the individual dust particle motions using simple videography techniques, thereby obtaining insights into the micro dynamics governing the collective behavior of the system as well as its statistical properties. Hence, a dusty plasma provides an excellent experimental platform for investigating a host of fundamental physics problems associated with phase transitions and allied topics that have relevance for areas as diverse as statistical mechanics, fluid mechanics, soft condensed matter, strongly and weakly coupled systems, active matter dynamics, colloidal physics and warm dense matter. The ease of observation of the individual dust dynamics coupled with the convenient time scales of the collective dynamics of such systems has spurred plenty of laboratory investigations of such medium.

Similar to plasma, dusty plasmas are also omnipresent in interplanetary or interstellar environments, where the dust particles are invariably immersed in a



Figure 1.1: Picture representing the explosion of solar nebulae. Credit: Hernan Canellas.

radiative as well as in a plasma environment. For example, it is found that our solar system has evolved from the solar nebulae (shown in Fig. 1.1) in which a cloud of hydrogen gas and dust collapsed due to gravitational force [3–5]. The formation of planets, meteoroids, planetesimals have evolved from the solar nebulae by the coagulation of dust. The dust particles are also observed in planetary rings [6] of Saturn from the images taken by Voyager-2. The images in Fig. 1.2 show a pattern of radial spokes rotating around the outer edge of Saturn’s dense B-ring and consist of charged dust grains. These dust particles are also observed in interstellar clouds, zodiacal light, Earth’s magnetosphere, etc..

Dusty plasma causes a great problem in semiconductor industries. In the late 1980s, while making the silicon wafers, semiconductor scientists discovered that micron or sub-micron sized dust particles get suspended over the wafers and form rings of dust particles. These particles are created by the reactive gases in the plasma environment and contaminate the silicon wafers when the plasma is switched off [7]. However, now a days the dusty plasma is demonstrated as a potential candidate to many applications like electrostatic painting [8], plasma

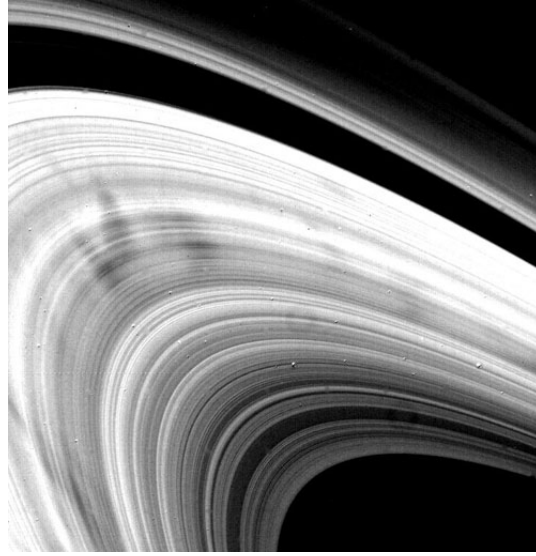


Figure 1.2: Spokes observed in Saturn's ring as seen by Voyagers 2. Credit: Cassini Imaging Team.

spraying [8], nanomedicine [9, 10], microbiology [11] etc..

Dusty plasmas are also occasionally seen in different fusion devices (e.g. tokamak) [12, 13]. The dust particles, made of materials like beryllium, carbon, tungsten, etc., get sputtered from the first wall of the tokamaks. After getting sputtered from the wall, these dust grains accelerate towards the plasma due to the electric field or flow of ions and play an important role in deciding the transport properties of fusion plasmas. These liberated dust particles sometimes also form thin films on the walls of tokamaks and pose safety issues over the radioactive elements. Due to its numerous observations as well as technological and scientific implications, dusty plasmas is a current topic of research in the field of plasma processing and fusion research.

The first experimental observations of Coulomb crystal [14] and sound waves [15] in laboratories opened up a whole new area of fundamental research in dusty plasma physics. In such a plasma, the dust component gets strongly coupled

due to the large charge residing on each dust surface and the low temperature of the dust species. Due to the strong coupling effect, the dusty plasma forms an ordered structure in the form of Simple Cubic (SC), Body Centred Cubic (BCC) and Face Centred Cubic (FCC) lattice [15, 16]. The quantities namely, the dust temperature, the dust charge as well as the interparticle distance between the dust particles, are amenable to external control and can be manipulated to steer the dust component from a gaseous state to a liquid state to a crystalline state. The individual particles in dusty plasma yield a small value of the charge-to-mass ratio due to their heavy mass and high charge. These unique features make the time scales of their collective phenomena very slow (ms to s) and characteristic lengths large (mm to cm). As a result, the dynamics of these dusty particles can be seen by naked eyes and captured very easily with the help of laser and camera. Dusty plasma medium has therefore proved to be a useful and simple paradigm for the study of numerous physics problems such as phase transitions [1, 17] recrystallization [18] heat transport [19–21] formation of Mach cones [22, 23], excitation of linear and nonlinear waves/structures and instabilities [2], fluctuation theorem for entropy production [24], etc..

Dusty plasma provides an excellent medium that supports the excitation of a variety of linear and non-linear waves and structures. During the past couple of decades, extensive studies have been carried out both theoretically and experimentally on the excitation of linear modes like Dust Acoustic Waves (DA) [25–27], Dust Ion Acoustic (DIA) waves [28], Dust Lattice Waves [29], non-linear modes like Dust Solitary (DS) waves [30, 31], Dust Acoustic Shock (DAS) Waves [32, 33] and various coherent structures like voids [34–37], vortices [38, 39], etc.. The fluid concept of dusty plasma is employed widely to understand the excitation of these

collective phenomena. As in a hydrodynamic fluid, there have also been observations of wake structures in laboratory dusty plasmas. These wakes are sometimes termed as Mach cones [22, 23, 40–43] and are generated when a dust particle moves through a stationary dusty plasma medium or a laser is shined through it.

The excitation of precursor solitons ahead of a fast-moving object with wakes behind it is a phenomenon that has been widely studied in hydrodynamics particularly in the context of disturbances created by ships and boats close to the coast [44–46]. These earlier studies have also provided model descriptions of this fascinating nonlinear phenomenon by employing a forced Korteweg-de Vries equation or a forced generalized Boussinesq equation [44]. Controlled laboratory experiments using model ships moving in a channel were carried out by Wu [45] and Sun [46]. It was found that as long as the speed of the object moving through the fluid (water) was below a critical value (in this case, the phase velocity of the surface water waves), the movement only created the customary trailing waves (wakes) in the downstream direction. A dramatic change occurred when the object speed was transcritical. Then, in addition to the trailing wakes, the object also created a steady stream of solitons ahead of it in the upstream direction. These solitons with a speed higher than the object moved away as precursors. The phenomenon was Galilean invariant [47]—it could be reproduced by keeping the object stationary and moving the fluid over it.

The topic of these fore-wake excitations (precursor solitons) has, however, received very limited attention in plasma physics community until now. The first experimental demonstration of the generation of a precursor soliton in a flowing dusty plasma was reported in 2016 by Jaiswal *et al.* [48]. In their study, they observed the spontaneous excitation of precursor solitons when a supersonically

(with respect to the dust acoustic speed) moving dusty plasma fluid was made to flow over an electrostatic potential structure. In the past experiments of Jaiswal *et al.* [48], it was found that for the case of subsonic flow over a stationary charged object, the wakes are excited on the left side of the object and travel in the direction opposite to the flow. In the frame of the fluid where the object moves from left to right, these wakes propagate in the downstream direction. Similar to hydrodynamic experiments, when the flow was made supersonic, a dramatic change in the excitations was observed. In addition to the wakes, the large-amplitude solitary waves are observed to the right of the object that travels in the direction opposite to the flow or the frame of the fluid in the upstream direction. The physical mechanism underlying this phenomenon can be understood in terms of the fluid concept used to explain hydrodynamic precursors. An object moving in a fluid always creates a pileup of matter in front of it. If its speed is subcritical, then the matter in front can disperse away at the linear phase velocity, leading to the creation of a wake structure. However, if the object speed is supercritical, then the matter in front cannot disperse away fast enough and continues to build up. At a certain stage, nonlinear effects become important, and this can lead to the formation of solitons or other nonlinear structures. These nonlinear structures can move at a higher speed and can, therefore, separate from the object and move away as precursors. These first-ever observations of precursor solitons in plasma have been well characterized by detailed experimental measurements of their propagation features and qualitative comparisons with results from theoretical models based on the forced-KdV equation derived for a charged object moving through a dusty plasma medium [49]. The existence of such precursor excitations has also been confirmed from full-scale fluid simulations [50] and molecular dynamic simu-

lations [51].

However in the past experiments of Jaiswal *et al.* [48], the potential profile around the charged object over which the dust fluid flows was unknown. Due to this reason, it was not possible to study further the modification in the propagation characteristics of these precursor solitons when the fluid flows over a charged object with different shapes and sizes. Also, the earlier experiments were carried out for a slightly supersonic flow ($M = 1 - 1.2$). This essentially restricts the authors to get a complete picture of the fore-wake excitation in a case when the fluid flows over the charged object with highly supersonic velocity. To date, all the earlier studies of excitations of non-linear waves in dusty plasma have been carried out in a homogeneous medium. However, in an experimental situation, the presence of density inhomogeneity is obvious when one performs experiments with large size dusty plasma. The shortcomings of earlier experiments motivate us to perform in-depth experiments on the fore-wake excitation in a flowing dusty plasma. The objective of this thesis work is to further consolidate and extend the previous experimental study by carrying out a detailed investigation of the propagation characteristics of the precursor solitons under varying excitation conditions. In particular, attention is paid to look at the effects of varying the size and shape of the potential hill over a range of fluid flow velocity on the fore-wake phenomenon. The objective also includes studying the modification on the propagation characteristics of oscillatory shock waves when they encounter a density inhomogeneity. These insights should prove helpful in interpreting the manifestation of this concept in natural occurrences such as in excitations triggered by solar wind interactions with the earth and moon or space debris or satellite interactions with the ionospheric plasma. The findings may also stimulate further experimental and theoretical

studies toward more fundamental investigations of this yet poorly explored topic in plasma physics.

The rest of this chapter is organized as follows: basics of complex plasmas and the characteristic parameters used to describe dusty plasmas are discussed in Sec. 1.2. In Sec. 1.3) some of the past studies on flowing complex plasmas are described. Then the scope and outline of this thesis are described in Sec. 1.4.

1.2 Characteristics of dusty or complex plasma

The normal conventional plasma having electrons and ions are defined by the characteristic parameters like screening lengths, response time scales to any perturbations. Similarly, dusty plasmas are also characterized by the characteristic parameters such as screening lengths, frequencies, quasineutrality, dust charge, surface potential, and coupling parameter, etc.. The knowledge of these parameters is necessary to establish the background for the experimental analysis and to understand the underlying physics associated with them. The details of these characteristic parameters are described in the next subsections.

1.2.1 Typical length scales

Dusty plasmas can be characterized by three different length scales namely Debye length (λ_D), the radius of a dust particle (r_d) and inter-particle distance (d) that decide the role of dust particles in the plasma. In the case of $r_d \ll \lambda_D < d$, the individual charged dust particles are shielded and isolated from each other and behave like “dust in plasmas”. Whereas for $r_d \ll d < \lambda_D$, the dust particles show collective behavior are called as “dusty plasma”.

1.2.1.1 Debye length

The most fundamental characteristic of plasma is its ability to shield any electric field either applied externally or the field associated with an individual charged particle. The associated distance over which the influence of the electric field of an individual particle can be experienced by another particle is known as Debye length (λ_D) or sometimes called screening length. The Debye length in dusty plasma is expressed as [52].

$$\lambda_D = \frac{\lambda_{De}\lambda_{Di}}{\sqrt{\lambda_{De}^2 + \lambda_{Di}^2}} \quad (1.1)$$

where $\lambda_{D(e,i)} = (\epsilon_0 k_B T_{e,i} / n_{e,i} e^2)^{1/2}$ are the electron and ion Debye lengths. In most of the laboratory experiments the dust particles become negatively charged by absorbing more electrons than ions and hence $n_e \ll n_i$ and $T_e \geq T_i$ which leads to $\lambda_{De} \gg \lambda_{Di}$. Using Eq. 1.1, one can express the value of dust Debye length as $\lambda_D \sim \lambda_{Di}$. It essentially signifies that the screening length of dusty plasma can be determined mainly from the density and temperature of ions.

1.2.1.2 Radius of dust particle

The radius of the dust particle, r_d , is also an important characteristic length and prior knowledge describes its various features. The amount of charge depends on the size of the dust grain and its value becomes higher for bigger particles. The strength of different forces that act on the dust particles in the plasma also depends on the size of the particles. The radius of the particles also determines the cross-sections of different collision processes.

1.2.1.3 Inter-particle distance

The average distance between two dust grains in the plasma is defined as the inter-particle distance (d) and its magnitude can be larger or smaller than the dust Debye length. The inter-particle distance determines whether the dust particle can show collective behavior or behave like an isolated particle. It can also be used to estimate the dust density, Coulomb coupling parameter, etc. in a dusty plasma.

1.2.2 Typical time scales

1.2.2.1 Dust plasma frequency

A space charge region builds automatically whenever the individual charge species in the plasma are displaced from their respective equilibrium positions. This space charge gives rise to a collective motion which is known as plasma oscillation. The plasma oscillation tries to restore the charge neutrality condition. Similar to conventional electron-ion plasmas, the dust particles also exhibit the collective oscillation which is known as dust-plasma oscillation and the frequency associated with this oscillation is known as dust-plasma frequency (ω_{pd}) and can be expressed as:

$$\omega_{pd} = \sqrt{\frac{n_{do}Q_d^2}{\epsilon_0 m_d}}. \quad (1.2)$$

Where n_{do} , Q_d , ϵ_0 , m_d are the equilibrium dust density, charge residing on the individual dust particle, the permittivity of free space and mass of the dust particles, respectively. Due to the higher charge and heavier mass of dust particles compared to electrons and ions, the dust-plasma frequency differs significantly from electron-plasma or ion-plasma frequencies.

1.2.2.2 Collisional frequency

The collisions of plasma species among neutrals are very common in weakly ionized plasmas and as a result, the collective oscillations get damped due to frequent collisions with background neutrals. The collision frequency ν_{sn} of plasma species (electrons, ions, dust) with neutrals can be expressed as:

$$\nu_{sn} = n_n \sigma_{sn} V_{Ts}. \quad (1.3)$$

Where n_n , σ_{sn} , V_{Ts} are the number density of neutrals, collision cross-section and thermal velocity, $v_{Ts} = \sqrt{\frac{k_B T_s}{m_s}}$, respectively.

1.2.3 Dust charge

The dust particles acquire a charge (Q_d) whenever they are introduced in the plasma and there exists a variety of fundamental charging processes through which the dust particles get charged. The important elementary charging processes are:

- Collection of plasma species
- Secondary electron emission
- Photo-ionization
- Thermionic emission
- Field emission
- Radioactivity
- Impact ionization.

In laboratory plasmas, the charging procedure of dust grains is mainly dominated by the collection of electrons and ions by the dust. Because the ions are much heavier than the electrons, initially the ion current (I_i) to a dust grain becomes much smaller than the electron current (I_e), and the grain becomes negatively charged. This increases the ion current and decreases the electron current until the currents are equalized, $I_e = I_i$. At that equilibrium condition, the amount of charge (Q_d) residing on the dust surface can be expressed by the following rate equation as:

$$\frac{dQ_d}{dt} = I_e + I_i = 0. \quad (1.4)$$

Q_d can also be defined in terms of dust surface potential (U) as:

$$Q_d = CU. \quad (1.5)$$

Where $C = 4\pi\epsilon_0 r_d$ is the capacitance of spherical dust particle of r_d for $r_d \ll \lambda_d$. The surface potential can be estimated by the Orbital Motion Limited (OML) theory [53] or Collision Enhanced Plasma Collection (CEC) [54, 55] theory, which will be discussed in more detail in the next section.

1.2.4 Dust surface potential

In dusty plasmas, the dust charge is usually estimated by assuming the dust particles to be isolated spherical capacitors. The surface potential of these spherical charged objects with respect to the plasma potential is estimated by assuming the dust particles are similar to floating single Langmuir probes. In this condition, the net current drawn by each isolated dust particle is approximated to be zero. Orbital Motion Limited (OML) and Collision Enhanced Plasma Collection (CEC)

theories are widely used to estimate the dust surface potential. They are discussed in detail in the following subsections.

1.2.4.1 Orbital Motion Limited (OML) theory

The most widely used dust charging theory for negatively charged dust particles is the so-called orbital motion limited (OML) theory [53]. The OML theory follows the collisionless particle orbit via conservation of energy and angular momentum. It essentially signifies that the electrons and ions do not encounter any collisions in the Debye sphere to reach the dust surface. In this approach the condition $r_d \ll \lambda_d \ll \lambda_{mf}$ holds good. Where $\lambda_{mf(i,e)}$ is the mean free path of neutrals with ions or electrons and their motions are “orbit-limited”.

Assuming the electrons and the ions obey Maxwellian distributions with temperatures T_e and T_i , respectively, the expressions of electron and ion currents can be given by:

$$I_e = \sqrt{8\pi}r_d^2n_eV_{Te}exp(-z_r)e, \quad (1.6)$$

where $z_r = \frac{eU}{k_B T_e}$ and,

$$I_i = \sqrt{8\pi}r_d^2n_iV_{Ti}[1 + z_r\tau]e. \quad (1.7)$$

Where $\tau = \frac{T_e}{T_i}$. At equilibrium, *i.e.* $I_e + I_i = 0$ we get,

$$\frac{n_e}{n_i} \frac{V_{Te}}{V_{Ti}} exp(-z_r) - 1 - z_r\tau = 0 \quad (1.8)$$

Numerically solving the above equation (Eq. 1.8), one can estimate the value of z_r and then U .

1.2.4.2 Collision Enhanced plasma Collection (CEC) theory

The OML theory estimates the surface potential of the dust by neglecting the collisions of ions with neutrals but it has been recently inferred that even when the mean free path of ions is greater than screening length the grain charge substantially reduces due to ion-neutral collision. A new theoretical approach i.e., Collision Enhanced Plasma Collection (CEC) has been developed by Khrapak *et al.* [54, 55] to account for the ion-neutral collision in the expression of ion current in a weakly collision limit ($\lambda_{mfi} \geq \lambda_D$). The modified expression of ion current is given as follows:

$$I_i = \sqrt{8\pi} r_d^2 n_i V_{Ti} \left[1 + z_r \tau + 0.1 (z_r \tau)^2 \frac{\lambda_D}{\lambda_{mfi}} \right] e. \quad (1.9)$$

Whereas the expression of electron current remains the same as Eq. 1.6. The modified balance equation, which assumes the ion-neutral collision takes the form

$$\frac{n_e V_{Te}}{n_i V_{Ti}} \exp(-z_r) - 1 - z_r \tau - 0.1 (z_r \tau)^2 \frac{\lambda_D}{\lambda_{mfi}} = 0 \quad (1.10)$$

The dust surface potential can be estimated by numerically solving Eq. 1.10 which gives directly the dust charge.

1.2.5 Quasi-neutrality condition

Microscopically the plasma is quasi-neutral in the absence of any external perturbation and the charge neutrality condition can be given by:

$$Q_i n_{io} = n_{eo} e, \quad (1.11)$$

where $Q_i = Z_i e$ is the ionic charge and n_{io}, n_{eo} are the equilibrium densities of ions and electrons. In the same sense dusty plasma also maintains the charge neutrality condition and the above condition gets altered as some of the electrons are absorbed by the dust particle. The modified quasi-neutrality condition for dusty plasma can be re-written as

$$Q_i n_{io} = e n_{eo} + Q_d n_{do}, \quad (1.12)$$

where, $Q_d = Z_d e$, is the dust charge and Z_d is the dust charge number.

1.2.6 Coulomb coupling parameter

A very important feature of dusty plasma is that it exists in solid, liquid and gaseous states and the parameter associated to determine the phase of dusty plasma is the Coulomb coupling parameter (Γ). The Coulomb coupling parameter is defined as the ratio of potential energy to dust thermal energy and can be expressed as:

$$\Gamma = \frac{Q_d^2}{4\pi\epsilon_0 d k_B T_d} \exp\left(-\frac{d}{\lambda_D}\right) \quad (1.13)$$

The factor $\exp\left(-\frac{d}{\lambda_D}\right)$ takes into account the screening of the dust charge by the plasma species over the length λ_D .

The increase in Γ leads to an increase in the coupling between the particles. When the value of Γ becomes more than 170 [56], the dusty plasma forms an ordered structure and said to be in the crystalline state. The dusty plasma, with Γ ranging from $1 \ll \Gamma \ll 170$, behaves like a fluid state. For the case of $\Gamma \ll 1$, the dusty plasma lies in a weakly coupled gaseous state. Hence, dusty plasma provides an excellent medium by which one can study the phase transition in a

controlled manner by cooling down the gaseous state of a dusty plasma.

1.2.7 Forces on dust particles

There are a number of forces, such as electromagnetic force, gravitational force, ion drag force, neutral drag force, thermophoretic force, radiation pressure force, polarization force, etc. that can act on the charged dust grains and may govern their dynamics in the plasma [1]. The basic definition of different forces and their governing equation is discussed in the following subsections.

1.2.7.1 Electromagnetic force (\vec{F}_{EB})

The electromagnetic force (\vec{F}_{EB}) plays an important role to determine the dynamics of charged dust particles in the presence of electric and magnetic fields. The electromagnetic force is the sum of the electrostatic force (\vec{F}_E) and the Lorentz force (\vec{F}_B). When a charged particle is immersed in the plasma, it experiences the electrostatic force due to the presence of a static sheath electric field (\vec{E}) near the electrodes. The Lorentz force comes into the picture when this charged particle moves with a velocity (\vec{v}_d) in an uniform or non-uniform magnetic field (\vec{B}). Therefore the electromagnetic force can be represented by

$$\vec{F}_{EB} = \vec{F}_E + \vec{F}_B = Q_d \vec{E} + Q_d (\vec{v}_d \times \vec{B}) \quad (1.14)$$

The electromagnetic force indirectly depends on the size of the dust particles. The amount of charge resides on the dust particles is proportional to the radius of the dust particles. As a result \vec{F}_{EB} is proportional to r_d .

1.2.7.2 Gravitational force (\vec{F}_g)

In the laboratory experiments, the gravitational force \vec{F}_g is one of the strongest forces that act on the micron or sub-micron sized dust particles. It can be expressed as follows:

$$\vec{F}_g = m_d \vec{g} = \frac{4}{3} \pi r_d^3 \rho \vec{g} \quad (1.15)$$

where m_d , ρ , \vec{g} are the mass, mass-density, and acceleration due to Earth gravity, respectively. In the solar and astrophysical environments, the gravitational forces arises from the nearby planet or satellite. As the gravitational force depends on the mass of the dust particles, hence it is proportional to r_d^3 .

1.2.7.3 Ion Drag force (\vec{F}_{id})

The ion drag force (\vec{F}_{id}) acts on the dust particles due to the rate of change of momentum transfer from the dust grains to the plasma particles or vice versa. In a dusty plasma, the ion drag force (\vec{F}_{id}) comes from the momentum exchange between positive ions and dust particles. The ions can transfer their momentum to a dust particle in three possible ways, namely (i) ion impacts, i.e. the collection of ions, (ii) electrostatic Coulomb collisions and (iii) ion fluid flow (collective) effects, which modify or distort the shape of the Debye sheath around the dust particle [57–60]. The ion drag force due to the flow of ions acts on the dust particles in some special experimental configuration, hence it is neglected in this discussion. However, it will be discussed in more detail in Chap. 3.5.2. Therefore, the resultant ion drag force can be represented by

$$\vec{F}_{id} = \vec{F}_{coll} + \vec{F}_{coul} \quad (1.16)$$

The ions which arrive to the dust particles not only contribute to the charging mechanism of dust grains but also transfer momentum to the dust particles. Hence, \vec{F}_{id} can be expressed as follows [52, 61]:

$$\vec{F}_{coll} = m_i n_i \vec{v}_s \vec{u}_i \sigma_{coll}. \quad (1.17)$$

Here, $v_s = \sqrt{u_i^2 + v_{Ti}^2}$ is the net velocity of ions, m_i , n_i , u_i , v_{Ti} is the mass, density, drift velocity and thermal velocity of ion and σ_{coll} is the cross-section associated with the collection of ions. σ_{coll} can be expressed by

$$\sigma_{coll} = \pi b_c^2 = \pi r_d^2 \left(1 - \frac{2eU}{m_i v_s^2} \right), \quad (1.18)$$

where b_c is the maximum impact parameter for ion-dust collection. The contribution of ion drag force from Coulomb collision of ions with dust particles \vec{F}_{coul} is given by [52]:

$$\vec{F}_{coul} = m_i n_i \vec{v}_s \vec{u}_i \sigma_{coul}, \quad (1.19)$$

where the Coulomb collision cross-section can be expressed as:

$$\sigma_{coul} = \pi b_{\frac{\pi}{2}}^2 \ln \left[\frac{\lambda_D^2 + b_{\frac{\pi}{2}}^2}{b_c^2 + b_{\frac{\pi}{2}}^2} \right] \quad (1.20)$$

and $b_{\frac{\pi}{2}} = Q_d e / 4\pi\epsilon_0 m_i v_s^2$ is called the impact parameter for 90° scattering. It is worth mentioning that the ion drag force is proportional to r_d^2 .

1.2.7.4 Neutral drag force (\vec{F}_{nd})

Similar to the ion drag force, the neutral drag force \vec{F}_{nd} acts on the dust particles due to the momentum transfer of neutral to the dust particles. It acts either

as a hindrance to the dust particles while moving through a partially ionized gas medium or favors the dust particle to move. The neutral drag force can be represented by Epstein [62] formula as [52]:

$$\vec{F}_{nd} = -\gamma_{Eps} \frac{4}{3} \pi r_d^2 m_n n_n v_{Tn} (\vec{v}_d - \vec{v}_n). \quad (1.21)$$

Where m_n , n_n , v_{Tn} are the mass, density and thermal velocity of neutrals. \vec{v}_d and \vec{v}_n are the directed velocities of dust and neutral gas molecules, respectively. The value of γ_{Eps} depends upon the type of collision between the neutrals and dust and it varies between 1.0 to 1.4. Similar to ion drag force, the neutral drag force also depends on r_d^2 .

1.2.7.5 Thermophoretic force (\vec{F}_{th})

The thermophoretic force \vec{F}_{th} acts on the dust particles due to the presence of gradient in the temperature of neutrals. The gas molecules on the hot side of the particle have higher thermal speeds than those on the cold side. It results in a net momentum transfer from the gas to the dust particle. The rate of this net momentum transfer is known as the thermophoretic force \vec{F}_{th} . Its magnitude is directly proportional to the temperature gradient and its direction is in the direction of the heat flux, i.e. in the direction opposite to the neutral gas temperature gradient. The expression of \vec{F}_{th} is given by [63, 64]:

$$\vec{F}_{th} = -\frac{32r_d^2 K_n}{15v_{Tn}} \vec{\nabla} T_n. \quad (1.22)$$

Where K_n represents the thermal conductivity and T_n is the temperature of neutral gas. The thermophoretic force directly depends on r_d^2 .

1.2.7.6 Radiation pressure force (\vec{F}_{rad})

The process of gaining energy by dust particles from the laser is attributed to the well-known radiation pressure force (\vec{F}_{rad}). The radiation pressure arises from the exchange of momentum between the particles and the laser electromagnetic field. The radiation pressure force can be defined as the momentum transfer per unit area per unit time for a particular laser intensity I_{laser} and its mathematical expression is [65]:

$$\vec{F}_{rad} = \frac{\gamma \pi r_d^2 I_{laser}}{c}, \quad (1.23)$$

where γ depends upon the processes such as reflection, absorption and transmission and c is the speed of light. Similar to the drag forces and thermophoretic force, the strength of the radiation pressure force depends on r_d^2 .

1.2.7.7 Polarization force (\vec{F}_p)

The polarization force act on the dust grains due to the nonuniform plasma background. It arises due to any kind of deformation of the Debye sheath around the particulates in the background of non-uniform plasmas. As discussed by Hamaguchi and Farouki [66], the polarization force can be expressed as $\vec{F}_p = \frac{1}{4\pi\epsilon_0} Q_d^2 \nabla \lambda_d / 2\lambda_d^2$, where λ_d is the dust Debye length. As shown in Ref. [66], the simplified form of the polarization force is:

$$\vec{F}_p = -\frac{1}{16\pi\epsilon_0} \left[\frac{|Q_d|e}{\lambda_d k_B T_i} \times \left(1 - \frac{T_i}{T_e} \right) \right] Q_d \vec{E}. \quad (1.24)$$

This above expression essentially signifies that the polarization force always acts in the direction opposite to the electrostatic force and it becomes significant for a particle of larger size.

1.3 An overview of earlier works

A dusty plasma comprises of electrons, ions, neutrals, and micron or sub-micron sized charged dust particles. The great diversity in the space and time scales of these constituent components makes for a rich collective dynamics of this medium and has made dusty plasmas an active field of research for the last three decades or so [1,2]. The presence of these additional highly charged and massive species in the plasma can modify the properties of the usual plasma modes and can also give rise to new low-frequency ‘dust modes’ since they involve the dynamics of the dust grains [15,25,27]. The ‘Dust Acoustic Wave’ (DAW) was first theoretically studied by Rao et al [27] and subsequently by several others [15,25]. This mode is a long-wavelength, low-frequency collective oscillation in an unmagnetized dusty plasma in which the electron and ion pressures provide the tension with the inertia provided by the massive and negatively charged dust grains. After the first experimental observation of DAW by Angelo *et al.* [15], a large number of experiments have been carried out worldwide [67–69] to study the modification in the propagation characteristics of DAWs in the presence of various effects. During the past two decades, other longitudinal waves associated with dusty plasma such as Dust Ion Acoustic waves (DIAW) [70–72], Dust Lattice waves (DLW) [73,74], etc. are also extensively studied both theoretically and experimentally.

Kaw and Sen [75] proposed a phenomenological model - a Generalized Hydrodynamic (GH) model which provides a simple physical picture of the effects of strong dust correlations through the introduction of the viscoelastic effect of the medium. In their theoretical model, they have predicted that, unlike in a normal fluid or a conventional plasma, the transverse shear waves can be excited in the

strongly coupled fluid regime of dusty plasma. Later, Pramanik *et al.* [76] and Bandyopadhyay *et al.* [77] experimentally observed the transverse shear waves in a DC glow discharge plasma. These experimental observations reveal strong correlation effects in the medium due to a strong coupling between the particles.

Similar to linear waves, dusty plasmas also support the excitations of non-linear waves and structures in the form of solitary waves [30, 31, 78, 79], shock waves [80–82, 82–84] and voids [34–37] and vortex structures [38, 39]. Dust Acoustic and Dust Ion Acoustic Solitary Waves get excited in a medium when the non-linearity balances dispersion and have been studied widely both theoretically and experimentally [30, 31, 84–88]. Dust Acoustic and Dust Ion Acoustic Solitary Waves are the coherent structures, which can propagate a long distance in a dispersive medium without losing their identity. They even can sustain their properties after mutual collisions. These coherent structures can be modeled using the full sets of fluid equations and studied widely by constructing the Kortweg-de Vries (KdV) equation [44, 47] and by arbitrary amplitude approximation techniques [52, 89].

Another class of non-linear wave that has also been studied extensively is Dust Acoustic and Dust Ion Acoustic Shock Waves [33, 69, 80–83]. Shock waves are highly non-linear structures, which form with a characteristic sudden jump in any one of the physical parameters such as pressure, velocity, temperature, and density. These nonlinear waves get excited when the dissipation (due to collisions or viscosity) in the medium plays a significant role along with non-linearity and dispersion. In dusty plasmas, dissipation can arise either from frequent dust-neutral collisions [33] or dust-dust coupling effects [83]. In a weakly coupled dusty plasma, the dissipation comes primarily from the kinematic viscosity due to frequent dust-neutral collisions and/or dust charge fluctuations [90], whereas for a strongly coupled dusty plasma

the bulk and shear viscosity [33,83] play a crucial role in providing dissipation. The first theoretical approach to understand the propagation characteristics of a shock wave was carried out by Shukla *et al.* [85], where they have used Generalized Hydrodynamic (GHD) equation to derive KdV-Burger equation and found the stationary shock type solutions. In their study, the bulk viscosity provides the dissipation in the medium and its strength decides the solution to be monotonic or oscillatory. Subsequently other authors made significant studies on the propagation characteristics of shock waves [91,92]. All these studies in the past essentially indicate that the dusty plasma is a very versatile medium for studying various collective modes in both linear and nonlinear regimes [93].

Apart from the excitation of linear and nonlinear waves, numerous experimental and theoretical studies have been carried out in flowing dusty plasmas in the past. The motivation behind these studies originates from various hydrodynamic phenomena and astrophysical events. Gavrikov *et al.* [94] performed a fundamental experiment to generate the laminar flow in a dusty plasma liquid by using an Ar^+ laser. From the particle trajectory, they estimated the shear viscosity of a dusty plasma liquid. In another experiment of Flanagan *et al.* [95], the dust particles are used as a tracer to demonstrate the thermal creep flow (TCF) caused by the flow of bulk gas in a closed glass box. In this experiment, the flow in the gas was initiated by heating the wall of the box with the help of a laser. In a similar experiment, Schwabe *et al.* [96] studied the gas dynamics by using dust particles as a tracer in the presence of temperature gradient in the background neutrals. Two types of gas convections namely the Rayleigh Benard convection, and thermal creep flow are observed from the motions of the dust particles. Few experiments have also been carried out to study the flow of dust particles in different experimental con-

figurations [97–100]. In all these experiments, either the flow of ions or neutrals or asymmetric potential was responsible to circulate the particles. In a different set of experiments, Fink *et al.* [101] formed a stable cone-shaped structure of micro-particle in a dc glow discharge plasma using a gas nozzle. They used the strings of microparticles to generate the electric field inside the nozzle.

There is another area that has also been explored in dusty plasmas to initiate various types of flows from laminar to turbulent and generate various types of instabilities associated with these flows. Gavrikov *et al.* [94] generated the laminar flow in dusty plasma liquid by using a laser. Gupta *et al.* [102] generated the Kolmogorov flow in a two dimensional strongly coupled dusty plasma using MD simulations and compared their results using GHD model both in the linear and non-linear regimes. Shear flows have also been generated in the strongly coupled complex fluid using two counter-propagating Ar^+ laser beams by Nosenko *et al.* [103]. Rayleigh Taylor (RT) instability [104], Kelvin Helmholtz (KH) [105] instability, and generation of structures are also investigated in a shear flow driven strongly coupled dusty plasma. Pacha *et al.* [104] studied the Taylor instability in a dusty plasma by the interference of a high-density fluid into a low-density fluid spontaneously. They phenomenologically compared their experimental findings by estimating the linear growth rate of RT instability observed in hydrodynamics. Ashwin *et al.* [105] observed Kelvin Helmholtz instability in molecular dynamics simulations for the first time at the particle level in a two-dimensional strongly coupled dusty plasma. In their study, it is found that the linear growth increases with the increase of the strength of the coupling between the particles.

Flow past an obstacle and simultaneous excitations of nonlinear waves and structures opened up a new research area in the field of dusty plasma. Mor-

fill *et al.* [106] were the first to perform experiments on the flow of a dust fluid around an obstacle at its kinetic level in microgravity conditions. Their experimental observations predict that a dusty plasma can provide a unique tool to model various classical fluids. In a controlled experiment, Saitou *et al.* [81] observed the bow shock formation in the downstream direction when a supersonic flow of dusty plasma is initiated around a thin conducting needle. The bow-like structure was characterized as a shock by the numerical simulation and polytropic hydrodynamics model. In another set of experiments, Meyer *et al.* [107] noticed the formation of the transient bow shock around a biased cylindrical object in a flowing dusty plasma. While flowing from the secondary to the primary dust cloud, it was found that the dust acoustic shock waves were triggered in the upstream direction. Jaiswal *et al.* [83] very recently observed oscillatory shock structures when a highly supersonic flow is generated over a charged object. The shocks are found to propagate in the direction of fluid flow. In continuation, Jaiswal *et al.* [108] also reported an experimental observation of the formation of dynamic structures in a flowing dusty plasma when a supersonic flow was initiated around a spherical metal object. Motivated by all these experiments, Charan *et al.* [109] performed a simulation study of supersonic flow around an obstacle. They observed in their simulation that the transition from primary bow shock propagation in the upstream direction is changed to stationary arc structure and the generation of the secondary bow shock in the downstream direction with the change of Mach number.

As in a hydrodynamic fluid, there are many observations of wake structures in laboratory dusty plasmas [23, 110–113]. These wakes (sometimes termed as Mach cones) are generated when a dust particle moves through a stationary dusty

plasma medium with a subsonic velocity. The first experimental demonstration of the generation of a precursor soliton in a flowing dusty plasma was reported in 2016 by Jaiswal *et al.* [48]. In their study, they observed the spontaneous excitation of precursor solitons when a supersonically moving dusty plasma fluid was made to flow over an electrostatic potential structure. The physical mechanism underlying this phenomenon can be understood in terms of the fluid concept used to explain in hydrodynamic precursors. Sen *et al.* predicted the possibility of the excitation of these fore-wake phenomena in a flowing plasma medium using a forced version of the KdV model equation. Very recently numerical simulation studies were also carried out by Sanat *et al.* [50, 114] to study the propagation characteristics of these fore-wake excitations e.g., the excitation of precursor solitons and pinned (stationary in the laboratory frame) solitons. The topic of fore-wake excitations (precursor waves) has, however, received very limited attention until now.

1.4 Scope and outline of this thesis

In this thesis, we have addressed important issues on the fore-wake excitations in a flowing dusty plasma. In particular the modifications in the propagation characteristics of precursor solitons due to the different shapes and sizes of the charged object over which the dust fluid flows. This study is extended further to excite the pinned solitons in a flowing dusty plasma when the fluid is made to flow over the charged object with highly supersonic velocity. Furthermore, we have also investigated the propagation characteristics of shock waves in an inhomogeneous dusty plasma.

Chapter - 2 is devoted to the detailed description of the Dusty Plasma Experimental (DPEx) device and its associated instrumentation for carrying out the

experiments in flowing dusty plasmas. The plasma and dusty plasma are thoroughly characterized using a single Langmuir probe and an emissive probe. The detailed description of the generation of flow in dust fluid and the measurement techniques are also provided.

Chapter - 3 describes the study the dynamics of dust particles when the flow in the dust component is induced by the neutrals. The characteristics of the dust dynamics are investigated as a function of the differential gas flow rate, the background neutral pressure, the dust particle size, and the neutral species of the gas. The asymptotic steady-state flow velocity of the injected micron-sized dust particles is found to increase with an increase in neutral flow velocity and decrease with an increase in the background pressure. Furthermore, this velocity is seen to be independent of the size of the dust particles but decreases with an increase in the mass of the background gas. A simple theoretical model, based on estimates of the various forces acting on the dust particles, is used to elucidate the role of neutrals in the flow dynamics of the dust particles.

Chapter - 4 describes a new technique to measure the potential profile around the charged object by using the dust particles as dynamical micro-probes. The tracer particles are made to flow over the grounded wire by suitable variations in the background gas flow. By a visual tracking of the individual particle trajectories, the potential values at different axial and radial locations are directly estimated by using energy conservation arguments. The results agree very well with conventional probe-based measurements.

Chapter - 5 is devoted to the modifications in the propagation characteristics of precursor solitons due to the different shapes and sizes of the potential hill (floating wire) over which the dust fluid flows. The size (height and width) of the potential

hill is varied by drawing current through it. With a decrease in the height of the potential hill, the amplitude, velocity, and number of excited precursor solitons are found to decrease, whereas the widths of the solitons are seen to increase. To examine the effect due to the shape of the potential profiles, the wire is replaced by a triangular object. Only trailing wakes are seen to be excited when the dust fluid faces the linearly increasing slope of the potential profile, whereas both solitons and wakes get excited when the object is placed with the sharp edge facing the flow. All the experimental findings qualitatively agree with numerical solutions obtained with different source terms in the forced-Korteweg de Vries model equation.

Chapter - 6 focuses on the first experimental excitation of pinned solitons in a dusty plasma flowing over a charged obstacle. Under appropriate conditions, non-linear stationary structures are observed in the laboratory frame that corresponds to pinned structures moving with the speed of the obstacle in the frame of the moving fluid. A systematic study is made on the propagation characteristics of these solitons by carefully tuning the flow velocity of the dust fluid by changing the potential height of the charged object. It is found that the nature of the excited structures changes from a single-humped one to a multi-humped one and their amplitudes increase with an increase of the flow velocity of the dust fluid. The experimental findings are then qualitatively compared with the numerical solutions of a model f-KdV equation.

Chapter - 7 is concerned with an experimental investigation of propagation characteristics of shock waves in an inhomogeneous dusty plasma. Initially, an equilibrium density inhomogeneity in the dust fluid is created by introducing an imbalance in the pumping and the gas feeding rates. Dust Acoustic Shock structures are then excited in this inhomogeneous dusty plasma by a sudden compression

in the dust fluid. The amplitude of a shock structure is seen to increase whereas the width broadens as it propagates down a decreasing dust density profile. A modified-KdV-Burger equation is derived and used to provide a theoretical explanation of experimental findings.

Chapter - 8 provides an overall summary of the work carried out in this thesis. An attempt is made in this chapter to identify some possible issues that merit future investigation.

2

Experimental set-up, production and characterization of plasma and dusty plasma

All the experiments discussed in Chap. 1 are performed in a tabletop versatile Dusty Plasma Experimental (DPEx) device. DPEx device is built at the Institute for Plasma Research to conduct the experiments associated with flowing complex plasma. The detailed descriptions of the geometry, size, and dimension of the device are also presented in Ref. [115]. It is an inverted Π shaped device whose layout is inspired by PK-4 experimental device but the dimensions of the vacuum vessel, electrode configuration and mechanism of plasma generations are quite different. Moreover, the pumping system, gas feeding system are installed in a different way to get the precise control of the flow of dusty plasma. The dimension of the system is designed in such a way so that all the length scales like collision mean free path, plasma Debye length, the wavelength of waves and the flow-induced

structures can be accommodated and studied without any interruption. The size of the chamber is also chosen properly so that a homogeneous long dust cloud can be formed to conduct flowing dusty plasma experiments.

This chapter is organized as follows. The first section (Sec. 2.1) describes the details of the experimental set-up, accessories, and instrumentation used to initiate the plasma as well as dusty plasma. Different probes used to diagnose the plasma is described in Sec. 2.2 whereas in Sec. 2.3 optical diagnostics are presented. Plasma and dusty plasma production and their characterization are described in Sec. 2.4, 2.5 and 2.6, respectively. The flow generation mechanisms used to conduct the flow-related experiments are described in Sec. 2.7 and the flow velocity measurements are described in and Sec. 2.8. A concluding remark of this chapter is given in Sec. 2.9.

2.1 Experimental set-up

In this section, we describe the main components of the DPEx device to execute the experiments associated with excitations of waves and structures using flowing complex plasmas. The schematic of the DPEx device is shown in Fig. 2.1. This section includes the descriptions of the vacuum chamber (Subsec. 2.1.1), pumping and gas feeding systems (Subsec. 2.1.2), powered electrodes (Subsec. 2.1.3) and confining strips (Subsec. 2.1.4) to initiate the plasma using power supply (Subsec. 2.1.5), dust particles (Subsec. 2.1.6), dust dispenser (Subsec. 2.1.7) used in the experiments. They will be discussed subsequently in the following subsections.

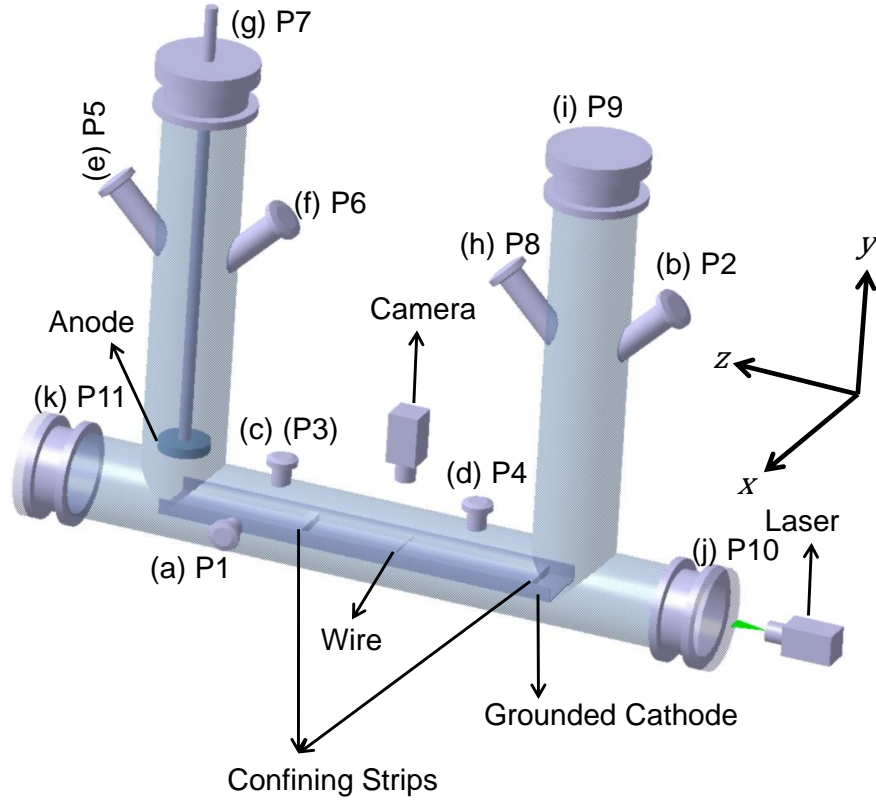


Figure 2.1: A schematic of the experimental set up for performing flowing dusty plasma experiments. Ports P1 and P2 are used for Gas feeding. Port P3 is used either for installation of different probes or Gauge. Port P4 is used to attach Dust Dispenser. Port P5 is made for Pumping port and used to attach the rotary pump. Gauges are attached in Ports P6 and P8. Anode is hung axially through Port P7. Ports P9 and P11 are closed. Port P10 is used for cathode insertion and for shining the laser axially.

2.1.1 Vacuum chamber

All the experiments that are presented in this thesis are executed in the DPEx device whose schematic diagram is shown in Fig. 2.1. The vacuum vessel consists of three Pyrex glass tubes to give the device an inverted II-shape. The main tube in which all the experiments are performed has a length of 65 cm and an inner radius of 8 cm. Two other auxiliary tubes are aligned vertically with the main tube

having a length of 30 cm and has the same inner radii as of the main chamber. The vacuum vessel is placed on an optical table in such a way that the main tube remains perpendicular to the gravity. The purpose to use the optical table is to absorb all kinds of mechanical vibrations during the experiments. The optical table also facilitates the DPEX device to align perfectly to conduct dusty plasma experiments. Two auxiliary tubes of DPEX device are used to attach the pump at port P5, gas flow meter and gas dosing valve at ports P2 and P1, respectively. Pressure in the vacuum chamber is measured by a couple of Pirani gauges, which are attached to port P8 and port P3. An anode is hung axially from port P7 of one of the auxiliary chambers, whereas a long tray cathode is inserted axially in the main chamber through port P10. A dust dispenser is attached to port P4 to introduce the dust particles into the main chamber. Different electrostatic probes such as single Langmuir probe, emissive probes are installed at ports P3, P4 and P10 to measure the plasma parameters radially and axially. All the radial ports of the secondary chamber that are unused are covered with Poly-ether Ether Ketone (PEEK) to avoid hollow cathode discharges.

2.1.2 Pumping and gas feeding system

To conduct experiments in plasmas as well as in dusty plasmas, creating a vacuum in the experimental chamber is very important and various types of vacuum pumps are used depending upon the requirements. In the present set of experiments, we have used a rotary pump (ED-18, pumping speed = 250 lit/min and power 0.5 HP) to evacuate the vessel. The rotary pump is attached to one of the radial ports (port P5) of the left auxiliary chamber (see Fig. 2.1) through a bellow. One gate valve is also attached to the mouth of the rotary pump to control the pumping

speed. It can also be used to disconnect the pump from the chamber. The base pressure is achieved to ~ 0.1 Pa by using this pump. During the experiments, the gate valve is kept partially closed to balance the pumping speed and the gas feeding rate and to maintain a constant working pressure in the chamber.

A couple of Pirani gauges are used and attached to (see Fig. 2.1) ports P3 and P8 to measure the working pressure/base pressure and also the pressure difference in between the main chamber and secondary chamber. An Argon gas cylinder of 99.99% purity attached to Port P1 through a mass flow controller to feed the gas into a device. The flow meter serves to feed the gas in a controlled way which is tuned by a computer through an RS-232 cable that maintains the working pressure (p) 9–18 Pa. The gas flow speed is controlled precisely by a step of 2.75 sccm/min. In some of the experiments, the Argon gas is also inserted through another gas port P2 of the right auxiliary chamber to initiate a flow in a dusty plasma.

2.1.3 Powered electrodes

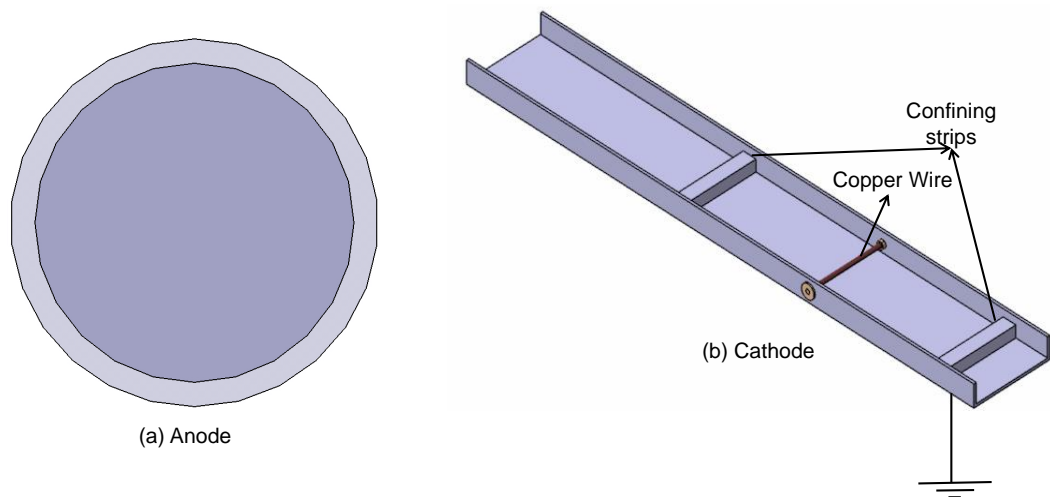


Figure 2.2: Schematic of (a) anode and (b) cathode electrodes used to generate the plasma

A circular metallic disc is served as anode and long metallic tray with angled ends served as grounded cathode whose schematic is shown in Fig. 2.2. The anode is made up of stainless steel (SS-304) having a circular shape of radius 2 cm and thickness 5 mm. It is hung from the axial port P7 of the left auxiliary glass chamber. The anode is covered with a ceramic cap to prevent the micro arcing from its sharp edges.

A SS tray of length 400 mm width 60 mm and thickness 2 mm is placed along the axis of the main chamber which is used as a grounded cathode. The long tray shaped cathode makes the plasma uniform, which helps the dust cloud to be uniform and long. The bent ends of the cathode provide the radial confinement to dust particles by their radial electric field.

2.1.4 Confining strips

Confining strips, as the name suggests, are used to confine the dust particles in the axial direction. In all our experiments, a couple of metallic SS cuboid strips of dimension 60 mm \times 12 mm \times 5 mm are placed on the grounded cathode as shown in Fig. 2.2(b). During the experiments, one of the strips is placed at the right edge of the cathode whereas another one is kept at distance nearby to the anode. The distance between the two strips can be changed depending upon the experimental requirement. As the strips are placed on the grounded cathode, they remain in the grounded potential and confine the particle in the axial direction due to the sheath electric field around them. A copper wire of diameter 1 mm and length 60 mm radially attached to the cathode at a distance of 20 cm from the its right edge. The wire can also be used for axial confinement depending upon the potential applied to it. In some of the experiments, the wire also serves as a charged object to

perform experiments on the excitation of non-linear waves/structures in a flowing dusty plasma.

2.1.5 Plasma discharge power supply

The discharge is initiated between the circular anode and the grounded tray cathode using a Direct Current (DC) power supply. The DC power supply used in our experiments has a voltage rating from 0 to 2 kV and a current rating from 0 to 500 mA. The power supply is protected by connecting a current limiting resistor of 2 k Ω resistance in series with the power supply and anode. A couple of digital panel meters (DPM) on the front panel of the power supply help us to measure the discharge voltage and discharge current. In addition, we have also used a couple of multimeters to measure the discharge parameter precisely. A high voltage, ranging from 290 V to 360 V, is applied to initiate a DC glow discharge Argon plasma at a working pressure of 9 Pa to 15 Pa.

2.1.6 Dust particles

To create a dusty plasma, we have used either micron-sized poly-dispersive Kaolin particles or mono-dispersive Melamine Formaldehyde dust particles depending on the experimental requirements. Melamine Formaldehyde (MF) having diameters (a) $10.66 \pm 0.01 \mu\text{m}$, $8.90 \pm 0.01 \mu\text{m}$ and $4.38 \pm 0.01 \mu\text{m}$ particles with mass density 1.51 g/cm^3 are used. These particles are uniform in shape and having excellent mono-dispersivity. These particles are used to study the dynamics of dust particles induced by neutral flow as discussed in Chap. 3. They are also used to measure the potential profile around a charged wire which is discussed in Chap. 4. These particles are injected into the plasma using a dust dispenser as

discussed in the next Sec. 2.1.7.

Poly-dispersive Kaolin particles having wider dispersion 2–5 μm are used in the excitation of linear and nonlinear waves as discussed in Chaps. 5, 6 and 7. Just before closing the chamber, these particles are sprinkled on the cathode tray uniformly in between the wire and the right confinement strip or in between the two confinement strips depending upon the experimental necessity. Due to size variation, they levitate at different layers above the cathode and form a large dense three-dimensional dust cloud as soon as the plasma initiated. This highly dense dust cloud is used for conducting experiments on the collective excitations, flow-induced structures, etc..

2.1.7 Dust dispenser

A dust dispenser is used to dispense the mono-dispersive (Melamine Formaldehyde) particles into the plasma. It is connected to one of the radial ports (Port P4) of the main chamber (see Fig. 2.1). It has a cap where the particles are loaded before starting the experiments. The front part of the cap is covered by a mesh having a very small inter-grid spacing (e.g. 15 μm for the particles of diameter 10.66 μm) that can filter the particles and allow them to fall easily into the plasma. Several steel balls of 1 mm diameter are also loaded in the cap to avoid coagulation. These balls also help to throw the particles individually. The dust dispenser is connected to a trigger circuit which is operated by a Lab-View software using a computer.

2.2 Diagnostics of plasma

Plasma is generated by setting the working gas pressure and powered the electrodes using a DC power supply. After the production of plasma, the plasma parameters like plasma density, electron temperature, floating potential, plasma potential, and electron distribution function are measured using different probes. We have used a single Langmuir probe and an emissive probe to diagnose the plasma in the absence of dust. The single Langmuir probe is used to measure the plasma density, electron temperature, floating potential, plasma potential, and electron distribution function and from there the radial profiles of plasma density and electron temperature. Whereas, an emissive probe is used to obtain the radial profiles of floating potential, plasma potential and hence the electric field. These probes are discussed in detail in the following subsections.

2.2.1 Langmuir probe

A cylindrical Langmuir probe made up of tungsten and insulated by the ceramic holder is used to measure plasma density, electron temperature, floating potential, plasma potential, and electron distribution function. A photograph of the Langmuir probe tip is shown in Fig. 2.3 whereas its electric circuit is shown in Fig. 2.4.

A cylindrical tungsten wire of diameter 1 mm and length 10 mm is used as a single Langmuir probe in the present set of experiments. The dimensions are chosen wisely so that the conventional probe theory holds good in a collisionless plasma. The probe is biased using a RAMP power supply and the probe current is measured across a resistor of resistance 5.5 k Ω . Depending upon the discharge condition, the current drawn by the probe is different at different sweep voltage.

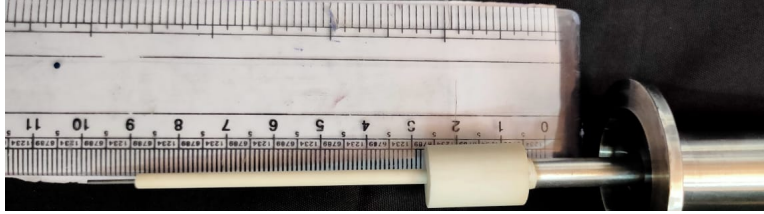


Figure 2.3: Photograph of Langmuir probe exposing the tip only and covered with ceramic is shown.

The potential applied to the probe at which the net probe current becomes zero is called the floating potential (V_f). After measuring the floating potential, the probe is biased over the range of bias voltage from $V_f - 100$ to $V_f + 100$ V to obtain the full V-I characteristics starting from the ion saturation region to the electron saturation region. The different regions of V-I characteristics of the Langmuir probe help us to estimate the plasma parameters which are discussed in Subsec. 2.5.1. The circuitry of a single Langmuir probe power supply is discussed in detail in Ref. [116].

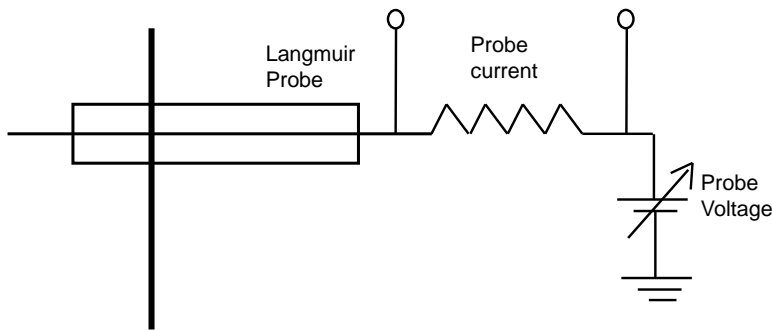


Figure 2.4: A schematic of the Langmuir probe circuit.

2.2.2 Emissive probe

We have also used an emissive probe to get the precise measurement of plasma potential V_p in the plasma as well as in the sheath. The radial profile of plasma

potential from the bulk to the sheath regions is used to estimate the electric field profile. It, in turn, helps us to estimate the value of charge acquired by the dust particles. A photograph of the emissive probe is shown in Fig. 2.5. Similar to the Langmuir probe, the emissive probe is also made up of tungsten wire of diameter 0.125 mm and length 8 mm. The tungsten wire is made in the form of a loop and its ends are inserted in a twin-bore ceramic tube and connected to the copper wire to make the electrical contacts. It is ensured that the contact points are good enough such that it can withstand a high temperature when the high current is drawn by the tungsten wire. The probe is made to expose in the plasma and subsequently, a high current is passed through it using a high current DC power supply (15 V, 7 A). When the probe is heated up and as a result, it emits electrons through thermionic emission.



Figure 2.5: A photograph of emissive probe used in the experiments.

An emissive probe, which is widely used to measure the plasma potential [117], can be operated by using three different techniques. The simplest method ‘floating-point technique’ is followed to measure the plasma potential in our experiments. The circuit diagram to operate the emissive probe in this method is shown in Fig. 2.6. In this technique at zero-emission current (cold emissive probe), the emissive probe acts as a single Langmuir probe. The floating potential at that condition is measured by connecting a resistor of very high resistance ($R_1 = 70 \text{ M}\Omega$) in between one lead of the emissive probe and another resistor of lower resistance

($R_2 = 10 \text{ k}\Omega$). The other lead of R_2 is connected with ground potential. At cold conditions, the current through the resistance R_1 is obtained by measuring the voltage across R_2 using a multimeter. The floating potential is then measured by using the principle of the potential divider. The same technique is then followed for a hot emissive probe for different values of emission current to measure the floating potential. The plasma potential is obtained at which the floating potential remains constant with the emission current as discussed in Ref. [117]. The radial profiles of plasma potential measured using this technique are described in Sec. 2.5.3.

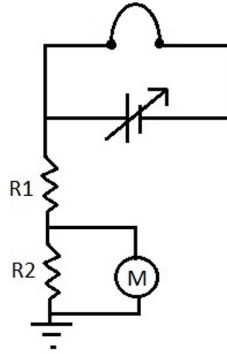


Figure 2.6: A schematic diagram of emissive probe circuit operated in floating-point technique.

2.3 Diagnostics of dusty plasma

The main diagnostic used to diagnose the dusty plasma is the optical diagnostic. It is a combination of a laser and a couple of CCD cameras. The laser light is used for visualizing the particles whereas the cameras are used for recording the dynamics of the dust particles by capturing the Mie-scattered light from the particles. Due to the low charge to mass ratio, the dynamics of the dust particles become very slow which facilitates us to record the motion of the dust particles by a CCD

camera having a very low frame rate (30-200 fps). Therefore in dusty plasma, video imaging is the primary source of acquiring the data for studying the various collective phenomena such as the formation of structure, excitation of linear and non-linear waves, *etc.*. Both the cameras in our experiments are connected to a high-speed workstation using firewire cables to store the images which are captured by the cameras. Later, the images are analyzed using various software such as ImageJ, IDL based super Particle Identification and Tracking (sPIT) code [118], MATLAB based Particle Image Velocimetry (PIV) [119] to study dynamics of dust particles and collective excitation.

2.3.1 Imaging of dust particles

The dust particles are illuminated by a green laser light having a wavelength of 532 nm. The laser power can be tuned from 0-100 mW at that wavelength. The point laser light source is converted into a line source by attaching a Powell lens in front of the laser. It helps to shine the dust cloud either in the y-z or x-z plane. The thickness of the laser line is made to be less than 1 mm at a distance of 50 cm with a width of 60 mm. The dimension of the line source is good enough to illuminate the complete dust cloud either in one of the planes. It is to be noted that in our experiments, two lasers are used simultaneously, One laser is used to illuminate the x-z plane whereas there is another laser having the same specification is situated on the left side of the chamber which is used to illuminate the y-z plane.

The Mie scattered light from these dust particles is captured by a couple of CCD cameras. The high-speed camera having 60 fps and 1000×1000 pixel resolution is used either from the top or sideways depending upon the experimental requirement. The capturing frame rate can be further increased up to 200 fps by lowering its

field of view (FOV). A couple of C mount zoom lenses having focal length 25 mm and 16 mm are attached in front of the camera to adjust the aperture and magnification. The magnification can also be increased by connecting the C rings in series with the lens. In some of the experiments, another camera with a lower frame rate (30 fps) and a higher resolution (2000 pixel \times 2000 pixel) is also used.

2.3.2 Data storage and analysis

As discussed in Sec. 2.3, the raw image data is stored in a computer by a cable that is connected to the PCI Express Host Adapter card mounted on the motherboard of the workstation. The camera is operated by a software (Vimba 2.0), which is compatible with the Windows-10 operating system. The high-quality images are stored in the computer in ‘jpeg’ or ‘png’ formats by adjusting the shutter speed, resolution, gain, frame rate with the help of the software.

To analyze the stored images we have used various software like ImageJ, sPIT, and PIV. ImageJ is used for spatial calibration. For particle level experiments (i.e. the experiments which are performed with very few particles) as discussed in Chap. 3 and Chap. 4, we have used IDL based super Particle Identification Code to extract the coordinates of the particles over the time. It is an efficient and powerful code to track individual particles for several frames to get the particle trajectories. We have also used MATLAB based open-access Particle Image Velocimetry (PIV) code in the rest of the chapters (Chaps. 5–7) in which the flow-related excitation of nonlinear waves are discussed. This code is mainly used to determine the velocity of the dust particles in a flowing dusty plasma.

2.4 Plasma production and its characterization

To conduct the experiments, initially, the vacuum chamber is evacuated at a base pressure of 0.1 Pa by the rotary pump as described in detail in Subsec. 2.1.1. While pumping down to the base pressure the gate valve connected with the rotary pump is kept fully open. After attaining the base pressure, the gate valve is closed partially (approximately 20%) and the Argon gas is introduced in the chamber using a mass flow controller to set the working pressure at $p= 8\text{-}20$ Pa as discussed in Subsec. 2.1.2. A high voltage ranging from 250–400 V is applied between the electrodes using a DC power supply to initiate a DC glow discharge Ar plasma. A single Langmuir probe and an emissive probe are used to characterize the plasma thoroughly to obtain the plasma parameters over a range of discharge conditions. The detailed construction and the electrical circuit of these probes are described in the subsequent Subsec. 2.2.1 and 2.2.2, respectively.

2.5 Characterization of plasma

The plasma parameters like plasma density, temperature, floating potential and plasma potential are measured from the V-I characteristics curve of a single Langmuir probe. The typical probe current from the Langmuir probe is shown in Fig. 2.7. The curve can be divided into three regions: ion saturation, electron saturation, and transition regions. The potential at which the total current drawn by the probe becomes zero is known as floating potential (V_f). In the electron saturation region, the current drawn by the probe is mostly by the electrons as the probe is biased by a large positive potential with respect to the floating potential whereas, at ion saturation regions, the ion current dominates over the electron cur-

rent as the probe is biased by the negative potential with respect to the floating potential. The region at which the probe current rises significantly with a small change in the bias voltage is called a transition region. The knee on the probe current corresponds to a potential called plasma potential (V_p) where the electrons and ions come to the probe with their thermal velocities. All the plasma parameters are determined from these three different regions of the V-I characteristics curve. The floating potential (V_f) is determined at first by noting down the bias voltage at which the probe current becomes zero. The intersection of tangents drawn on the electron saturation region and the transition region in the voltage axis gives the plasma potential (V_p).

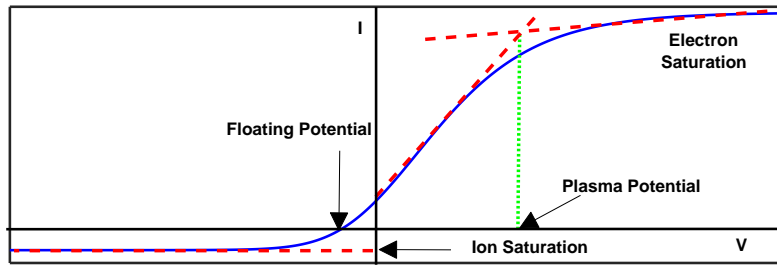


Figure 2.7: The ideal I-V characteristics of Langmuir probe.

The ion saturation region is a region at which the ion current becomes almost constant and can be used to obtain the plasma density using the following expression:

$$I_{is} = 0.61en_i v_{Bohm} A_{probe} \quad (2.1)$$

where, n_i is the ion density, $v_{Bohm} = \sqrt{\frac{k_B T_e}{m_i}}$ is the Bohm velocity, m_i is the ion mass, and A_{probe} is the probe area which is exposed to the plasma. Before estimating the plasma density from the Eq. 2.1, the plasma temperature is calculated. The inverse of the slope of $\log(I - I_{is})$ Vs probe bias voltage is used to determine the electron temperature.

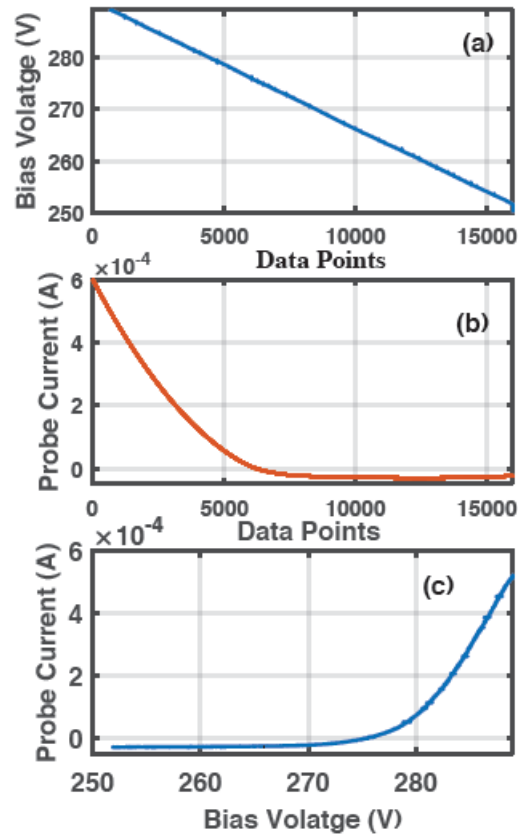


Figure 2.8: Variation of (a) bias voltage applied to the probe (b) current drawn by the probe with time. (c) Typical characteristics of a Single Langmuir probe.

Fig. 2.8 (a) and (b) shows the typical bias voltage along with the current drawn by the probe, respectively for a discharge voltage of 320 V and pressure of 12 Pa. The probe current is estimated by measuring the voltage drop across a resistance of 5.5 k Ω . In this set of experiments, the probe is installed at port P4. Fig. 2.9 shows the variation of floating and plasma potentials with discharge voltage at a constant pressure of 14 Pa. One can see that plasma and floating potentials follow the increasing trend with the discharge voltage which is also reported by Jaiswal. *et. al.* [115].

Plasma density and electron temperature are also plotted in Fig. 2.10 for the same range of discharge conditions. One can see that plasma density increases

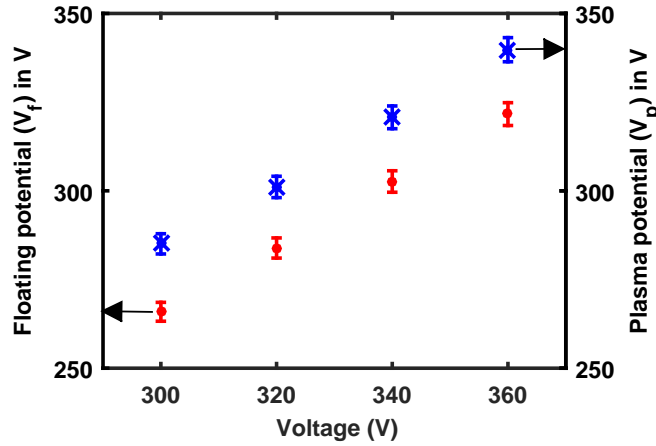


Figure 2.9: A plot showing the variation of floating potential and plasma potential with discharge voltage.

whereas electron temperature decreases with the increase in discharge voltage. At higher discharge voltage, the discharge current increases due to the higher ionization, which leads to the enhancement of plasma density. Due to the higher electron density, the electron-neutral mean free path decreases, as a result, the electrons undergo frequent collisions with neutrals. It essentially reduces the electron temperature with increase of the discharge voltage.

The electron temperature and plasma density are also measured for different background pressure at a given discharge voltage as shown in Fig. 2.11. One can see that the density and temperature follow a similar trend as shown in Fig. 2.10. In this set of experiments, the plasma density increases with the increase in background pressure. At higher pressure, the extent of ionization becomes more, which results in a rise in the discharge current. However, the temperature decreases with the increase of background pressure as the electrons lose their average kinetic energy by undergoing frequent collisions with the neutrals at higher pressure.

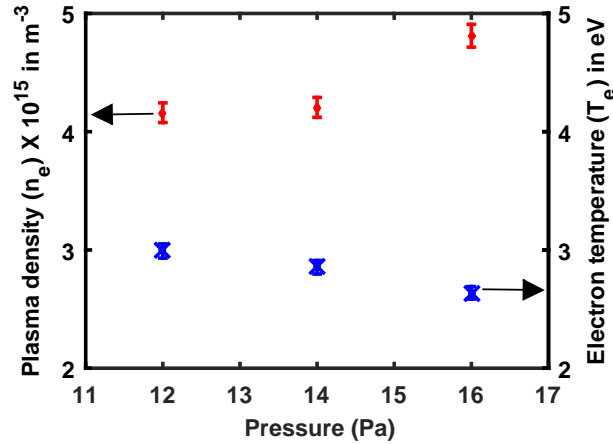


Figure 2.10: A plot showing the variation of plasma density and electron temperature with background pressure.

2.5.1 Measurements of radial profile by Langmuir probe

As discussed, the plasma parameters are very sensitive to the discharge parameters such as on the background pressure and the discharge voltage. In this section (Sec. 2.5.1), we discuss the measurements of these plasma parameters when the probe is scanned radially over a given discharge condition. The typical radial profiles of plasma density and electron temperature are shown in Fig. 2.12 for a given discharge condition, $p=16$ Pa, and $V_d=360$ V. It is to be noted that these experiments are carried out by installing the probe at port P4. The probe is scanned radially very precisely in the interval of 0.5 cm from bottom to top. The ‘0’ position represents the position of the cathode and the different radial positions correspond to the location of the probe tip as shown in Fig. 2.12. One can see from Fig. 2.12 that plasma density decrease as we move away from the cathode whereas the temperature follows the increasing trend. The first point in Fig. 2.12 is taken at ~ 2 cm far from the cathode where the cathode sheath ends. The Langmuir probe can not be used in the sheath region to measure the plasma parameters as

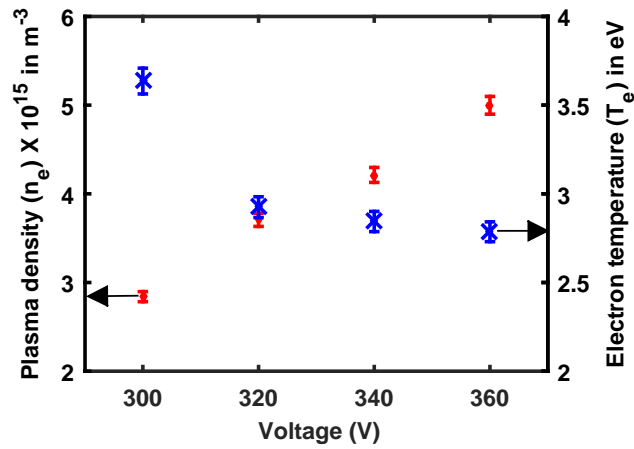


Figure 2.11: A plot of plasma density and electron temperature for different discharge voltages.

the probe theory doesn't hold good in this region. The axial profiles of plasma density and electron temperature have already been carried out and described in Ref. [115].

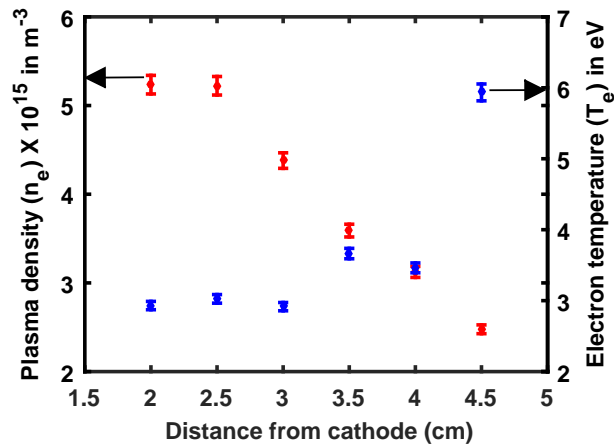


Figure 2.12: A plot of plasma density and electron temperature at different radial locations.

2.5.2 Distribution function

The Electron Energy Distribution Function (EEDF) is also a very important parameter which can be estimated using a single Langmuir probe. The variation of probability of finding electrons with energy ϵ and $\epsilon + d\epsilon$ with electron energy can be used to find out whether the electrons follow a certain kind of distribution. The multiple peaks in EEDF also provide information about the presence of hot and cold electrons or two temperature electron species in a plasma. EEDF is estimated from the current drawn by the Langmuir probe. The expression [120] of electron energy distribution function is given as:

$$f(\epsilon) = 2(2m_e)^{1/2}(e^3 A_{probe})^{-1}(\epsilon)^{1/2} \frac{d^2 I}{dV^2} \quad (2.2)$$

where, m_e , A_{probe} , e , $\frac{d^2 I}{dV^2}$ are the mass of the electron, area of the probe, electronic charge, respectively.

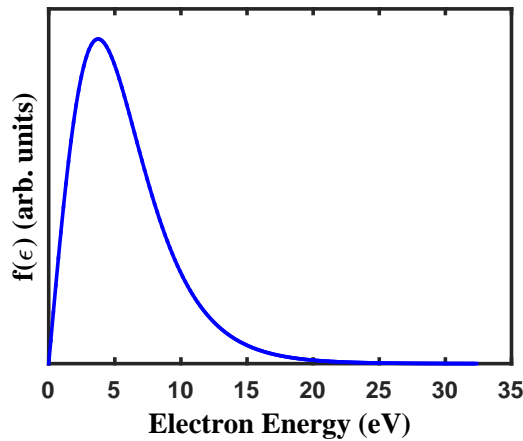


Figure 2.13: A plot of electron energy probability distribution function (EEDF) for $p = 14$ Pa and $V = 300$ V

The probability distribution $f(\epsilon)$ is defined by the ratio of EEDF to $\sqrt{\epsilon}$ and

plotted in Fig. 2.13 for pressure 14 Pa and discharge voltage 300 V. The plasma parameters like plasma density and temperature can be calculated with the help of $f(\epsilon)$ using the kinetic theory as given below:

$$n_e = \int_0^{\text{inf}} f(\epsilon) dE \quad (2.3)$$

$$T_e = \int_0^{\text{inf}} \epsilon f(\epsilon) d\epsilon \quad (2.4)$$

The electron temperature estimated from electron energy distribution function using Eq. 2.4 is 3.8 eV whereas the electron temperature calculated from the slope of Langmuir probe V-I characteristics at the same discharge condition is 3.5 eV. Another important plasma parameter, electron density is also estimated from EEDF using 2.3, which comes out to be $\sim 7 \times 10^{14} / m^3$. The plasma density measured from the ion saturation current of the Langmuir probe is $\sim 1 \times 10^{15} / m^3$. The estimations of electron temperatures and the electron density using EEDF are in good agreement with V-I characteristics of the Langmuir probe.

When the electrons are not in thermal equilibrium, the Maxwellian distribution function may not be suitable to describe those electrons. Druyvesteyn distribution function is one type of such non-equilibrium or non-Maxwellian distribution function, which can be used to represent the plasma species like electrons having an always higher temperature than ions and neutrals. The normalized expression for Druyvesteyn distribution function can be expressed as [121]:

$$f_D(\epsilon) = \frac{0.5648 n_e}{(k_B T_e)^{3/2}} \sqrt{\epsilon} \exp \left[-0.243 \left(\frac{\epsilon}{k_B T_e} \right)^2 \right] \quad (2.5)$$

The basic distinction between the Maxwell and Druyvesteyn distribution functions

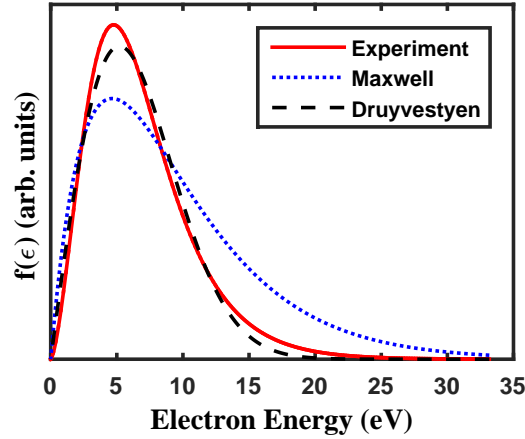


Figure 2.14: Maxwell, Druyvestyen and experimentally obtained distribution functions.

is the exponent in the argument of exponential function. As shown in Eq. 2.2 and Eq. 2.5, the exponent for Maxwellian distribution function is one whereas for Druyvestyen distribution function, it is two. It is reported in the literature that for low electron energy, the Druyvestyen distribution function represents the experimental data better than the Maxwellian distribution function [121]. In our experiments also, (as shown in Fig. 2.14) the Druyvestyen distribution function is in better agreement with the experimental distribution function than that of Maxwell distribution function.

2.5.3 Measurements of plasma potential and floating potential by emissive probe

An emissive probe is also used in our experiments to obtain the radial plasma and floating potential profiles to estimate the radial sheath electric field. The detailed circuitry and their construction have already been described in Subsec. 2.2.2. The simplest technique ‘floating-point technique’ is used to measure the plasma po-

tential, which is also extensively used by other [117]. In this method, the floating potentials are measured by passing a different amount of emission currents through the filament as shown in Fig. 2.14. As the emission current increases, the sheath around the probe diminishes and as a result, the potential across the resistance R_1+R_2 increases. When the sheath around the probe gets completely nullified by

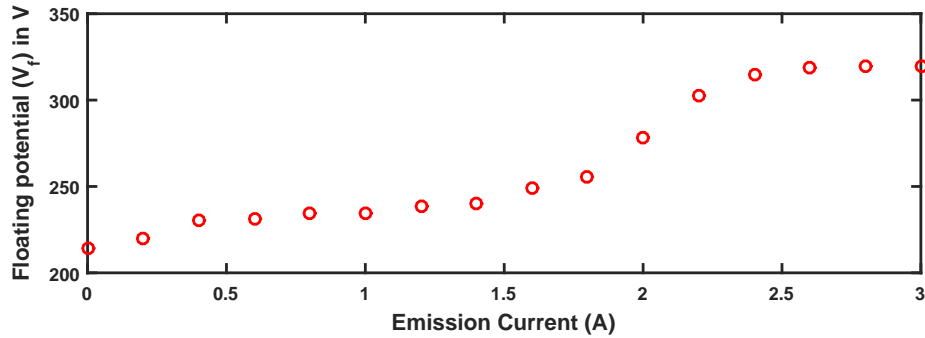


Figure 2.15: Measurement of plasma potential using emissive probe by floating point technique.

the filament electrons, the floating potential attains the plasma potential. Thereafter the potential does not increase with the further increase of emission current instead it takes a constant value. Fig. 2.15 shows the variation of floating potential with the emission current at $V_d = 340$ V and background pressure $p = 12$ Pa. One can see that as the emission current increases, the floating potential increases from 220 V and it saturates to a plasma potential at 320 V when the emission current reaches to a value close to 2.5 A. One can see that the floating potential measured using Langmuir probe is always higher compared to the measurements made by emissive probe. This is because, at zero-emission current, the emissive probe still draws some current from the plasma. For a precise measurement of floating potential, one needs to attach a resistor (R_1) of higher resistance. However, in these specific set of experiments, we measure the plasma potential precisely using an

emissive probe.

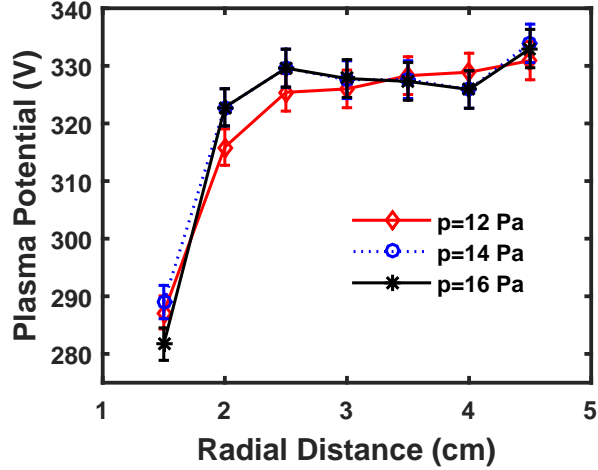


Figure 2.16: Radial profile of plasma potential for three different pressure and discharge voltage 360 V.

The plasma potential is then measured at different radial locations from cathode sheath to bulk plasma using the same techniques. In this set of measurements, the emission current is kept constant at 3 A, so that in all the locations the sheath around the probe gets nullified and the probe measures the actual plasma potential. The radial profiles of the plasma potential for three different pressures are shown in Fig. 2.16. The first point corresponds to the measurement near the cathode whereas the last point in Fig. 2.16 represents the plasma potential at the bulk plasma. It is seen that the plasma potential does not change much at bulk plasma when the pressure is changed from 12 to 16 Pa. It is due to the fact that the electron temperature does not change significantly over the narrow range of background pressure. As the plasma potential explicitly depends upon the electron temperature, hence it remains almost constant over the range of background pressure. Interestingly, the plasma potential falls very rapidly when the probe is scanned from bulk plasma to the cathode sheath, which essentially indicates there

exists a sheath near the cathode. The sheath electric field can be calculated from the first derivative of the plasma potential with respect to radial distance. It is clear from Fig. 2.16, the plasma potential falls rapidly for $p=16$ Pa compare to $p=12$ Pa, which signifies that the sheath electric field at $p=16$ Pa is higher than that of $p=12$ Pa. At a given discharge voltage, the electric field values change in the range of $0.7 - 2 \times 10^5$ V/m when the pressure is changed from 12 Pa to 16 Pa.

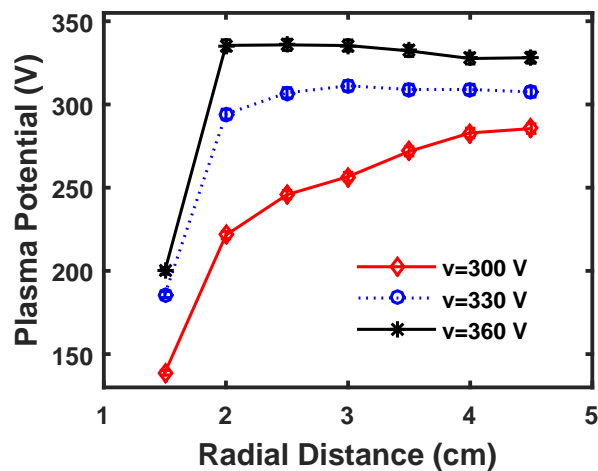


Figure 2.17: Radial profile of plasma potential for three different discharge voltages and fixed background pressure 14 Pa.

The same experiment is repeated to obtain the radial profiles of plasma potential for three different discharge voltages at 300 V, 330 V and 360 V to examine the dependency of plasma potential on the discharge voltage at a constant pressure $p=14$ Pa. Fig. 2.17 depicts the radial profiles of plasma potential for these three discharge voltages. For a given discharge voltage the plasma potential remains constant at bulk plasma whereas it falls rapidly when the probe enters into the cathode sheath as shown in Fig. 2.16. In addition, it is also seen that the plasma potential is always higher for higher discharge voltages. It is due to the fact that at higher discharge voltage the degree of ionization becomes higher which in turn

increases the loss of electrons. As a result, the plasma becomes more and more positive with respect to the grounded cathode with the increase of the discharge voltages. The sheath electric fields can be calculated from the potential profiles and it is found that it is higher for higher discharge voltages. At a given pressure, the electric field values change in the range of $2 - 9 \times 10^5$ V/m when the discharge voltage is changed from 300 V to 360 V. It is to be noted that the axial profiles of plasma potentials have already been obtained for the DPEx device and reported in Ref. [115].

The following table (Tab. 2.1) provides the range of plasma parameters for the range of discharge voltages (V) = 290–370 V, discharge currents (I_d) = 2–11 mA and working pressures (p) = 10–16 Pa.

Table 2.1: Discharge and plasma parameters

Parameters	Values
Floating Potential (V_f)	250-320 V
Plasma Potential (V_p)	270-340 V
Plasma Density (n_i)	$1-5 \times 10^{15} m^{-3}$
Electron Temperature (T_e)	2-4 eV
Ion Temperature (T_i)	0.03 eV

2.6 Characterization of dusty plasma

We have already discussed the characterization of the plasma using a single Langmuir probe and an emissive probe in detail in last section. This section aims to provide a brief description of the characterization of dusty plasma. The dust particles in the plasma environment become negatively charged due to the higher mobility of electrons than ions. These negatively charged dust particles exert the sheath electric field force in a vertically upward direction due to sheath electric field $E(y)$, which is directed in the downward direction (negative y-direction) whereas

the gravity pulls the particle in a downward direction. Whenever these two forces balance each other, the particles simply levitate in the plasma-sheath boundary depending upon the size of the particles and the magnitude of the sheath electric field. The force balance equation can be given by:

$$m_d g = Q_d(y) E(y). \quad (2.6)$$

Where m_d , g and $Q_d(y)$ are the mass of the particles, acceleration due to gravity and the charged accumulated on the dust surface at a particular location. In our experiments, the dust particles are introduced in the plasma either by a dust dispenser or sprinkled on the cathode before performing the experiments as described in Subsec. 2.1.7). As soon as the plasma is initiated, the dust particles that are sprinkled on the cathode tray or introduced by dust dispenser get negatively charged and levitate at a height of $\sim 1.3 - 1.7$ cm from the cathode by a balance of the sheath electrostatic force and gravitational force in the vertical direction. The repulsive interactions among the negatively charged dust particles in the radial direction can be nullified by the strong radial confinement force provided by the cathode edges. However, the repulsive interaction in the axial direction is taken care of by the grounded copper wire and the right strip. The force balance in axial, radial and vertical directions creates an equilibrium dust cloud. Depending upon the mass (m_d) and charge (Q_d) of the particles and the vertical cathode sheath electric field ($E(y)$), the micron-sized polydispersive particles levitate at different heights by balancing the gravitational force (acting in the downward direction) and the electrostatic force (acting in the upward direction for the negatively charged dusty particles). Since $m_d \propto r_d^3$ and $Q_d \propto r_d$ (provided T_e remains constant), one can conclude from the force balance condition that the particles of the same size

should levitate at the same height, y , provided the electric field remains the same over the axial extent at that height.

A green light source is used to illuminate these levitated dust particles in the sheath region whereas a couple of cameras are utilized to capture the images of dust particles (see in Subsec. 2.3 for more details). The perfectly aligned parallel thin laser sheet (in x-z plane) always illuminates the dust particles of the same size for a given discharge condition. It is also worth mentioning that the laser light is kept perfectly parallel to the cathode so that the light scattered from dust particles is not re-scattered from the other plane of the dust cloud. The dynamics of the dust particles are captured by a fast CCD camera having a frame rate of 100-200 frames/s with a spatial resolution of 40-50 $\mu\text{m}/\text{pixel}$ (depending upon the experimental condition). We have taken care that the camera is not being saturated while capturing the images of the equilibrium dust cloud and the excitations of linear and non-linear waves. We have also verified that the image intensity is linear with dust number density by checking that the camera has a linear response with no offset.

A typical image of levitated Kaolin dust particles is shown in Fig. 2.18. The arrows represent the direction of different forces. The upward arrow corresponds to the sheath electric field force (F_E) whereas the downward arrow represents the gravitational pull (F_g). The side arrows represent the confinement force that comes from the radial sheath electric field around the two edges of tray shaped grounded cathode. The particles get confined axially due to the axial sheath electric fields around the metal strips that are placed on the cathode. The radial and axial confinements of these micron-sized dust particles have already been discussed in detail in Subsec. 2.1.4. Before performing experiments, the dusty plasma is thoroughly

characterized by measuring some of its equilibrium parameters. For that purpose, a systematic experiment is carried out to characterize the dusty plasma for a range of discharge conditions.

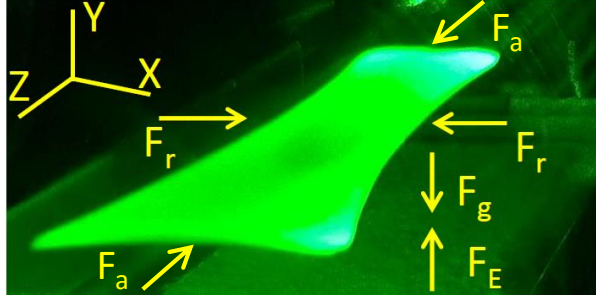


Figure 2.18: A photograph showing the levitation of dust particles in DPEX device.

Dusty plasma can be characterized by measuring/estimating the parameters such as particle size, mass, charge resides on the dust surface, inter-particle distance, dust number density, dust temperature, and coupling parameter. These equilibrium dusty plasma parameters are sometimes necessary to find out the other parameters like phase velocity of dust acoustic waves, dust plasma frequency, dust-neutral collision frequency, and mean free path, etc.. The detailed descriptions and the measurement procedures of these above dusty plasma parameters are given below in subsequent subsections.

2.6.1 Mass

To study the dynamics of dust particles in a flowing dusty plasma (described in Chap. 3) and to measure the potential profiles in a plasma (described in Chap. 4) by using dust particles as microprobes, mono-dispersive Melamine Formaldehyde (MF) particles having diameters $10.66 \mu\text{m}$, $8.90 \mu\text{m}$ and $4.38 \mu\text{m}$ are used. The mass density(ρ) of these MF particles is 1.51 g/cm^3 . For conducting experiments on the excitation of nonlinear waves and structures in a flowing dusty plasma

such as excitations of precursor solitons (described in Chap. 5), pinned structures (described in Chap. 6) and shock waves (described in Chap. 7), the poly-dispersive Kaolin particles of diameter ranging from 4 to 10 μm are used. The mass density of these particles is 2.65 g/cm^3 . Both these particles (MF and Kaolin) are assumed to be spherical and the following expression is used to calculate the mass of dust particles.

$$m_d = \rho \times \frac{4}{3}\pi r_d^3 \quad (2.7)$$

where m_d , ρ , r_d are the mass, mass density, and radius of the dust particles, respectively. For MF particles of diameters 10.66 μm , 8.90 μm and 4.38 μm the masses come out to be $9.57 \times 10^{-13} \text{ kg}$, $5.57 \times 10^{-13} \text{ kg}$, and $6.64 \times 10^{-14} \text{ kg}$, respectively, whereas for Kaolin particles of diameter 4-10 μm the mass comes out to be in the range $8.9 \times 10^{-14} \text{ kg} - 1.4 \times 10^{-13} \text{ kg}$.

2.6.2 Charge

The amount of charge that resides on the surface of the dust particle is an important parameter as it governs most of the dynamics of dust particles in a dusty plasma. The dust particles become charged whenever they are introduced in the plasma. The different charging processes that are associated with dusty plasmas are the collection of plasma species, secondary electron emission, thermionic emission, etc.. However, the magnitude of dust charge solely depends on the background plasma parameters and the size of the dust particles. In laboratory dusty plasma, the particles become negatively charged mostly by collecting more electrons than ions. Different theoretical models are available to estimate the dust charge [54, 55, 122], however, the measurement of dust charge is not explored much. In all these models, the charge acquired by the dust particles is estimated by assuming the dust

particles are of spherical capacitors. The following relation is used to estimate the charge as [123]:

$$Q_d = CU = 4\pi\epsilon_0 r_d U, \quad (2.8)$$

where C is the capacitance, U is the surface potential of the dust particle with respect to the plasma potential. ϵ_0 , r_d are the permittivity of free space and radius of the dust particles, respectively. Dust surface potential is estimated in the past either by taking into account the Orbital Motion limited (OML) approximation [122] or by Collision Enhanced Plasma Collection (CEC) [54, 55] approximation. Both these theories are based on the assumption that the collections of ions and

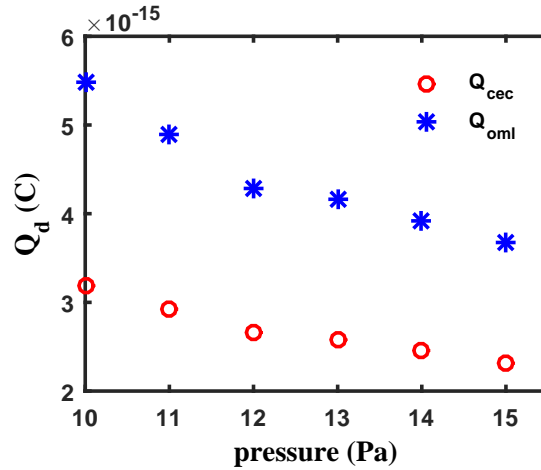


Figure 2.19: Variation of dust charge calculated using OML and CEC theories with pressure.

electrons fluxes are orbitally limited for an isolated spherical particle. OML theory assumes that the electrons and ions come to the dust particle without colliding with the neutrals which essentially means that the electron-neutral and ion-neutral collision mean free paths ($\lambda_{en,in}$) should be greater than the plasma screening length (λ_D). However, earlier experiments suggests that even in weak collisional limit ($\lambda_{en,in} \gg \lambda_D$) OML theory overestimate the dust charge [124]. Later, Khrapak *et al.*

has corrected the OML theory and provided Collision Enhanced Plasma Collection (CEC) model in which frequent collisions of ions with neutrals in the expression of total current drawn by the dust is considered [54]. This theory validates the experimental results in low as well as in high-pressure regimes ranging from 10–50 Pa [124]. Our experiments are carried out in the range of neutral pressure $p=10-12$ Pa, therefore the CEC model to estimate the dust surface potential is justified. We have numerically solved the net current on the dust surface described in Ref. [124, 125] using the Newton Raphson technique and estimate the dust surface potential with the help of OML and CEC models. The dust charge is then calculated using the capacitor model as given in Eq. 2.8. The variation of dust charge over a range of experimental pressures is plotted in Fig. 2.19 for the dust particle having a diameter of $10.66 \mu\text{m}$. One can see from Fig. 2.19 that the dust charge in both the theories falls monotonically with the increase of background pressure. Besides, the OML theory always overestimates the dust charge in comparison to the CEC model. The collisions of dust particles with plasma species suppress at lower pressure. Hence for a plasma with constant temperature and density, one can expect that the difference of estimated values of the dust charges decreases with the decreases in the background pressure. However, in our experiments, the OML and the CEC models show a larger deviation at a lower pressure as compared to a higher pressure. It is because the plasma parameters in our experiments vary with a decrease in pressure. With an increase in pressure, a fall in electron temperature and a rise in plasma density is observed (see Fig. 2.10).

2.6.3 Inter-particle distance and dust density

The dust density (n_d), is defined as the number of dust particles per unit volume, is estimated by finding out the inter-particle spacing (d). A single dust particle is assumed to contain in the sphere of radius d and hence the dust density can be expressed as:

$$n_d = \frac{3}{4\pi d^3} \quad (2.9)$$

Since our experiments are mostly conducted in a dense dust cloud, therefore it is very difficult to measure the inter-particle distance. However, to measure the dust density, the tail part of the dust cloud is captured by a CCD camera in full resolution such that the individual dust particles can be identified. From the information of the inter-particle distance, one can be calculated the dust density using Eq. 2.9. For a range of inter-particle distance of 360–170 μm , the dust density varies from $0.5 \times 10^{10} / \text{m}^3$ to $5 \times 10^{10} / \text{m}^3$ in our experiments.

2.6.4 Temperature

The dust temperature (T_d) is estimated by tracking the individual particles at the tail part of the dust cloud for 500 consecutive frames. From the information of the coordinates of the dust particles over time, the velocity distribution function is calculated. The experimental data points are then fitted by a Maxwellian function and the full width at half maximum of the distribution function gives the temperature of the dust particles. In the range of our discharge conditions, the dust temperature varies in the range 0.5–1 eV.

2.6.5 Coulomb coupling parameter

Due to the low charge to mass ratio, dusty plasma exhibits different states of matter e.g. crystalline state, liquid state and gasses state in contrast to the conventional plasma. The state of the dusty plasma can be defined by a quantity called the Coulomb coupling parameter, Γ . It is the ratio of potential energy to the dust thermal energy, which is already described in Chap. 1 at Sec. 1.2.6. In the DPEx device, the dust particles form a strongly coupled dusty plasma in which the Coulomb coupling parameter varies over the range 80-220 [116]. However, in the case of flowing dusty plasma experiments, the dust cloud behaves as a fluid whose Γ varies from 10–30.

The following table (Tab. 2.2) provides the range of dusty plasma parameters for the range of discharge voltages (V) = 290–370 V, discharge currents (I_d) = 2–11 mA and working pressures (p) = 10–16 Pa.

Table 2.2: Dusty plasma parameters

Parameters	Values
Dust mass (m_d)	$9-14 \times 10^{-14}$ kg
Dust charge (Q_d)	$1-4 \times 10^{-15}$ C
Inter-Particle distance (r_d)	360-170 μm
Dust number density (n_d)	$0.5-5 \times 10^{10}$ m^{-3}
Dust Temperature (T_d)	0.5-1 eV

2.7 Flow generation

As this thesis work mainly focuses on the excitation of nonlinear waves and structures in a flowing plasma, hence it is important to discuss some of the techniques that we have developed to generate the flow in a dusty plasma medium. The flows on the dust particles are generated using three different techniques, namely Single

Gas Injection (SGI) technique, Dual Gas Injection (DGI) and altering potential hill technique. These three techniques to generate the flow in a dusty plasma medium are described in the following subsections.

2.7.1 Single Gas Injection (SGI) technique

In the case of the Single Gas Injection technique, the equilibrium dust cloud is formed at a particular discharge condition by adjusting the pumping rate and the gas feeding rate. In this situation, the particles only show their random motion. To generate the flow in the dust fluid, the gas feeding rate is decreased suddenly at port P1 which creates a pressure difference in the glass chamber. Near the port P1, the gas pressure becomes lower compare to the location where the dust particles levitate. To maintain the dynamic equilibrium the neutrals particles rush towards the pump and during their movement, they carry the dust particles on their way. As a result, the dust particles are seen to move always from right to left. The dust particle velocity can be tuned precisely by adjusting the change of gas flow rate at port P1 and the background pressure. This SGI technique is used extensively to generate the flow in the dust component to study the dynamics of dust particles (presented in Chap. 3), to measure the potential profile by using dust particles as micro-probes (presented in Chap. 4), to excite the shock waves in an inhomogeneous dusty plasma (presented in Chap. 7).

2.7.2 Dual Gas Injection (DGI) technique

Dual Gas Injection (DGI) technique is also a method to generate the flow in the micron-sized dust particles. As the name suggests, in this method the gas is inserted from two sides of the Dusty Plasma Experimental (DPEX) device. Two

ports P1 and P2 are used for feeding the gas in this method. Initially, the dynamic equilibrium of dust particles is attained by feeding the gas from both the ports such that the working pressure remains constant. The dust particles are then injected from port P4 in the plasma using a dust dispenser. Due to the dynamic equilibrium, the dust particles always move from right to left. In this technique, the neutrals carry the dust particles on their way to the pump similar to the SGI technique however the dynamics of the dust particles are slightly different in this case of flow generation. The details of this technique will be discussed in Chap. 3.

2.7.3 Altering potential hill technique

In this case of flow generation, a copper wire of 1 mm diameter and 6 cm length is installed radially on the grounded cathode. This wire can be kept either grounded or in floating potential. There is also a provision to keep this wire in an intermediate potential by connecting a variable resistance in series with the wire and the ground through a mechanical switch. The details about this wire and its circuitry are discussed in Subsec. 2.1.4. As discussed earlier, the dust particles are initially confined in between the right confinement strip and this grounded wire and exhibit only the thermal motion. When the wire is kept at grounded potential, the plasma creates a sheath around it. The sheath provides a negative potential with respect to the dust surface potential and hence the negatively charged dust particles get confined in between the wire and the right strip. At that time, the dust particles only exhibit the thermal motion.

Fig. 2.20(a) shows a cartoon of the y - z plane of dust cloud when the particles get confined in between the wire and the right strip. The yellow circle in the figure represents the location of the wire and the solid line around the yellow

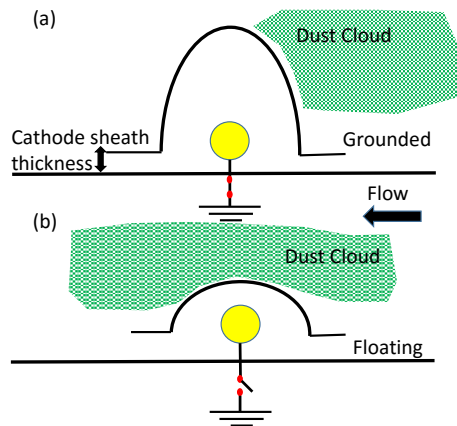


Figure 2.20: Schematic diagram to show the generation of flow by altering the potential hill technique. a) The confinement of dust particles by a grounded wire and b) the flow of particles over the floating wire.

circle qualitatively represents the sheath profile around the wire. When the wire is switched suddenly to the floating potential, the charged dust particles and the floating wire come almost in the same potential (see Fig. 2.20(b)) as a result, the particles start to flow from right to left over the wire. This technique of flow generation is mainly employed to excited the precursor and the pinned solitons, which will be discussed in more detail in Chap. 5 and Chap. 6. The velocity in

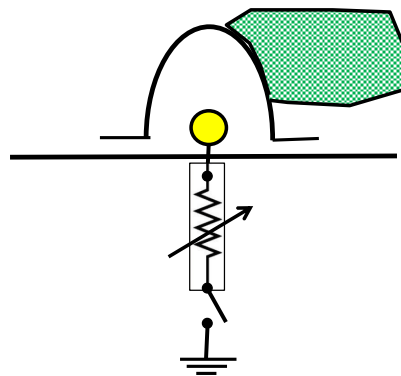


Figure 2.21: Modulating the height and the width of the hill by attaching resistances in between the wire and the ground.

the dust fluid can be precisely adjusted by tuning the height of the potential hill

caused by the wire. It can be achieved by drawing the current through different resistances connected with the wire as shown in Fig. 2.21. The potential profiles around the wire over a range of discharge condition are measured using dust as a dynamical probe and described in more detail in Chap. 4.

2.8 Measurements of flow velocities

After the initiation of flow in dust fluid, it is equally important to measure the velocity of the individual particles as well as the dust fluid for performing further experiments. These measurements indirectly give the information of the force that acts on the dust particles in a flowing dusty plasma. Besides that, the magnitude of flow velocity (subsonic/sonic/supersonic) by which it flows also plays an important role to determine the type of collective excitations in a flowing dusty plasma. Thus, in the following subsections section, we will discuss some of the measurement techniques to estimate the flow velocity of individual particles and the velocity of the dust fluid.

2.8.1 Particle Image Velocimetry (PIV)

Particle Image Velocimetry (PIV) technique is used to measure the dust flow velocity when the dust density is reasonably high. It is a MATLAB based open source code [119] and generally used to estimate the properties of a flowing fluid. For the present set of analyses, 20-30 consecutive images of pixel resolution 1000×200 are taken in the interval of 7 ms. The algorithm divides the images in $32 \text{ pixel} \times 32 \text{ pixel}$ interrogation area in which $16 \text{ pixel} \times 16 \text{ pixel}$ interrogation area is accommodated in steps of $8 \text{ pixel} \times 8 \text{ pixel}$ area to construct the velocity vectors. The

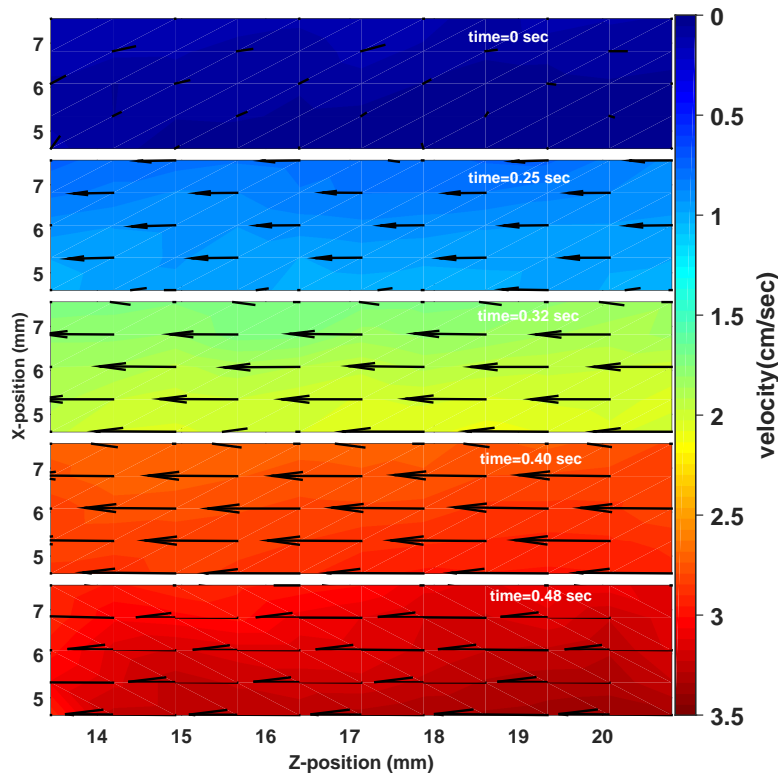


Figure 2.22: The magnitude and velocity vector of dust fluid analyzed using PIV technique.

mean velocity vectors are then formed by averaging the velocities obtained from all the frames. The typical velocity vector of the x-z plane of a dust cloud is shown in Fig. 2.22, when the flow is generated using the SGI technique. Different subplots of Fig. 2.22 show the velocity vectors at a different instant after the generation of flow. The color code represents the magnitude of the velocity where the blue color represents the minimum velocity and the red (see Fig. 2.22) color represents the maximum velocity. The direction of straight arrows essentially indicates that the dust particles move unidirectional from right to left almost with a constant velocity (as the velocity vectors are of the same length) at a given time. In these experiments, the velocity of the dust fluid varies from 0–4 cm/s over time. This method of measuring the flow velocity is used in Chap. 5, Chap. 6 and Chap. 7.

2.8.2 super Particle Identification Tracking (sPIT)

An IDL based super Particle Identification Tracking (sPIT) code is also used to measure the velocity of the dust particles [118]. This code works efficiently when the density of dust is very low such that the particles can be identified individually. In this thesis work, sPIT code is mainly used when the flow is generated either by SGI or DGI techniques as discussed in the Subsec. 2.7.1 and 2.7.2. With the help of this code, the particle positions are identified in several consecutive frames by plotting the brightness contour and finding the centres of the intensity of each local region. The velocity of the particles is then calculated from their instantaneous

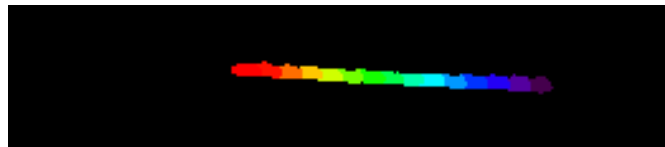


Figure 2.23: Color plot showing the trajectory of particles when analyzed using spit code.

positions over time. The inverse of the frame rate gives the time between two consecutive frames. The trajectory of a single dust particle obtained from sPIT code is plotted in Fig. 2.23. In this case, the flow is generated using the SGI technique. The color plot shows the time information of the particle- violet color represents the particle position at the initial time whereas red color represents the final position of the particle. The color sequence suggests that the particle moves from right to left almost in a straight line. The size of the same color band of each color signifies that initially, the particle moves with a slower velocity and then it accelerates. The trajectories of the particles and their associated dynamics extracted from this code are described in more detail in Chap. 3 and Chap. 4.

2.9 Conclusions

To conclude, a tabletop versatile Dusty plasma Experimental device is built at IPR to perform experiments on the excitations of nonlinear waves and structures in a flowing dusty plasma. It is an inverted Π -shaped glass chamber having several axial and radial ports for different purposes like pumping, gas feeding, taking out electrical connections, dispensing dust, diagnosing the plasma and dusty plasma, etc.. A rotary pump is used to evacuate the chamber at a base pressure of 0.1 Pa. A circular live anode and a grounded tray-shaped cathode are used to initiate a DC glow discharge plasma in the background of Ar gas at a working pressure over the range of 10-15 Pa. A single Langmuir probe and an emissive probe are used to characterize the plasma over a range of discharge conditions by measuring plasma density, floating and plasma potentials, electron temperature and electron energy distribution function. The radial profile of plasma potentials is obtained to estimate the radial sheath electric field which is responsible for the levitation of dust particles.

Dusty plasma is then produced either by introducing mono-dispersive Melamine Formaldehyde or poly-dispersive Kaolin particles in the plasma. A combination of camera and laser are used for optical diagnostics to capture the dynamics of dust particles. The consecutive images recorded by the camera are stored in a computer for further analysis. From the stored images, the dusty plasma is characterized thoroughly over a range of discharge conditions by measuring/estimating inter-particle distance, particle density, dust temperature, dust charge, Coulomb coupling parameter, etc..

The various techniques namely Single Gas Injection (SGI), Duel Gas Injec-

tion (DGI), altering potential techniques are used to generate a flow in the dust component. Different analysis techniques such as MATLAB based Particle Image Velocimetry (PIV) toolbox is used to estimate the flow velocity of a dust fluid whereas an IDL based super Particle Identification Tracking (sPIT) code is used to calculate the velocity of individual particles when the particles can be resolved as a single particle.

3

Dynamics of dust particles in a flowing dusty plasma

Part of this chapter is published in *Phys. Plasmas*, **26**, 023701 (2019) by Garima Arora *et al.*.

3.1 Introduction

The study of flowing dusty plasmas has attracted recent attention and flow induced excitations in dusty plasmas have become an emerging area of research in laboratory as well as in the astrophysical context. When the dust fluid flows past an obstacle it can excite a wide variety of linear and non-linear waves such as wakes and precursor solitons [47, 48, 114], bow shocks [81, 126], dispersive shocks [83] and Von Kármán vortex streets [127]. In all these experimental studies, the flow in the

dust fluid was typically initiated either by varying the confining potential [48, 126] or by sudden changes in the gas flow into the chamber [83] or by mechanically tilting of one side of the experimental chamber [81]. The focus of these experiments so far have mainly been on the collective excitations in the dusty plasma medium in which the dynamics of the dust flow itself has not received much attention.

A number of past studies have investigated the effect of various forces like the radiation force [128, 129], the ion [58–60] and the neutral drag forces [130–133] and the thermophoretic force [134] on dust dynamics and have explored means of manoeuvring the dust dynamics through these forces. The ion and the neutral drag forces, in particular, can play a dominant role in either inducing or limiting the steady state flow velocities of dust particles as they stream in a background of ions and neutrals. A detailed study of the ion drag force are carried out in past by Yaroshenko *et al.* [133] on the PK4 device over a range of discharge parameters and using particles of different sizes. The work presented in this chapter deals on the systematic measurement of flow velocity of micro particles to study the dynamics of dust particles in a flowing dusty plasma in DPEX device. A primary motivation for this work is to provide a better understanding of the role of neutrals in the dynamics of gas flow induced dusty plasma flows that were used in past experiments on the DPEX device [48, 83, 135, 136].

The chapter is organized as follows: In the next section in Sec. 3.2, a brief description of the experimental setup along with the production of plasma and dusty plasma is presented. The generation of flow in dust particles and their velocity measurement are discussed in Sec. 3.3. The experimental results and discussion, force estimation and a theoretical model to describe the dust particle motion are discussed in Sec. 3.4, Sec. 3.5 and Sec. 3.6, respectively. Some final

concluding remarks are made in Sec. 3.7.

3.2 Experimental Set-up and procedure

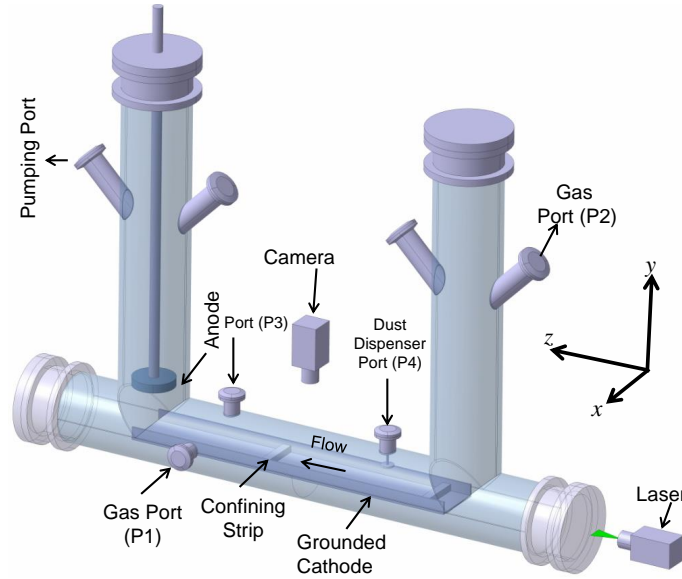


Figure 3.1: A schematic of the experimental set up for performing flowing dusty plasma experiments.

The experiments are carried out in the II shaped Dusty Plasma Experimental (DPEx) device. The system geometry of this device and the associated diagnostics have been given in details in Chap. 2. The vacuum chamber, as shown in Fig. 3.1, is evacuated to a base pressure of 0.1 Pa with the help of a rotary pump. Argon gas is then introduced by a mass flow controller and/or by a gas dosing valve using either port-P1 and/or port-P2 depending on the experimental requirements to set the working pressure at 9 – 15 Pa. A Direct Current (DC) voltage (300 – 400 V) is applied between the anode and the grounded cathode to produce plasma from the ambient Argon gas. The discharge current over the range of discharge conditions varies from 2 – 5 mA. The plasma parameters such as the ion density (n_i) \sim 1 – 3

$\times 10^{15}/m^3$, the electron temperature (T_e) $\sim 5 - 2$ eV are measured using a single Langmuir probe and an emissive probe. More details about the complete evolution of the plasma parameters over a broad range of discharge conditions can be found in Ref. [115] and Chap. 2 2.5.

Melamine Formaldehyde (MF) mono-dispersive spherical particles of diameter $10.66 \mu\text{m}$ (or 8.90 or $4.38 \mu\text{m}$) are then introduced into the plasma by a dispenser to create a dusty plasma. These micro-particles collect more electrons than ions from the plasma due to the higher mobility of electrons and get negatively charged and levitate near the cathode sheath region due to a balance between the electrostatic force (acting in the upward direction) and the gravitational force (acting in the downward direction). To observe the dynamics of these dust particles, they are illuminated by a green laser light (in the $x - z$ plane). The Mie-scattered light from the dust particles are captured by a CCD camera and the images from the camera are stored into a computer for further analysis.

3.3 Flow generation and velocity measurements

For conducting flowing dusty plasma experiments, these MF particles are made to flow along the axis of the Π -tube using two different methods e.g., Single Gas Injection (SGI) and Dual Gas Injection (DGI) techniques as discussed in details in [137] and in Chap. 2.7.1 and 2.7.2. In the SGI technique, a steady state dust cloud is initially formed in between the two axial confining strips by precisely balancing the pumping rate and the gas flow rate. This equilibrium of dust particles is then disturbed momentarily either by increasing the pumping rate or by reducing the gas flow using a mass flow controller (controlled by a software through a computer) attached to port P1. In both the cases the particles are seen to move from the

right to the left along the axis of the chamber. For our present set of experiments, the flow in dust particles is always initiated by reducing the gas flow in steps of ~ 0.5 *sccm*. In the DGI method of flow generation an equilibrium working pressure is maintained by introducing Argon gas using both the gas ports P1 and P2 as shown in Fig. 3.1. The dust particles are then injected into the plasma with the help of a dust dispenser and they get charged during the time of their fall. These particles come to the sheath region and are seen to flow from right to left due to the continuous flow of neutral gas. It is worth mentioning that for carrying out all these experiments the pressure range as well as the flow rate differences are set in such a way that the flow of dust particles is always laminar in nature. The dynamics of dust particles for these two different flow generation techniques will be discussed in subsequent sections.

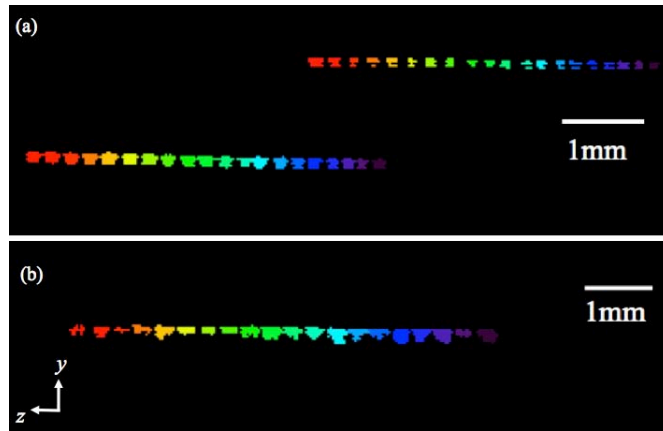


Figure 3.2: Color plot showing the trajectories of two particles where the flow is generated using (a) Single Gas Injection Technique (SGI) (b) Dual Gas Injection Technique (DGI).

Fig. 3.2(a) shows the trajectories of two dust particles of diameter $10.66 \mu\text{m}$ at a given pressure of 12 Pa and a discharge voltage of 320 V when the flow is generated using the SGI technique. Different colors represent the particle positions at different times in intervals of 6.25 ms. Violet color corresponds to initial position

of the particle whereas the red color corresponds to final position of the particle. The figure shows that the particle moves from right to left along the axial direction (along z) almost with a constant velocity. Fig. 3.2(b) shows the same when the flow is initiated using the DGI technique. It is to be noted that the trajectories show the same characteristics when the particles attain a constant velocity in both the techniques.

To study the dynamics of these dust particles, it is very important to measure the axial and radial components of the velocity. It essentially helps us to understand the fundamental forces that act on them. For analysing the video images of the flow of these dust particles an Idl based super Particle Identification Tracking (sPIT) code [118, 138] is used in which hundreds of still frames are considered over a wide range of discharge conditions. This code is very powerful and efficient to track individual particles and to measure the velocity very precisely when the particles are well resolved during the span of their journey.

3.4 Results and discussion

A series of experiments is carried out to study the dynamics of dust particles by varying different parameters namely gas flow rate, background pressure, size of dust particles and gas species. Their dependency are discussed in subsequent sections.

3.4.1 Influence of gas flow rate

To begin with, a series of experiments are carried out to study the dynamics of the dust particles by changing the gas flow rate and the background pressure. Fig. 3.3

shows the time evolution of a dust particle having diameter $10.66 \mu\text{m}$ when the experiments are performed at a discharge voltage of 300 V and pressure of 12 Pa and in which the flow is initiated by the SGI technique [137] with a flow rate difference of 3.4 *sccm*.

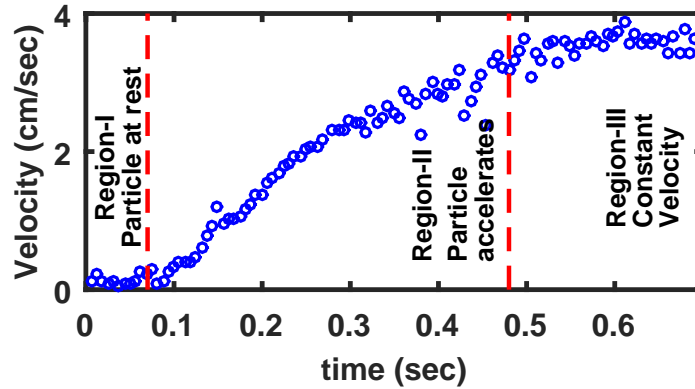


Figure 3.3: Time evolution of $10.66 \mu\text{m}$ particle at a fixed pressure of $p=12 \text{ Pa}$ and discharge voltage of 300 V when the flow is generated by Single Gas Injection Technique (SGI).

To understand the dynamics of dust particle in a better way, Fig. 3.3 is divided into three different distinct regions. In region-I (region of zero velocity), the dust particles only exhibit random motion (no directional motion) and represent the phase when no flow in the dust particles has yet been initiated. Region-II is the accelerating region, where the dust particles start their journey from rest in the z -direction and accelerate for approximately 0.45 s. This happens when the gas flow rate near the port P1 is suddenly reduced and as a result the neutrals move from right to left for neutralizing the imbalance of sudden gas pressure. On their way towards the pump, the neutral molecules impart their momentum to the heavier dust particles causing them to move in the direction of the neutrals. The transfer of momentum from neutrals to dust particles continues till the velocity of the dust particles become equal to the velocity of the neutrals and correspond

to the accelerating phase marked as Region-II in Fig. 3.3. When the velocity of the dust particle becomes equal to the velocity of neutrals, it moves with almost constant velocity - an asymptotic velocity as depicted in region-III. In this region of Fig. 3.3, it is clearly seen that the particle moves with a constant velocity of ~ 4 cm/s during $0.6 - 0.7$ s. It is worth mentioning that the moving neutrals impart their momentum to dust particle whenever the velocity of the dust particle decreases due to other damping phenomena.

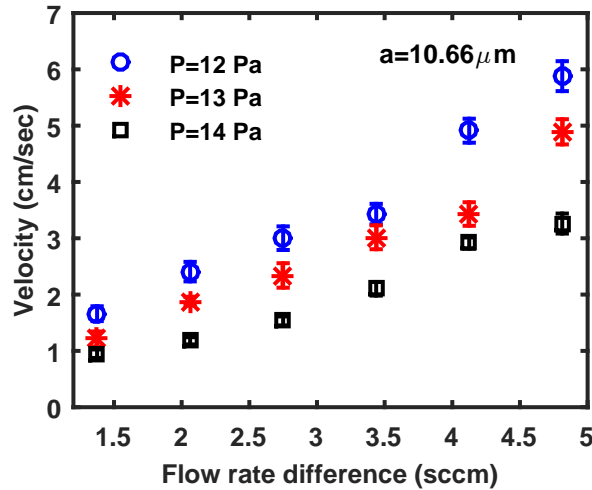


Figure 3.4: Variation of asymptotic velocity of $10.66 \mu\text{m}$ particle with flow rate difference for three different gas pressures.

Fig. 3.4 shows the variation of this asymptotic velocity achieved by $10.66 \mu\text{m}$ particle when the differential gas flow rate is varied by different amounts and for three different background pressures. The average asymptotic velocities are calculated from the time evolution of different particles with the same size at the time when they attain a constant velocity as discussed in Fig. 3.3. The figure indicates that the asymptotic velocity increases monotonically with the gas flow rate difference. A higher flow rate difference concomitant larger transfer of momentum to the dust particles which then moves with a greater velocity for a given pressure.

3.4.2 Influence of background pressure

Fig. 3.4 also shows that the asymptotic velocity decreases with an increase of the background gas pressure for a constant flow rate difference. This can be understood from the fact that the number of neutral gas molecules increases with the increase of Argon gas pressure and as a result the neutrals undergo frequent collisions among themselves which essentially reduces the effective directional velocity of the neutrals. As a consequence they impart less directional momentum to the dust particles causing them to move with a smaller velocity.

3.4.3 Influence of size of dust particle

To study the effect of particle sizes on the flow velocity, a set of experiments is carried out with different sized dust particles. Fig. 3.5(a) shows the velocity evolution of dust particles having diameter $10.66 \mu\text{m}$, $8.90 \mu\text{m}$ and $4.38 \mu\text{m}$ for the case of gas flow rate difference of $\sim 2.1 \text{ sccm}$ at a constant pressure of 11 Pa and discharge voltage of 300 V. Fig. 3.5(a) shows that the asymptotic velocity attained by all these micron sized particles are nearly equal indicating that the Region-III as shown in Fig. 3.3 is independent of the sizes and hence masses of these dust particles. However, the acceleration region (Region-II) shows a marked dependency on the size of the dust particle. The velocity profiles show that the lighter dust particle initially moves with a higher velocity than the heavier one whereas after $\sim 0.4 \text{ s}$, the lighter particle achieves the same constant velocity as attained by the bigger particle. In the accelerating region in which the dust particle gains momentum from the moving neutrals, the acceleration is higher for the lighter dust particle whereas it is smaller for the heavier particle as shown in

Fig. 3.5(a). It is to be noted that the smaller particle overshoots in the downward direction from the equilibrium velocity, in which other force may play a role other than neutral streaming which will be discussed later in detail in Sec. 3.6.

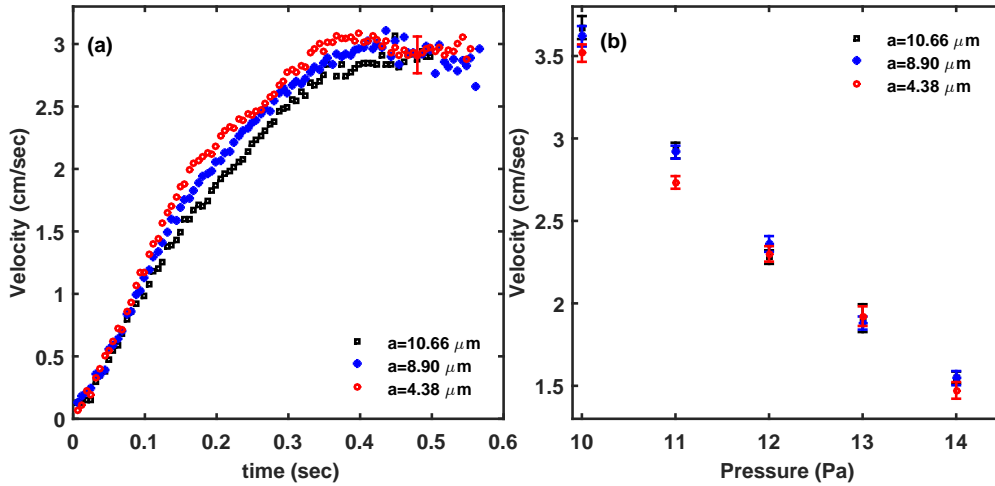


Figure 3.5: Variation of constant velocity with pressure for three different micro particles of diameter $10.66 \mu\text{m}$, $8.90 \mu\text{m}$ and $4.38 \mu\text{m}$ when the flow is generated by SGI technique

Finally, the asymptotic velocities for these three different sized particles are measured over a range of pressures from 10 Pa to 14 Pa by keeping the other discharge parameters constant at a flow rate difference of $\sim 2.1 \text{ sccm}$. Fig. 3.5(b) shows the variation of the asymptotic velocities of these three different sized particles with pressure. It is clearly seen that all the particles attain the same velocity for the entire pressure range and this velocity decreases with an increase in the background pressure. The error bars shown in the figure are calculated by performing the experiments several times and taking the mean as well as standard deviation of velocities. However, at lower pressures ($p = 10 \text{ Pa}$ and 11 Pa) the constant velocity of smaller particle of diameter $4.38 \mu\text{m}$ is slightly smaller compare to the bigger particles of diameter $8.90 \mu\text{m}$ and $10.66 \mu\text{m}$ whereas for higher

pressures, it is almost same for all particles. This may be due to the fact that the other forces than neutral streaming may contribute to determine the asymptotic velocity of smaller particles at lower pressure which will be examined later in Sec. 3.6.

To examine the dynamics of dust particles in a steady state equilibrium, another set of experiments is carried out by introducing Argon gas through the gas port P₂ with the help of Dual Gas Injection technique as described in Sec. 3.3 and in Ref. [137]. It should be mentioned that, in this technique of flow generation it is difficult to identify Region-I (region of zero velocity) and Region-II (region of acceleration) of the particle trajectory as identified in Fig. 3.3 for the SGI technique as the particles attain their asymptotic velocity nearly from the very beginning of their journey. It is due to the fact that there is a continuous flow of neutrals from port P₂ towards the pump which always carry the dust particles as soon as they fall into the sheath region.

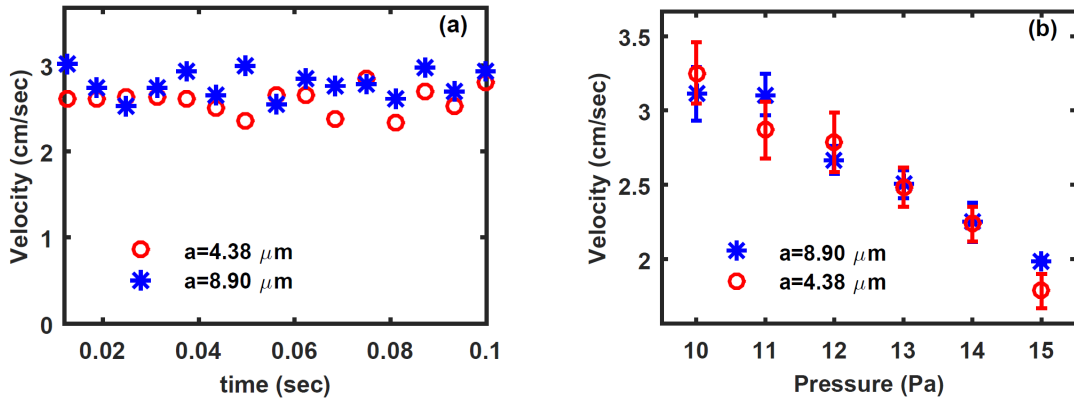


Figure 3.6: (a) Time evolution and (b) variation of constant velocity with pressure of 8.90 and 4.38 μm micro particle when flow is generated by Dual Gas Injection (DGI) technique.

Fig. 3.6(a) shows the time evolution of the velocity for two different dust particles of diameter 8.90 μm and 4.38 μm , respectively when the flow in the dust

particle is generated by the DGI technique at a discharge voltage of 300 V and pressure of $p = 13$ Pa. It is seen from the figure that irrespective of sizes, the particles move at constant velocities of nearly the same value. Fig. 3.6(b) shows that the asymptotic velocity decreases monotonically with increasing background pressure akin to the earlier case (see Fig. 3.5(b)) when the flow is generated using SGI technique. Interestingly, it is also seen that both the particles possess nearly the same velocity for the entire range of gas pressure. Therefore, the experimental results obtained in both the techniques demonstrate that the neutrals are primarily responsible for carrying the dust particles in their own direction of flow from the right to the left. A more quantitative confirmation of this observation will be established in Sec. 3.5 by making theoretical comparisons between all other forces acting on the dust particle and comparing them with the neutral streaming force.

3.4.4 Influence of neutral particles

For studying the role of different neutral species on the dynamics of dust particles, an experimental investigation is carried out using three different gases with different masses. The average asymptotic velocities are measured from the trajectories of the particles when they attained their constant velocities. In this set of experiments the flow rate difference and other discharge parameters are kept constant at 2.75 *sccm*, 300 – 500 V and 10 – 15 Pa, respectively. The variation of these asymptotic velocities for different gases are plotted in Fig. 3.7. The open-circle, square, and star represent the results of the dust particle velocities in backgrounds of Krypton ($m_n = 80 u$), Argon ($m_n = 40 u$), and Neon ($m_n = 20 u$) gases, respectively. It is observed that the asymptotic velocities again decrease with an increase of gas pressure for all the gases as seen before in Fig. 3.5(b) and Fig. 3.6(b). How-

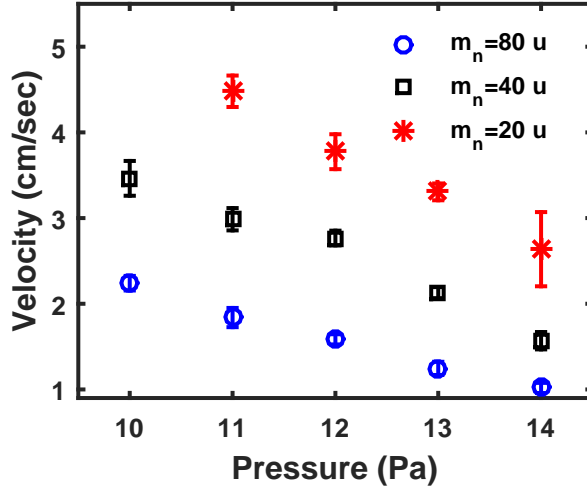


Figure 3.7: Variation of constant velocity with pressure for Krypton, Argon, Neon gases.

ever, for a given pressure the dust particles move with a slower asymptotic velocity (represented by open circles) in a background of heavier neutrals compared to a background of lighter gas molecules (represented by open stars). This can be understood from the fact that for a given flow rate difference the lighter neutrals move with a higher velocity due to their lower inertia compared to the heavier neutrals. Since the asymptotic velocity of the dust particle equals the flow velocity of the neutrals they move faster in a gas of lighter mass. As a result the dust particles move with maximum velocity in the case of Neon plasma, whereas they move with minimum velocity for Krypton plasma.

3.5 Estimation of various forces

For an estimate of the various forces (e.g. Coulomb force, ion drag force, neutral streaming force, electrostatic force *etc.*) acting on the particle, first the electric field ($E = -\frac{dV_p}{dZ}$) is estimated over a wide range of discharge parameters by measuring

the plasma potential (V_p) at different axial locations. For that estimation, the average plasma potentials (V_p) are measured (by floating point technique [117]) using a couple of emissive probes that are placed at two different axial locations at a distance of $dZ = 5$ cm. The working principle of an emissive probe and its circuitry is discussed in details in Chap. 2.2.2. The effective electric field is estimated from the difference of plasma potentials before and during the generation of flow in dust particles. It is found that during the flow generation the maximum electric field turns out to be in the range of $8 - 12$ V/m directed to dust flow for a flow rate difference of $1.5 - 5$ sccm, $V_d = 300$ V and $p = 10 - 15$ Pa.

3.5.1 Coulomb force:

To start with, the Coulomb force ($F_e = Q_d E$) acting on the dust particles is determined by multiplying the charge (Q_d) acquired by the dust particles with the local axial electric field as discussed before. The charge is calculated by assuming the dust particle to be a spherical capacitor and using the fundamental relation, $Q_d = CU$, where $C = 4\pi\epsilon_0 r_d$ and U are capacitance and surface potential of dust particle. The surface potential of dust particle is calculated using Collision Enhanced plasma Collection model (CEC) [124, 125] as discussed in Chap. 2.6.2 and Q_d comes out to be $\sim 2.87 \times 10^{-15}$ C for $r_d = 5.33$ μm particle. For our experimental parameters, $p = 12$ Pa, flow rate difference 3.5 sccm, $E = 10$ V/m and $T_e = 3.0$ eV which yields the value of Coulomb force, $F_e \sim 30$ fN, which is directed opposite to the dust flow and acting as a drag for these micro particles.

3.5.2 Ion drag force:

Micro-particles experiences ion drag force when ions transfer their momentum to the dust particles. For the ion drag force F_i , the expression given by Khrapak et al. [61] is used, which estimates F_i for a single micro-particle in a collisionless Maxwellian plasma for an arbitrary ion velocity as:

$$F_i = \sqrt{2\pi} r_d^2 n_i m_i v_{Ti}^2 \left\{ \sqrt{\frac{\pi}{2}} \operatorname{erf} \left(\frac{u_f}{\sqrt{2}} \right) \times \right. \\ \left. [1 + u_f + (1 - u_f^{-2})(1 + 2z\tau) + 4z^2\tau^2 u_f^{-2} \ln\Lambda] \right. \\ \left. + u_f^{-1} [1 + 2z\tau + u_f^2 - 4z^2\tau^2 \ln\Lambda] \exp \left(-\frac{u_f^2}{2} \right) \right\}. \quad (3.1)$$

Where, n_i , m_i , $v_{Ti} = \sqrt{8k_B T_i / m_i \pi}$ are the density, mass and thermal velocity of ions, respectively. The ion drift velocity normalized by the ion thermal velocity is denoted by u_f . The dimensionless charge of the micro particle is given by $z = Q_d |e| / (4\pi r_d k_B T_e)$, and the ratio of the electron to the ion temperature is denoted by $\tau = T_e / T_i$. The Coulomb logarithm is given by:

$$\ln\Lambda = \ln \left[\frac{\beta + 1}{\beta + (r_d / \lambda_{ef})} \right] \quad (3.2)$$

where β is defined as $\beta = Q_d |e| / [4\pi \epsilon_0 k_B T_i (1 + u_f^2) \lambda_{ef}]$ and $\lambda_{ef}(u_f)$ is the effective screening length and can be expressed as $\lambda_{ef}(u_f) = 1 / \sqrt{\lambda_i^{-2} (1 + u_f^2)^{-1} + \lambda_e^{-2}}$. The ion flow velocity is calculated by using the formula $v_i = \mu_i E$. E is the effective electric field when the flow in the dust particle is initiated and μ_i is the ion mobility, estimated by using the expression $\mu_i(E) = \mu_0 / p \sqrt{(1 + \alpha E / p)}$ with $\mu_0 = 19.5 \text{ m}^2 \text{ Pa V}^{-1} \text{ s}^{-1}$, $\alpha = 0.035 \text{ m Pa V}^{-1}$ for Argon gas of pressure p (in Pascal) [139]. For $E = 10 \text{ V/m}$, $p = 12 \text{ Pa}$, $n_i = 1.2 \times 10^{15} \text{ m}^{-3}$, the ion drag force

comes out to be $F_i \sim 9$ fN directed along the flow of dust particles.

3.5.3 Neutral streaming force:

The force on the dust due to streaming neutrals can be calculated by the Epstein formula [62], as expressed by

$$F_n = \frac{4}{3} \gamma_{Eps} \pi r_d^2 m_n n_n V_{Tn} (v_f - v_d), \quad (3.3)$$

where, m_n , n_n , V_{Tn} and v_f are the mass, number density, thermal and drift velocities of the neutrals, respectively. It is worth mentioning that the neutral streaming force acting on the dust particles is proportional to the relative velocity of neutral with respect to dust. It becomes maximum when the dust particles are at rest and minimum when they attain the velocity of neutrals. γ_{Eps} represents the Epstein drag coefficient which varies from 1 to 1.4 depending upon the types of reflection [62]. The Epstein coefficient as measured in our device is $\gamma_{Eps} \sim 1.2$ [115]. For a specific set of experiments, the neutral velocity comes out to be $v_f = 4$ cm/s at the flow rate difference of 3.50 *sccm* and background Argon gas pressure of $p = 12$ Pa. The particles of diameter 10.66 μm , $m_n = 6.67 \times 10^{-26}$ kg, $n_n \sim 3 \times 10^{21}$ m^{-3} and thermal velocity $V_{Tn} \sim 430$ m/s at a temperature of 300 K, the magnitude of maximum neutral streaming force comes out to be ~ 500 fN.

For the bigger particle of diameter 10.66 μm , the ratios $\frac{F_e}{F_n}$ comes out to be ~ 0.0625 whereas $\frac{F_i}{F_n}$ becomes ~ 0.018 . For smaller particles at low pressure, the electrostatic force plays an important role as $\frac{F_e}{F_n} \sim 0.167$ whereas the ratio $\frac{F_i}{F_n} \sim 0.033$ still remains insignificant. The above quantitative estimates show that the neutral streaming force and electrostatic forces are the predominant forces for

our experimental conditions and are primarily responsible for determining the dust dynamics.

3.6 Theoretical model

To interpret the experimental findings qualitatively, a simple theoretical model is developed in which the equation of motion for the dust particle can be written as:

$$m_d \frac{dv_d}{dt} = \gamma_{Eps} \frac{4}{3} \pi r_d^2 m_n n_n V_{Tn} (v_f - v_d) - Q_d E. \quad (3.4)$$

Where γ_{Eps} is the Epstein drag coefficients [65, 115] and m_d is the mass of MF dust particle. It is to be noted that only the contributions of neutral streaming force and electrostatic force are taken into account in the right hand side of Eq. 3.4 and ion drag force is neglected as discussed before in Sec. 3.5. Rewriting Eq. 3.4 in a compact form as

$$\frac{dv_d}{dt} + \frac{c}{m_d} v_d = \frac{c}{m_d} v_f - \frac{Q_d E}{m_d}, \quad (3.5)$$

where $c = \gamma_{Eps} \frac{4}{3} \pi r_d^2 m_n n_n V_{Tn}$.

After solving Eq. 3.5 we get:

$$v_d = (v_f - \frac{Q_d E}{c}) (1 - e^{-ct/m_d}). \quad (3.6)$$

The solution (Eq. 3.6) of equation of motion (Eq. 3.4) essentially describes the complete dynamics of the dust particle under the influence of the neutral streaming force and electrostatic force. From Eq. 3.6 it is seen that at $t = 0$ the particle starts from rest ($v_d = 0$) and asymptotes ($t \rightarrow \infty$) to $(v_f - Q_d E/c)$.

First, we have estimated the neutral flow velocity by solving the equation of

motion of neutrals for our experimental condition. The expression [140] for neutral velocity can be given by $v_f \sim \frac{(\nabla p)}{(m_n \nu_{nn} n_n)}$, where ∇p , m_n , n_n and are the gradient of pressure, mass of neutral argon atom, neutral density, and neutral-neutral collision frequency, respectively. Here $\nu_{nn}(= n_n \sigma V_{Tn}$, where σ is the neutral-neutral collision cross section) is the neutral-neutral collision frequency. During the initiation of flow, ∇P is measured by measuring the pressures at ports P3 and P4 which are separated by 30 cm (see Fig. 3.1) apart. For a specific experimental condition,

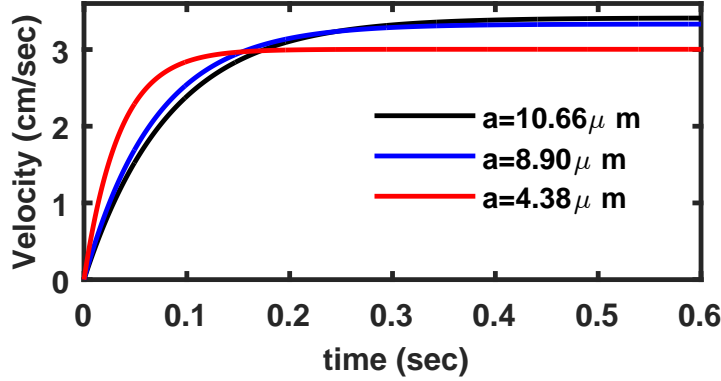


Figure 3.8: Theoretical plot of time evolution of 10.66, 8.90 and 4.38 μm particles.

$p = 11$ Pa, $V_d = 300\text{V}$ and gas flow rate of 2.1 sccm, the pressure difference at points P3 and P4 comes out to be 0.15 Pa which gives $\nabla p = 0.5$ Pa/m. In this experimental condition, the estimated neutral velocity comes out to be $v_f \sim 3.65$ cm/s for the values of $m_n = 6.67 \times 10^{-26}$ kg, $n_n \sim 2.75 \times 10^{21} \text{ m}^{-3}$, $V_{Tn} \sim 430 \text{ m/s}$ at a temperature of 300 K and $\sigma \sim 6.33 \times 10^{-20} \text{ m}^{-2}$. At that same experimental condition, the measured average asymptotic dust velocity is $v_d \sim 3$ cm/s. Thus, from the theoretically estimated value of neutral velocity and the measured value of the dust velocity, it can be seen that the dust particles attain slightly lower asymptotic velocity as the neutrals—a consequence of the direct influence of the neutral streaming force and electrostatic force on the dust.

This estimated flow velocity of neutrals $v_f \sim 3.65$ cm/s, charge Q_d from CEC model [124, 125] and measured electric field $E=11$ V/m for $p=11$ pa are used in the theoretical model (Eq. 3.6) to plot the time evolution of the velocities for three different sizes of dust particles in Fig. 3.8. It is to be noted that the smooth curves depicted in Fig. 3.8 are obtained from the analytic solution of Eq. 3.5 as given in Eq. 3.6 and provides a qualitative description of the time evolution of the dust particle of different sizes for understanding the experimental results shown in Fig. 3.5(a). One notes that in the initial stages, when the neutral streaming force dominates, the lighter particles accelerate rapidly leading to the separation of the three curves for small times in Fig. 3.6. Such a behavior is also clearly seen in the experimental results, where at early times the velocity of the $4.38 \mu\text{m}$ particle is observed to be higher than the heavier particles. As the particles gain energy and their velocities approach that of the neutral particles, the influence of the neutral streaming force begins to diminish and the electrostatic force begins to have a comparable influence. The electrostatic force has a stronger braking effect on the lighter particle leading to a smaller asymptotic value of the velocity for it. This is clearly seen in Fig. 3.8 for large times. At some time in between when the trajectories crossover, while approaching their asymptotic values, their velocities are very close to each other. Our end point experimental results, as shown in Fig. 3.5(a), correspond to such a stage and the fluctuations seen in the curves are a result of experimental measurement errors. These errors are estimated to be on the order of $\pm 2\% - 5\%$ of the average values. In the figure, we have not shown the error bars on the individual points to avoid cluttering up the plot—representative measure of the error has been shown in the left corner of the figure.

Interestingly, one can also estimate the dust charge from the measured asymp-

otic value of the dust velocity for a small sized particle. For a particle of diameter $2r_d$ $4.38 \mu\text{m}$ and at a low pressure of $p = 11 \text{ Pa}$, the dust charge is estimated from the expression $Q_d = \frac{(v_f - v_d)c}{E}$, where $c = \gamma_{Eps} \frac{4}{3} \pi r_d^2 m_n n_n V_{Tn}$. For $p = 11 \text{ Pa}$ and $E = 11 \text{ V/m}$, Q_d come out to be $\sim 7 \times 10^3 e$. As per the CEC model [124, 125], the charge residing on the surface of a dust particle of diameter $4.38 \mu\text{m}$ is about $Q_d \sim 8 \times 10^3 e$ which is in good agreement with our estimated value. However, this method to estimate the dust charge is only applicable for small sized particles and at low neutral pressures when the electrostatic force experienced by the particle is significant.

3.7 Conclusions

In conclusion, a set of experiments has been carried out to investigate the role of neutrals in initiating and sustaining the flow of dust particles in the Dusty Plasma Experimental (DPEX) device. The characteristics of the dust flow, initiated by two different techniques, namely the Single Gas Injection technique (SGI) and the Dual Gas Injection Technique (DGI), have been studied as a function of the neutral gas flow, the background pressure and the nature of the background gas. In the case of the SGI technique, the dust particles start from rest, go through an accelerating phase and then attain a steady state constant velocity. In the DGI method the acceleration phase is not discernible experimentally and the dust particles are carried along continuously by the flow of neutrals at a constant velocity. In this technique of flow generation the dynamical equilibrium is always maintained and hence it does not create any axial electric field. As a result the particles only flow from right to left due to neutral streaming force.

The asymptotic steady state velocity increases with an increase of the gas flow

rate and decreases with the increase of neutral background pressure when the gas flow rate is kept constant for both the techniques. The asymptotic velocity is independent of the size of dust particles whereas, for smaller particle of diameter $4.38 \mu\text{m}$ has slightly lower velocity at lower pressure. In the accelerating phase (for the SGI technique) the lighter dust particles show a higher acceleration compared to the heavier ones and then achieve slightly reduced asymptotic velocity. From experiments carried out with different background gases it is also found that the asymptotic velocity is dependent on the mass of the neutral molecules. The velocity is higher in the presence of a lighter gas compared to a heavier gas.

The experimental results can be well understood in terms of the neutral streaming force acting on the dust particles. A quantitative estimate of the various forces acting on the dust particles for our experimental conditions indicates that the neutral drag force predominates over all other forces and is the primary driver of the dust flow. A simple analytic solution of the equation of motion of the dust particle under the influence of the neutral streaming force reproduces the principal features of the experimental results.

4

Measurement of potential profiles around a charged object

Part of this chapter is published in *Phys. Plasmas*, **25**, 083711 (2018) by Garima Arora *et al.*.

4.1 Introduction

There has been a growing interest in flowing dusty plasma associated with the interaction of dust fluids with the charged object immeresed in the plasma. Notable examples are the experimental observation of precursor solitons [48] and shocks [32, 82, 83] in a dusty plasma medium caused by a supersonic flow of the dusty plasma over a stationary charged object. When such metallic object is kept in contact with the plasma, a space charge regions forms around it which is known

as sheath. Sheath formation is a ubiquitous phenomena and that have been extensively studied [141–144] both theoretically and experimentally over the past few decades. These studies reveals that the sheath or a potential structures forms around a physical boundary due to difference in the mobility of electrons and ions that leads to a preferential negative charging of the object.

The earlier experiments on the excitations of nonlinear waves in a flowing dusty plasma require precise measurements of the potential structures around such floating/biased electrodes in order to obtain a better understanding of the nonlinear excitation process and a more realistic theoretical interpretation of the same. The work presented in this chapter is motivated by the need to know the size and shape of such potentials in flowing dusty plasma experiments in DPEx device that are aimed at exciting nonlinear wake structures [48,83] without disturbing the plasma. To measure the potential structure around a charged object, a dust particle is used as a dynamical micro probe for various discharge parameters.

A variety of electrostatic probes are widely used to measure plasma parameters and potential structures in a plasma. The single Langmuir probe [145, 146] is one of the oldest such diagnostic tools used to measure plasma parameters. However when used for measurements inside the sheath region the results can get skewed as the probe itself develops a sheath around it which interacts with the sheath profile to be measured. Floating emissive probes are more effective and widely used to measure the space and plasma potential profiles even in the sheath region in a variety of plasmas ranging from DC and RF discharges to tokamak plasmas [146–150]. The emissive probe [147] works on the principle of electron emission when the probe is biased below the plasma potential. However, as with other diagnostics techniques, the emissive probe also suffers from a few drawbacks. One drawback

is that the presence of a magnetic field and large density gradients may result in space charge effects creating a significant difference in the measured and actual potentials. Sometimes, the mechanical contacts to the probe lead to non-uniform emission of electrons which can introduce inaccuracies in the measurements. Because of the high continuous emission of electrons from the filaments, the probe degrades with time and finally breaks. Due to this reason, the emissive probe cannot be operated for a long time. To overcome some of the disadvantages of the conventional emissive probe, laser heated emissive probes [151, 152] are presently used to measure the potential in the sheath region. Laser Induced Fluorescence (LIF) [153, 154] and other spectroscopic techniques have also been used for the sheath profile measurements and are found to be very precise. But these diagnostic techniques require expensive equipment and complicated diagnostics.

The use of dust particles as microprobes in the plasma is another diagnostic technique that has been widely used in the past in various experiments to measure the electric field in the sheath region [155–163]. H. Kersten *et al.* [155] obtained the equilibrium electric field in the sheath by measuring the height and charge of a stationary dust particle that is maintained by a balance of the electrostatic force and the gravitational force acting on it. Samarian *et al.* [157] also used dust particles as probes to estimate the sheath profile in the radial direction of a RF discharge and Inertial Electrostatic Confinement Plasma. Barsner *et al.* [156] measured the local electric field by resonating the particle motion with an applied low frequency AC signal in the central pixel of a segmented adaptive electrode. Hartmann *et al.* [158] rotated dust particles and estimated the horizontal electric field by balancing the centrifugal force with the electrostatic force. Schubert *et al.* [160] have studied plasma sheath structures in complex electrode geometries by

looking at the dust particle's equilibrium position in the associated potentials and field structures. They have further complemented their experimental observations by particle-in-cell simulations. Annaratone *et al.* [163] have looked at the plasma-sheath boundary near an adaptive electrode consisting of a two-dimensional array of single electrodes each individually voltage controllable to produce local modifications in the plasma edge. The nature of these perturbation is studied by using suspended particles as tracers.

In contrast to these single particle tracer studies, that are mainly aimed at diagnosing sheath potential structures in a plasma, E. Thomas and collaborators have over the past few years used the Particle Image Velocimetry (PIV) technique to study the internal dynamics of dust clouds as well as their interactions with high speed charged particle streams [130, 164–169]. However, for measurements of plasma potential structures such as sheath profiles it is more convenient to track a single dust particle which acts as a non-perturbative microprobe. Most past studies using the microprobe methodology have relied on a series of static local measurements to map the profile of plasma potential structures. In our present work we employ the microprobe in a dynamical fashion by continuously tracking the trajectory of a moving particle to provide a direct visualization of the potential profile. By launching the trace particle at different velocities it is possible to probe different regions of the potential structure.

We demonstrate this method experimentally by measuring the potential profile around a grounded wire that is mounted on the cathode of a DC glow discharge plasma. A few micron sized Melamine Formaldehyde (MF) particles introduced in the plasma get negatively charged and are trapped vertically in the sheath region of the cathode. They are further brought to an equilibrium stationary state in the

horizontal direction by balancing the pumping speed and gas feeding rates in the device [115]. The particles are then made to flow over the wire by a sudden change in the gas flow rate. The individual particle trajectories are tracked by analyzing the video images of their motion and the strength of the potential are deduced by using simple energy conservation arguments.

The chapter is organized as follows: In the next section (Sec. 4.2) a detailed description of the experimental set up along with the production procedure of the plasma and the introduction of dust tracer particles is given. The experimental results and the detail discussion on the experimental findings are discussed in Sec. 4.3. Sec. 4.4 provides a brief summary and discussion on our findings.

4.2 Experimental set-up and procedure

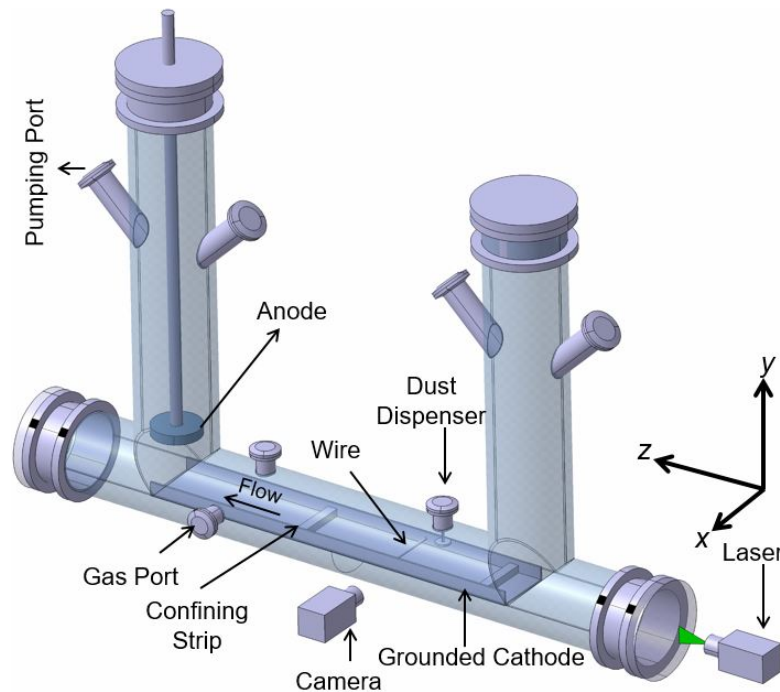


Figure 4.1: A schematic diagram of dusty plasma experimental (DPEX) setup.

The experiments are performed in Dusty Plasma Experimental (DPEX) device, whose schematic diagram is shown in Fig. 4.1. It is basically an inverted Π -shaped device which has several axial and radial ports for different purposes. The detailed description of instrumentation and its diagnostics are discussed in Chap. 2. A Direct Current (DC) glow discharge Argon plasma is created in between the circular shaped anode and long tray cathode. To measure the potential profiles around a charged object over a range of discharge conditions, a copper wire is mounted on the cathode in between two axial confining strips. This copper wire acts as a stationary charged object in the plasma environment. In this set of experiments, the copper wire is always kept at grounded potential, however there is a provision to bias it to a potential in between the grounded and floating potential.

To begin with, the experimental vessel is pumped down to a base pressure of 0.1 Pa by a rotary pump. Argon gas is then flushed in the device several times with the help of a gas flow controller and every time the vacuum vessel is pumped down to the base pressure to remove impurities from the vessel. Finally the working pressure is set to 10–20 Pa by adjusting the pumping rate and the gas flow rate. A plasma is then initiated by applying a voltage in the range of 280 to 360 V over which the plasma current varies from 1 to 10 mA. With the creation of a plasma the wire mounted on the grounded cathode acquires a sheath around it.

A few mono-dispersive MF particles of radius $r_d = 4.45 \mu\text{m}$ and mass $m_d = 5.57 \times 10^{-13}$ kg are introduced into the plasma by shaking the dust dispenser. In the plasma environment these particles get negatively charged and levitate in the cathode sheath region just $\sim 5 - 20$ mm above the cathode. The exact height of the levitation depends on the discharge condition. To illuminate these micro particles in the yz plane, a green laser is used. The Mie scattered light from

the dust particles is captured by a CCD camera and recorded in a computer for analyzing the dust dynamics.

To initiate the flow of dust particles over the stationary wire, the Single Gas Injection (SGI) technique is used as discussed in detail in Ref. [137] and in Chap. 2.7.1. In this technique, an equilibrium condition of the dust particles is achieved at first by adjusting the pumping speed and the gas flow rate. The stationary dust particles are then made to flow by a sudden momentary decrease of the gas flow rate. During the flow, the particles are seen to move from right to left and they come back to their original position when the flow rate difference is set to original value. When the flow rate difference is increased beyond 5.5 sccm the particles move towards the pump with a higher velocity and cross the potential barrier created by the wire and finally fall down on the left edge of the glass tube where the cathode ends. The trajectory of the particle, as video recorded, is then used to find the strength and profile of the barrier produced by the wire which will be discussed in detail in the next section (in Sec. 4.3.4).

4.3 Results and discussion

4.3.1 Generation of flow and closest approach

As discussed above, the injected particles attain a stable equilibrium when the pumping rate gets exactly balanced by the gas flow rate. In this situation the particles are observed to be confined in the potential well which is in between the right strip and the potential hill of the grounded wire. The particles display only small random displacements due to their thermal energy. Keeping the pumping speed constant when the gas flow rate is decreased, the particles are seen to move

towards the pump (right to left) and approach the grounded wire. If the velocities of these particles are not sufficient to enable them to go over the potential hill, they stay inside the potential well but attain an equilibrium position closer to the wire.

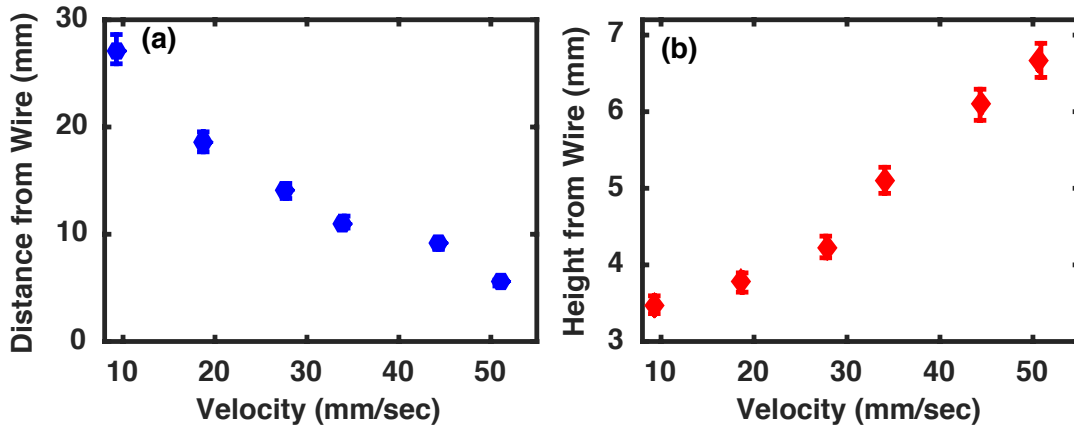


Figure 4.2: Variation of (a) the closest approach and (b) the height achieved by a $4.45 \mu\text{m}$ particle above the charged wire versus the velocity of the micro particle.

The variation of this closest distance of approach and the particle's height above the wire as a function of its velocity are shown in Fig. 4.2 for a gas pressure of $p = 12 \text{ Pa}$ and discharge voltage of $V_d = 320 \text{ V}$. It is clear from Fig. 4.2(a) and Fig. 4.2(b) that the distance of closest approach in the axial direction decreases and the height of the particle increases with an increase of the particle velocity. In this particular condition, the closest distance from the potential hill is seen to be $\sim 5 \text{ mm}$ and the height achieved by the particle is $\sim 7 \text{ mm}$ for a velocity of $\sim 5 \text{ cm/s}$. With a further increase of the gas flow rate and hence an increase in the magnitude of the asymptotic velocity, the particles are found to overcome the confining potential and do not come back in the well.

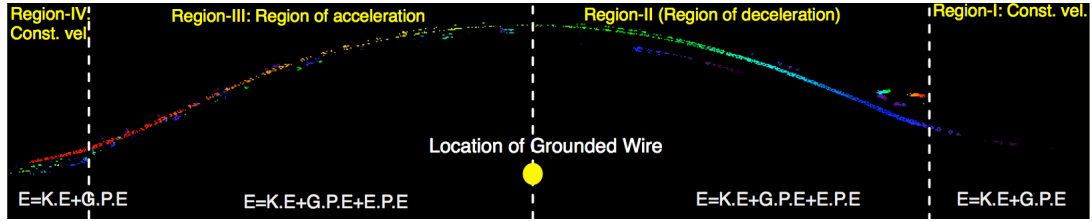


Figure 4.3: Color plot showing the trajectory of the particle, having radius $r_d = 4.45 \mu\text{m}$, while crossing the charged wire at a pressure of $p=12 \text{ Pa}$ and a discharge voltage $V_d = 320 \text{ V}$. The filled circle represents the location of the wire whereas the arrow represents the direction of flow.

4.3.2 Particle trajectory

Fig. 4.3 depicts the trajectory of a particle while moving over the grounded wire. In this case, the asymptotic velocity crosses the threshold value ($\sim 6 \text{ cm/s}$) so that it flows over the grounded wire and crosses the hill. The violet color (extreme right) of the trajectory indicates the particle coordinates at the initial time whereas the red color (extreme left) indicates the coordinates of the same particle at the final stage of its journey. The big solid circle shows the position of the charged wire. It is clear from the figure that the particle almost traces the sheath-plasma boundary (caused by the grounded potential wire) on its way. Very far from the potential wire, the particle moves with the asymptotic velocity (Region-I) towards the confining strip, climbs up (Region-II) the potential hill created by the wire and then moves down (Region-III) from the hill and finally (Region-IV) travels again with almost the same asymptotic velocity that it started with. Using the coordinates of the individual particles we will now deduce the height and width of the potential hill and also delineate the axial and radial profiles of the potential structure. Fig. 4.4 displays the particle trajectories (similar to Fig. 4.3) for two different discharge voltages (Fig. 4.4(a)) and background neutral gas pressures (Fig. 4.4(b)) when all other discharge parameters are kept constant. It is seen

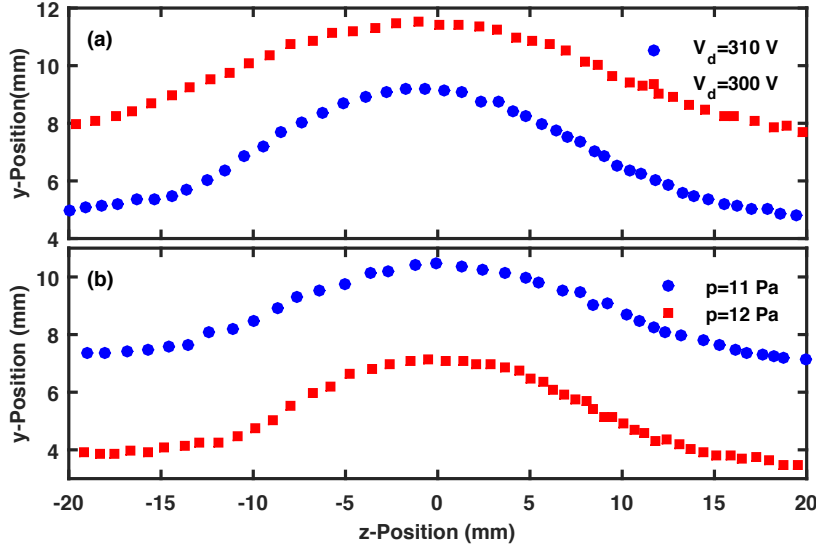


Figure 4.4: A plot showing the trajectories of a particle of radius $a = 4.45 \mu\text{m}$ for different (a) discharge voltages and (b) background neutral pressures.

that the height and the width of the potential hill increases with the decrease of the discharge voltages for a background pressure of $p = 12 \text{ Pa}$ (see Fig. 4.4(a)). A similar trend is seen when the pressure is reduced for a particular discharge voltage $V_d = 310 \text{ V}$. It is also seen from Fig. 4.4 that the z -coordinates of the particles are less spaced when the particles ride the hill near $z = 7 \text{ mm}$ whereas the coordinates are well spaced when the particles come down from the hill near $z = -7 \text{ mm}$. This essentially means that the particle decelerates while climbing up the hill whereas it gets accelerated when moving down the hill. Here the time interval of two consecutive frames is set to be $\sim 9.3 \text{ msec}$.

4.3.3 Variation of size of the potential hill with discharge parameters

Fig. 4.5 shows the variation of the width and height of the potential hill created by the charged wire over a wide range of discharge parameters. It is seen from

Fig. 4.5(a), that both the width and the height of the hill decrease with the increase of the discharge voltage. A similar trend of the changes in the width and height is observed when the pressure is increased from 11 to 15 Pa as shown in Fig. 4.5(b). In both the cases when the voltage or the pressure is increased, the plasma density increases which results in a decrease of the plasma Debye length. As the cathode sheath thickness is a function of the Debye length, hence the sheath thickness around the grounded potential wire decreases with the increase of discharge voltage and the background gas pressure.

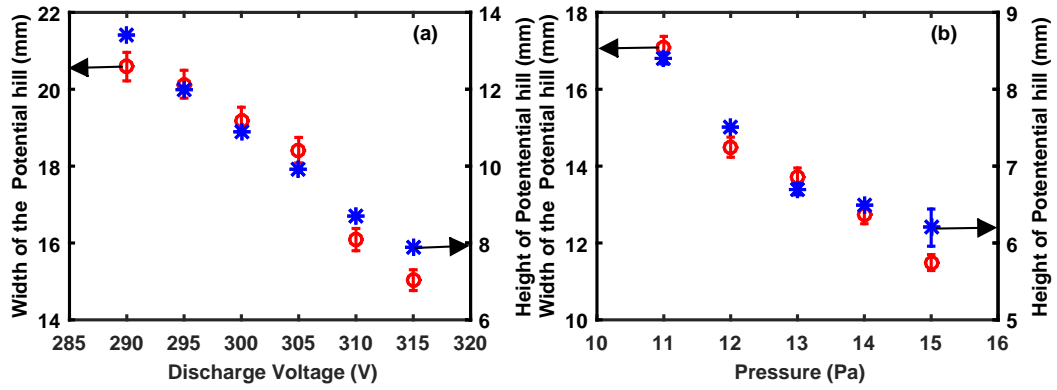


Figure 4.5: Variation of width (star) and height (open circle) of the potential hill created by the charged wire with (a) discharge voltages and (b) background neutral gas pressure.

4.3.4 Energy conservation and estimation of potential

To estimate the axial and radial potential profiles around the grounded object, we can make use of the energy conservation relation,

$$\left[\frac{1}{2} m_d v^2 + m_d g h \right]_{I,IV} = \left[\frac{1}{2} m_d v^2 + m_d g h + Q_d \phi \right]_{II,III} \quad (4.1)$$

where, m_d , v , and h denote the mass, velocity and height of the particles (above

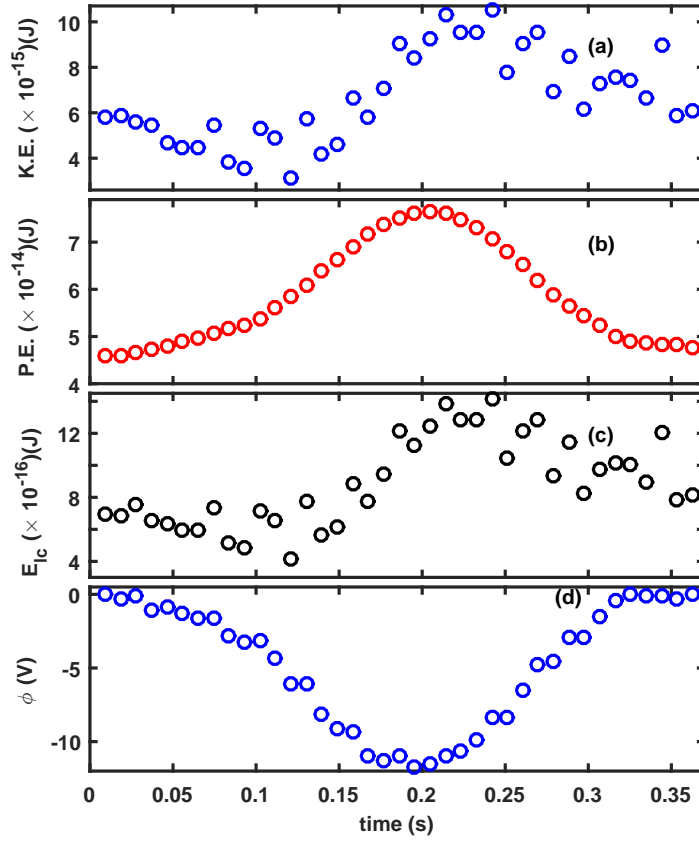


Figure 4.6: Time evolution of (a) kinetic energy, (b) gravitational potential energy and (c) energy loss due to neutral drag force (d) electric potential of a particle of radius $r_d = 4.45 \mu\text{m}$ while riding over a charged object for a given pressure $p = 12$ Pa and voltage $V_d = 320$ V.

the cathode tray), respectively. ϕ is the electrostatic potential created by the grounded wire, g is the acceleration due to gravity and $Q_d (= Z_d e = 4\pi\epsilon_0 r_d U)$ where Z_d is dust charge number and e is the charge of electron and U is the dust surface potential for an Argon plasma (which is negative in laboratory dusty plasmas), ϵ_0 is the permittivity of free space, r_d is the radius of the dust particle. The subscripts *I*, *II*, *III* and *IV* refer to the various regions of the trajectories as indicated in Fig. 4.3. As shown in Fig. 4.3, when the particles stay far from the wire (e.g., Region-I and Region-IV) they move only with the constant kinetic energy (K.E) and the gravitational potential energy (G.P.E). But when they enter in the

sheath region, the dynamics of the particles get changed and they start feeling the presence of the charged wire. Hence in Region-II and Region-III, the components of total energy are kinetic energy, gravitational potential energy and electrostatic potential energy (E.P.E). As a result the potential profile $\phi(z, y)$ created by the wire can be expressed as:

$$\phi(z, y) = \frac{m_d}{Q_d} \left[\left[\frac{1}{2}v_d^2 + gh \right]_{z \rightarrow \infty} - \frac{1}{2}v^2 - gh \right] \quad (4.2)$$

where $v = \sqrt{v_z^2 + v_y^2}$ and h is the height at a particular axial location z . By

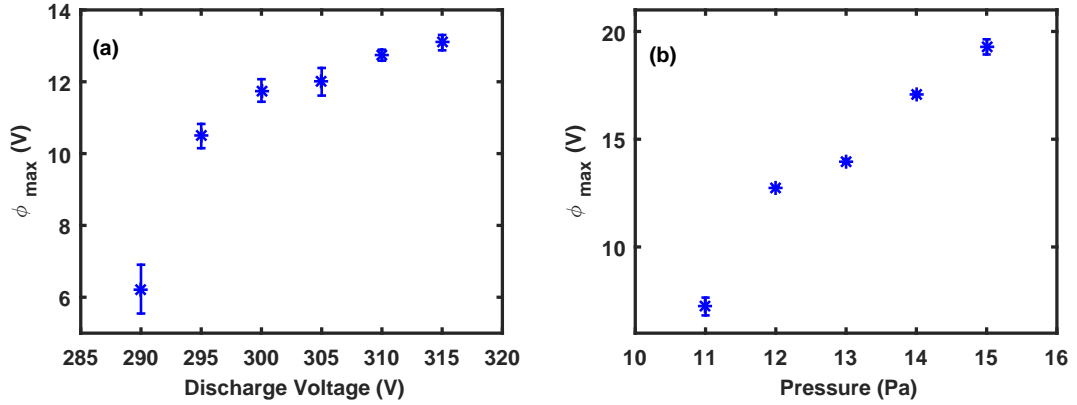


Figure 4.7: Variation of maximum potential calculated from potential profiles for different discharge (a) voltages and (b) gas pressure.

tracking individual particles, the potential profile $\phi(z, y)$ along the trajectory can be estimated with the help of Eq. 4.2.

For determining the potential profile, we first need to estimate the charge acquired by the dust particle in equilibrium. To estimate the dust charge, a Collision Enhanced plasma Collection (CEC) model [124, 125] has been used to first calculate the surface potential, $\phi_s \sim -\tilde{z}k_B T_e/e$ of the dust particle by solving the electron and ion flux balance equations numerically and subsequently an estimate of the charge is made using $Q_d = 4\pi\epsilon_0 r_d U$ assuming that the dust particles are

spherical in shape. For our experimental conditions $p = 11 - 15$ Pa, $T_e = 4 - 2.5$ eV and $n_i = 0.9 - 2 \times 10^{15} / m^3$ [170], \tilde{z} and Q_d come out to be $\sim 1.3 - 1.6$ and $\sim 2.6 - 1.9 \times 10^{-15}$ C, respectively. It is to be noted that for the basic plasma parameters such as T_e and n_i , we have used values previously obtained from actual measurements using a single Langmuir probe for discharges of similar conditions. These have been discussed and reported in Ref. [170]. Here, we have assumed that the charge of the dust particle is almost constant and does not change during its journey. This assumption is based on findings from earlier experiments carried out in the same device and for similar conditions [115]. These experiments have shown that the plasma parameters remain nearly constant along the axial direction (along z). In particular, the constancy of T_e ensures that the charge remains almost constant [122, 171]. When these micro-probes (dust particles) are made to flow over a grounded wire, their kinetic energy and potential energy profiles are measured and it is seen that the particles decelerate while riding up the potential hill and they accelerate while coming down from the hill (see Fig. 4.6(a)). Fig. 4.6(b) indicates that the particle starts its journey at a height of ~ 4.5 mm from the wire and then attains a maximum height and then ends its journey almost at the same height that it started from. It is to be noted that the energy loss due to dust neutral friction is not taken into account in Eq. 4.1. This is a reasonable assumption as it is seen experimentally that the particles display the same kinetic energy and height after climbing down from the potential hill indicating that there is negligible energy loss due to collisional friction with the neutrals. This is a consequence of the experiments being carried out in a low pressure regime. However, in a higher pressure range, where collisional effects may be important, one should consider the energy loss due to dust-neutral collision by subtracting a term, $E_{lc} = F_n dl$ [164] in Eq. 4.1

from both sides, where $F_n (=Nm_n\pi r_d^2 V_{Tn} v_g)$ is the neutral drag force which arises from the collision of the dust with neutral particles. N , m_n , r_d , v_{Tn} , v_g are number density of neutrals, mass of neutral, radius of dust particle, thermal velocity of neutrals and dust grain velocity, respectively. For our experimental conditions this loss varies from $\sim 4.2 - 14.2 \times 10^{-16}$ J as shown in the Fig. 4.6(c) which is nearly one order of magnitude smaller than the kinetic energy and two orders of magnitude than the gravitational potential energy and hence its neglect is justified. With the help of the kinetic and gravitational potential energy profiles, the electrostatic potential profile is estimated using Eq. 4.2 and is shown in Fig. 4.6(d). The electrostatic potential profile follows an almost a symmetric profile around the wire and a similar kind of potential profile was obtained when the floating/plasma potentials were measured using Langmuir and emissive probes [115].

Fig. 4.7 shows the variation of the maximum potential strength (near the location of the wire) created by the wire with a variation of the discharge parameters. The strength of the potential is seen to increase with an increase in the discharge voltage for a constant neutral gas pressure $p = 12$ Pa (Fig. 4.7(a)) or alternatively with an increase in the neutral pressure keeping the discharge voltage fixed at $V_d = 310$ V (Fig. 4.7(b)). A similar trend was observed earlier in experiments reported by Jaiswal *et al.* [115].

4.3.5 Estimation of radial and axial potential profiles around the charged object

To fully explore the radial and axial potential profiles around the grounded wire, we have varied the difference of gas flow rate (and hence the asymptotic velocity) over a wide range such that in all the cases the particles can overcome the potential

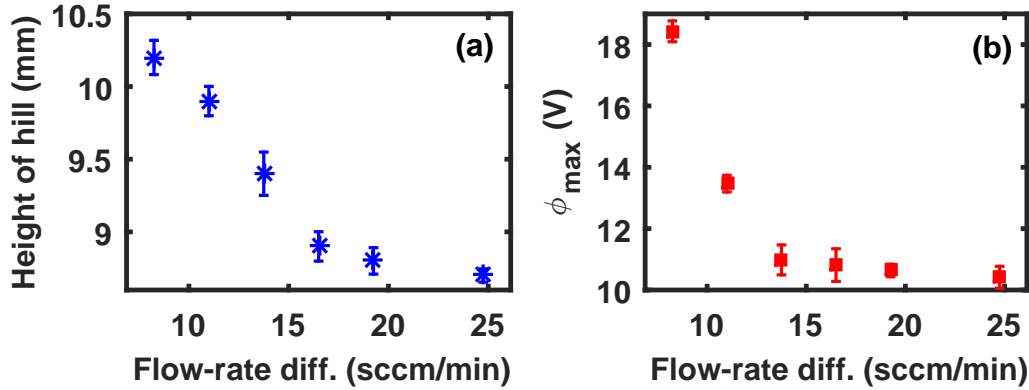


Figure 4.8: A plot showing the variation of (a) the height of the potential with flow rate difference and (b) the maximum potential.

barrier. In each case, the particles gain different asymptotic velocities and as a result in order to satisfy the conservation of total energy, they cross the potential hill at different heights. It is observed that the height of the potential hill decreases when the difference of gas flow rate increases as shown in Fig. 4.8(a). This figure is plotted for a constant gas pressure of $p = 12$ Pa and a constant discharge voltage of $V_d = 320$ V. The strength of the potential, estimated from the conservation of energy, at the peak of the hill is shown in figure Fig. 4.8(b). It clearly indicates that for different values of flow rate difference the strength of potential decreases with height.

To construct the radial potential profile, we plot the variation of potential strength with height as shown in Fig. 4.9. Fig. 4.9(a) shows the radial potential variation for three different axial locations $z = 0$ mm, 6 mm and 16 mm respectively, where $z = 0$ mm corresponds to the location of the wire. It is to be noted that Fig. 4.8(a) and Fig. 4.8(b) have been used to plot Fig. 4.9(a). A similar exercise is done to construct the potential for other two axial locations. Fig. 4.9(a) shows that the magnitude of the potential increases in all the cases when one goes away from the sheath created by the grounded wire towards the bulk plasma in

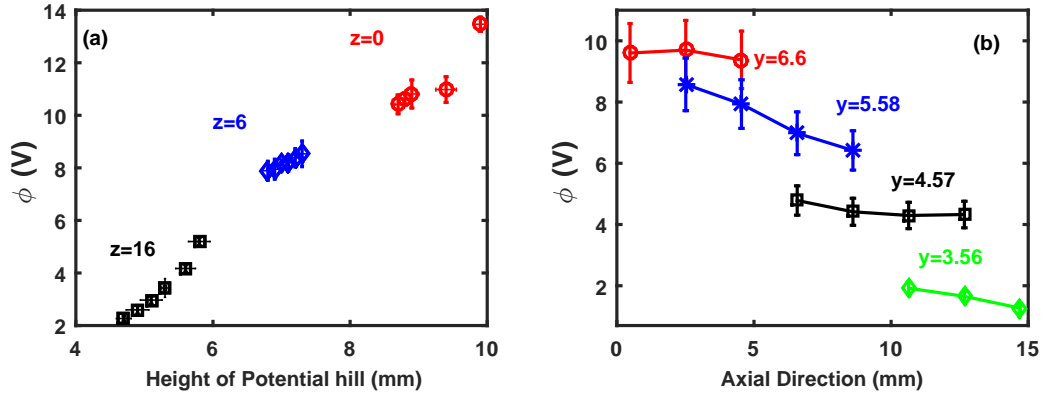


Figure 4.9: (a) Radial potential profiles at $z=0$, $z=6$ mm and $z=16$ mm. $z=0$ corresponds to the location of the wire. and (b) Axial potential profiles at $y=6.6$, $y=5.58$ mm, $y=4.57$ mm, $y=3.56$ mm

radial direction. However, the potential rise is maximum at the location of the wire as compared to the other axial locations. Fig. 4.9(b) shows the variation of potential strength in axial direction for four different radial locations $y = 6.6$ mm, $y = 5.58$ mm, $y = 4.57$ mm and $y = 3.56$ mm. It is clear from this figure that the variation of potential is not significant as we move away from the wire axially for a particular radial location.

4.4 Conclusion

In conclusion, we have experimentally demonstrated a simple technique to measure the potential around a charged object using the flow of a few tracer dust particles. The experiments have been carried out in the DPEx device in which an Argon discharge was initiated between a disc shaped anode and a grounded long cathode. A few micron sized dust particles were then introduced into the plasma, which were found to float near the cathode sheath boundary. A steady state equilibrium of the dust particles was achieved by a fine tuning of the pumping speed and gas

flow rate. A flow of the dust particles was then initiated by a sudden decrease of the mass flow rate of neutral gas. As a result the particles traveled over the grounded wire which was placed on the path of the particles. From a knowledge of the instantaneous position of the particles and their velocities, their potential and kinetic energies were estimated over a wide range of discharge parameters. The axial and radial electrostatic potential around the charged object was estimated by employing the conservation of total energy. In this technique, the particles act as dynamic micro-probes and measure the potential very precisely without significantly perturbing the potential around the charge object. Our experimental results show that the potential around a small charged object has a symmetric profile in the axial direction whereas it has a parabolic shape in the radial direction and the dimension of the potential shrinks in all directions with an increase of the discharge voltage and the background neutral gas pressure.

5

Excitation of precursor solitons, its dependence on the shape and the size of the charged object

Part of this chapter is published in *Phys. Plasmas*, **26**, 093701 (2019) by Garima Arora *et al.*.

5.1 Introduction

The simultaneous excitation of precursor solitons ahead of a fast moving object with wakes behind it, is a phenomenon that has been widely studied in hydrodynamics particularly in the context of disturbances created by ships and boats close to the coast [172–174]. These earlier studies have also provided model descriptions

of this fascinating non-linear phenomenon by employing a forced Korteweg de Vries equation or a forced generalized Boussinesque equation [45]. Controlled laboratory experiments using model ships moving in a channel were carried out by Huang *et al.* [175] and Sun [46]. It was found that as long as the speed of the object moving through the fluid (water) was below a critical value (in this case the phase velocity of the surface water waves) the movement only created the customary trailing waves (wakes) in the downstream direction. A dramatic change occurred when the object speed was trans-critical. In addition to the trailing wakes the object also created a steady stream of solitons ahead of it in the upstream direction. These solitons with a speed higher than the object moved away as precursors. The phenomenon was Galilean invariant [45], which could be reproduced by keeping the object stationary and moving the fluid over it.

Fluid concepts have often been successfully translated and exploited to understand collective phenomena in plasmas. A prime example is the extensive past study of linear waves and nonlinear structures in a dusty (or complex) plasma medium. Such a medium, consisting of heavy dust grains immersed in a plasma of electrons and ions, display a host of collective excitations on a slow time scale due to the low charge to mass ratio of the dust particles and can be understood from a fluid model of the dusty plasma. There is a rich literature on the study of linear waves *e.g.* the Dust Acoustic Wave (DAW) [27, 176], the Dust Ion Acoustic Wave (DIW) [70], Dust Lattice Waves (DL) [29] and non-linear waves like Dust Acoustic Solitary Waves (DASw) [30, 177], Shock Waves [33, 82], dust voids [34, 36, 37], Vortices [38, 39, 178] etc [179] consisting of both theoretical and experimental investigations. As in a hydrodynamic fluid, there have also been observations of wake structures in laboratory dusty plasmas [40, 178, 180]. These wakes (some-

times termed as Mach cones [22, 23, 41–43]) are generated when a dust particle moves through a stationary dusty plasma medium. The topic of forewake excitations (precursor waves) has however received very limited attention till now. The first experimental demonstration of the generation of a precursor soliton in a flowing dusty plasma is reported in 2016 by Jaiswal *et al.* [48]. In their study they observed the spontaneous excitation of precursor solitons when a super-sonically (with respect to the dust acoustic speed) moving dusty plasma fluid is made to flow over an electrostatic potential structure. The physical mechanism underlying this phenomenon is understood in terms of the fluid concept used to explain hydrodynamic precursors. An object moving in a fluid always creates a pileup of matter in front of it. If its speed is sub-critical then the matter in front can disperse away at the linear phase velocity leading to the creation of a wake structure. However if the object speed is super-critical then the matter in front cannot disperse away fast enough and continues to build up. At a certain stage nonlinear effects become important and this can lead to the formation of solitons or other nonlinear structures. These nonlinear structures can move at a higher speed and can therefore separate from the object and move away as precursors. These first ever observations of precursor solitons in a plasma have been well characterized by detailed experimental measurements of their propagation features and qualitative comparisons with results from theoretical models. The existence of such precursor excitations have also been confirmed from full scale fluid simulations [50] as well as molecular dynamic simulations [51].

The objective of the work presented in this chapter is to further consolidate and extend the previous experimental study [48] by carrying out a detailed investigation of the propagation characteristics of the precursors under varying excitation

conditions. In particular, we look at the effects of varying the size and shape of the potential hill on the fore-wake phenomenon. We find that there is a systematic dependence of the amplitude, velocity and number of excited precursors on the size of the potential hill and the existence of a threshold value of the potential height below which no precursors are excited. There is also a very interesting dependence on the shape of the potential hill that highlights the role of sharp gradients in the excitation of precursors.

This chapter is organized as follows: In the next section (in Sec. 5.2) we describe the experimental setup and procedure for excitation of precursor solitons and wakes. The experimental results of precursor solitons and wakes are discussed in Sec. 5.3.1 and the associated theoretical model is discussed in Sec. 5.3.2. The excitation of these forced solitary waves over different sizes of the potential profile of the charged object are described in Sec. 5.3.3 and the results on the influence of the shape of the potential profile are described in Sec. 5.3.4. A brief summary of all the results and some concluding remarks are given in Sec. 5.4.

5.2 Experimental set-up and procedure

The full set of experiments are performed in Dusty Plasma Experimental (DPEx) device and its schematic diagram is shown in Fig. 5.1. A detailed description of the experimental setup and its associated diagnostics are available in Chap. 2. The experiments presented in this chapter mainly deals with the excitation of waves in a flowing dusty plasma, which is made to flow over a charged object either subsonically or supersonically. For this purpose, a copper wire of diameter 1 mm and length 50 mm is mounted at a height of 10 mm from the base of the cathode. This copper wire serves as a charged object in the plasma environment. The wire

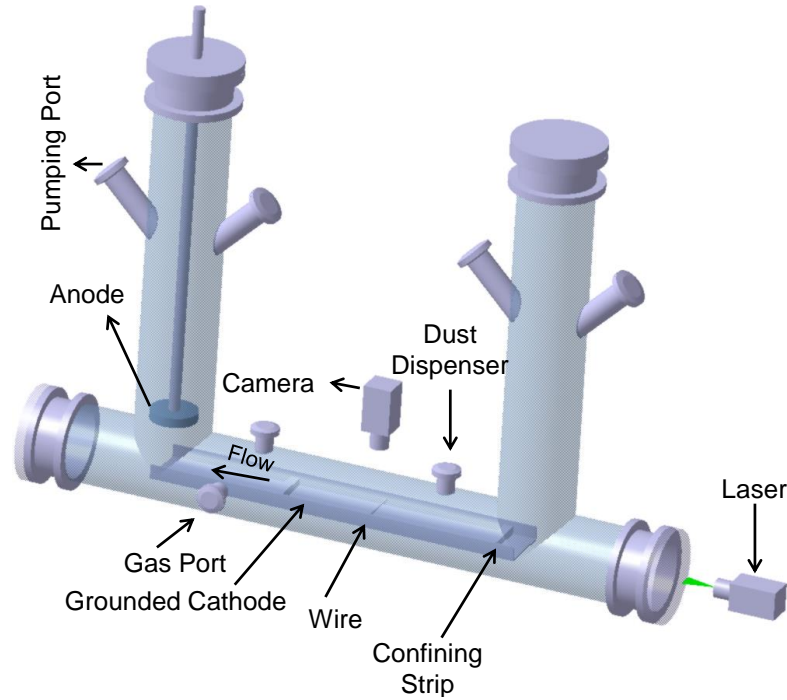


Figure 5.1: A schematic diagram of dusty plasma experimental (DPEX) setup.

is connected to the grounded potential through a switch and it can also be kept at various potentials by connecting a variable resistance ranging from $10\text{ k}\Omega - 10\text{ M}\Omega$ in between the wire and the switch. The potential around this charged object in presence of plasma can be measured using dust particles as dynamic micro probes and is discussed in details in Chap. 4.3.3.

Micron sized Kaolin particles of diameter $2\text{-}5\ \mu\text{m}$ are sprinkled on the cathode in between the wire and the right strip before closing the chamber for creating a dusty plasma. These dust particles get negatively charged in the presence of the background plasma and levitate in the cathode sheath region where the sheath electrostatic force acting on the particle balances the gravitational force. The mass of the levitated dust particles $m_d \sim 8.9 \times 10^{-14}\text{ kg}$ for a radius of $r_d = 2.0\ \mu\text{m}$. These levitated micro particles are then illuminated by a green laser light and their dynamics are captured by a fast CCD camera for further analysis. To start with,

the chamber is pumped down to a base pressure of 0.1 Pa and then Argon gas is injected into the device to set the working pressure at 9-15 Pa. In this condition the gate valve attached with the pump is opened at 20% whereas the mass flow controller is opened at 5% to maintain the equilibrium pressure in the chamber. An Argon plasma is produced between the anode and grounded cathode by applying a voltage in the range of 280-320 V using a DC power supply. The plasma parameters like plasma density (n_i) and electron temperature (T_e) are measured using a single Langmuir probe and they come out to be $n_i \sim 0.5 - 3 \times 10^{15}/\text{m}^3$ and $T_e \sim 2 - 5$ eV for the range of discharge conditions as discussed in details in Chap. 2.5. To create a dusty plasma, first the plasma is formed at a higher voltage and left for a few minutes. Later, the discharge voltage is reduced and set accordingly so that a highly dense dust cloud is formed. To repeat the earlier observations of Jaiswal *et al.* [48] the wire is kept at ground potential (negative compared to the plasma potential), which acts as a barrier for these negative charged dust particles and as a result the particles remain confined between the wire and the right potential strip as shown in Fig. 5.2(a) and exhibit only thermal motion. For the present set of experiments, the discharge condition is kept in such a way that there is no spontaneous excitation of waves in dust cloud due to ion streaming. For a specific discharge condition, $V_d = 320$ V and $p = 11$ Pa, the average charge of these micron sized dust particles comes out to be $Q_d \sim 8.4 \times 10^3 e$ which is estimated from a Collision Enhanced plasma Collection Model (CEC) as discussed in Chap. 2.6.2. The other dusty plasma parameters like dust density $n_d \sim 10^{11}/\text{m}^3$ and dust temperature $T_d \sim 0.6 - 1.2$ eV are estimated with the help of an IDL based super Particle Identification Tracking (sPIT) code, which is also discussed in Chap. 2.8.2. Based on the above parameters the phase velocity of the Dust Acoustic Wave

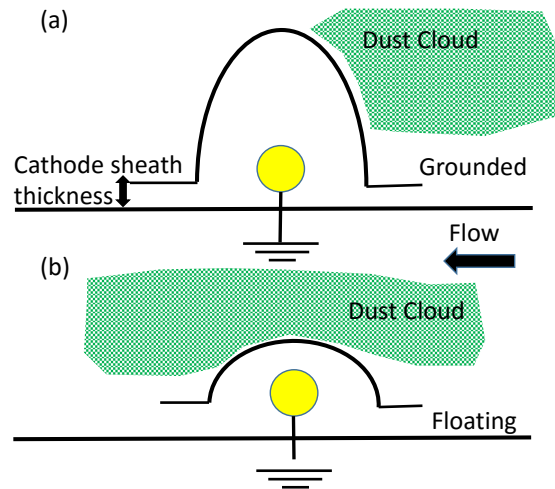


Figure 5.2: (a) Equilibrium configuration of dust cloud before generating the flow. (b) Dust flow initiated by lowering the potential hill suddenly by making it floating. The yellow circle represents the location of charged object and flow is generated from right to left.

(DAW) turns out to be $C_{da} \sim 20$ mm/s. To compare the theoretical estimation, a separate experiment is also carried out to excite DAW for the above discharge condition by applying a sinusoidal signal to the wire. It is found that the measured C_{da} comes out to be ~ 25 mm/s, which is in good agreement with the estimated value.

5.2.1 Generation of flow in the dust fluid

For the excitation of forced solitary waves and wake structure, the dust particles are made to flow over the wire. The flow of the dust cloud is generated by suddenly lowering the height of the negative potential hill created by the charged object. This technique of flow generation and the measurement of flow velocity is discussed in Chap. 2.7.1. As discussed, when the wire is switched to near floating potential the potential hill is lowered and the dust particles flow from right to left over the wire as shown in Fig. 5.2(b). During the flow, the dust particles attain a constant

velocity due to neutral drag force [135, 181] and excite solitary waves along with wakes depending on the flow velocity of dust fluid. The flow velocity of dust fluid is measured by tracking the individual particles at the tail of the cloud using Particle Image Velocimetry (PIV) technique [119]. The velocity of the dust fluid is changed from subsonic ($\sim 15 - 18$ mm/s) to supersonic ($\sim 25 - 32$ mm/s) values by varying the discharge parameters. To study the propagation characteristics of the excited structures, the size (both height and width) of the potential hill created by the charged object is altered by changing the resistance connected to the wire, whereas the shape of the potential profile is modified by using objects of different shapes. These studies are discussed in the subsequent sections (in Sec. 5.3.3 and Sec. 5.3.4).

5.3 Results and Discussion

5.3.1 Excitation of precursor solitons and wakes

Before investigating the dependence of shape and size of the potential hill on the precursor solitons, the past experiment of Jaiswal *et al.* [48] is repeated to serve as a benchmark. The results are shown in Fig. 5.3 and Fig. 5.4. It is seen in Fig. 5.3

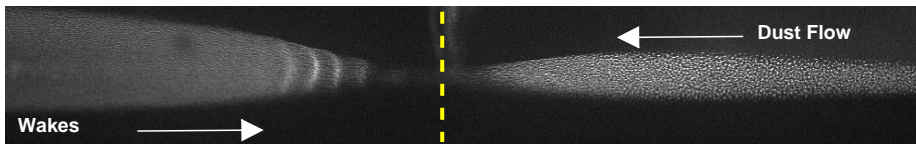


Figure 5.3: Propagation of wakes in the direction of flow (in downstream direction) for the case of subsonic flow. The position of wire is represented by the yellow dashed line.

that only wakes are excited in the direction of flow when the flow velocity of dust fluid is subsonic. The dust fluid flows from right to left and hence in the frame of the fluid the charged object (i.e. the wire) moves subsonically from left to right

and excites faint intense wake structures, which is observed to propagate in the downstream direction. Interestingly when the velocity of the dust fluid is changed to a supersonic value, few intense bright structures appear in the dust fluid along with the wake structures. Fig. 5.4(a) depicts such a scenario for a supersonic flow of

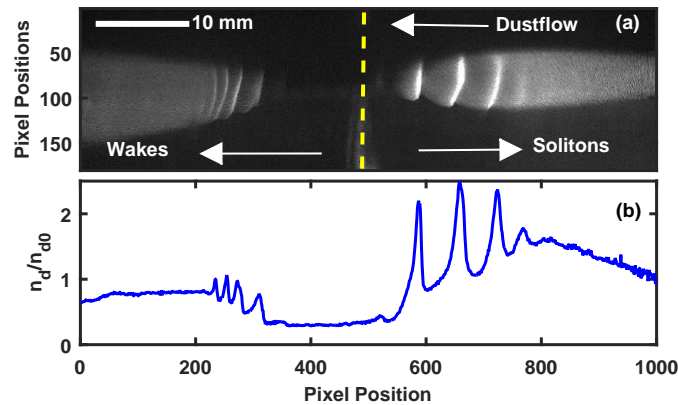


Figure 5.4: (a) Propagation of solitons against the direction of flow (in upstream direction) and wakes in the direction of flow (in downstream direction) for the case of supersonic flow. The position of wire is represented by the yellow dashed line. (b) The intensity profile of the solitons and wakes.

dust fluid. In this case, the object still moves from left to right supersonically and the higher amplitude solitary structures, known as precursor solitons, propagate in the upstream direction faster than the object, whereas the smaller amplitude wakes are found to propagate in the downstream direction. Fig. 5.4(b) shows the normalized amplitudes of solitary and wake structures extracted from Fig. 5.4(a). It is clear from the figure that the solitary structures (right of the object) are brighter and hence are larger in amplitude than the wakes. These nonlinear structures can be identified as KdV type solitons as was shown in details by Jaiswal *et al* [48]. These nonlinear precursor structures are confirmed to be solitons by estimating the quantity $amplitude \times width^2$, which remains constant over the time [30].

5.3.2 Theoretical model for the precursor solitons

The *forced*-KdV [49] model equation is solved as part of the benchmark exercise to obtain a qualitative account of the phenomenon. To model our experimental findings, an unmagnetized weakly collisional dusty plasma having electrons, ions and negatively charged dust grains is considered. In this model, the electrons and the ions are assumed to be Boltzmann distribution at temperatures T_e and T_i , respectively, whereas the fluid equations are solved for the dust particles. The fluid equations associated with the dust are given below:

$$\frac{\partial n_d}{\partial t} + \frac{\partial(n_d u_d)}{\partial x} = 0 \quad (5.1)$$

$$\frac{\partial u_d}{\partial t} + u_d \frac{\partial u_d}{\partial x} = \frac{\partial \phi}{\partial x} \quad (5.2)$$

$$\frac{\partial^2 \phi}{\partial x^2} - n_d - \alpha_e e^{\sigma \phi} + \alpha_i e^{-\phi} = S(x - v_d t) \quad (5.3)$$

where n_d , u_d , ϕ are the density, velocity and electrostatic potential of the dust fluid, respectively. $\alpha_e = \frac{n_{e0}}{Z_d n_{d0}}$, $\alpha_i = \frac{n_{i0}}{Z_d n_{d0}}$, are the constants and Z_d is the dust charge number. The term $S(x - v_d t)$ represents the presence of charged object (called as source term) moving with a velocity v_d from the frame of the fluid. The above equations are normalized as $x \rightarrow \frac{x}{\lambda_D}$, $t \rightarrow t\omega_{pd}$, $\phi \rightarrow \frac{e\phi}{k_B T_i}$, $n_d \rightarrow \frac{n_d}{n_{d0}}$, $u \rightarrow \frac{u_d}{C_D}$, where $\lambda_D = (\frac{\epsilon_0 k_B T_i}{n_{d0} Z_d e^2})^{1/2}$ is the dust Debye length, $\omega_{pd} = (\frac{n_{d0} Z_d^2 e^2}{\epsilon_0 m_d})$ is the dust plasma frequency and $C_D = (\frac{Z_d k_B T_i}{m_d})^{1/2}$ is the dimension of velocity.

A standard reductive perturbation technique is used to derive the f-KdV equation in which all the dependent variables are expanded in a power series in terms of small expansion parameter ϵ as

$$\Psi = \Psi_0 + \epsilon \Psi_1 + \epsilon^2 \Psi_3 + \dots, \quad (5.4)$$

where $\Psi = (n_d, u_d, \phi)$, $S(x - v_d t) = \epsilon^2 S_2(x - v_d t)$ and the unperturbed quantities denoted by subscript “0”. A suitable set of stretched coordinates are defined as:

$$\xi = \epsilon^{1/2}(x - v_{ph}t), \tau = \epsilon^{3/2}t \quad (5.5)$$

where v_{ph} is the phase velocity normalized by C_D . Using the above equations (Eq. 5.1-Eq. 5.5) and comparing the coefficients of same power of ϵ , one can obtain the final forced-KdV Eq. 5.6 as:

$$\frac{\partial n_{d1}}{\partial \tau} + A n_{d1} \frac{\partial n_{d1}}{\partial \xi} + \frac{1}{2} \frac{\partial^3 n_{d1}}{\partial \xi^3} = \frac{1}{2} \frac{\partial S_2}{\partial \xi}, \quad (5.6)$$

where the source term (S_2) represents the charged object, n_{d1} is the perturbed density normalized to the equilibrium density n_{d0} and $\xi(t)$ is the coordinate in the wave frame moving at the phase velocity u_{ph} normalized to the dust acoustic speed. The coefficient ‘A’ associated with Eq. 5.6 depends upon the electron and ion temperatures and the plasma density. A detailed description of the f-KdV model equation and its solution can be found in Ref. [49]. The source function S_2 ,

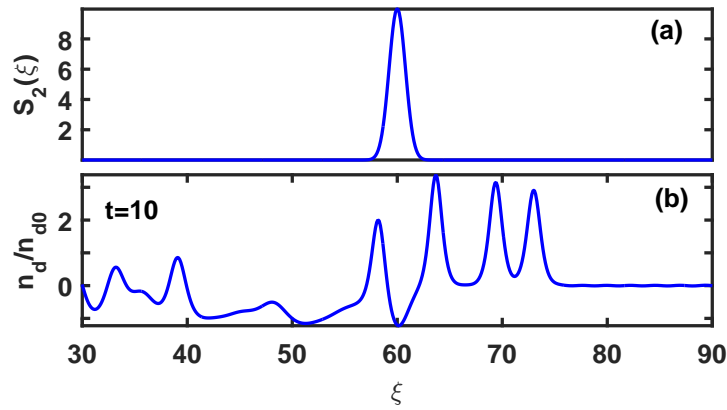


Figure 5.5: (a) Source function (b) Precursor solitons and wakes obtained from the numerical solution of f-KdV equation.

as shown in Fig. 5.5(a), is chosen as a Gaussian with amplitude A_s and width G . Fig. 5.5(b) shows the spatial variation of density perturbation which is obtained by solving f-KdV equation (Eq. 5.6) numerically. In this simulation, the Gaussian source function is made to move from left to right either subsonically or supersonically similar to the wire in the experiments. The coefficient A is chosen to be 4 for our experimental parameters. As shown in Fig. 5.5(b), just like the experimental observation, the numerical solution of f-KdV equation yields the excitation of precursor solitons which propagate in the upstream direction whereas the wakes move in the downstream direction. The solution of f-KdV equation will be further used in this chapter to model the present set of experiments exploring the effect of the size and shape of the obstacle on the excitations of solitonic structure.

5.3.3 Effect of size of charged object on the excitation of precursor solitons

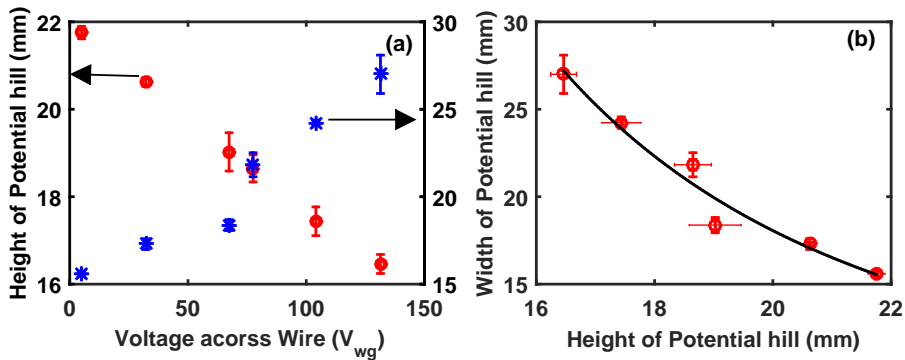


Figure 5.6: (a) Variation of height (represented by red open circles) and width (represented by blue star) of the potential hill with V_{wg} . (b) Power law fit on the height and width of the electrostatic potential created by the charged wire.

The benchmark experiments are executed by changing the height of the potential hill from its maximum value (grounded potential) to its minimum value

(floating potential) to excite the precursor solitons. To investigate the effect of the size (height and width) of the potential hill on the phenomenon, a systematic set of experiments are performed by connecting a variable resistance in series with the wire to change the size of the potential hill. The size of the potential hill of the charged object is adjusted by drawing a current through various resistance values ranging from 10 k Ω to 10 M Ω and measuring the voltage (V_{wg}) across the resistance. To begin with, the height and width of the potential hill is measured

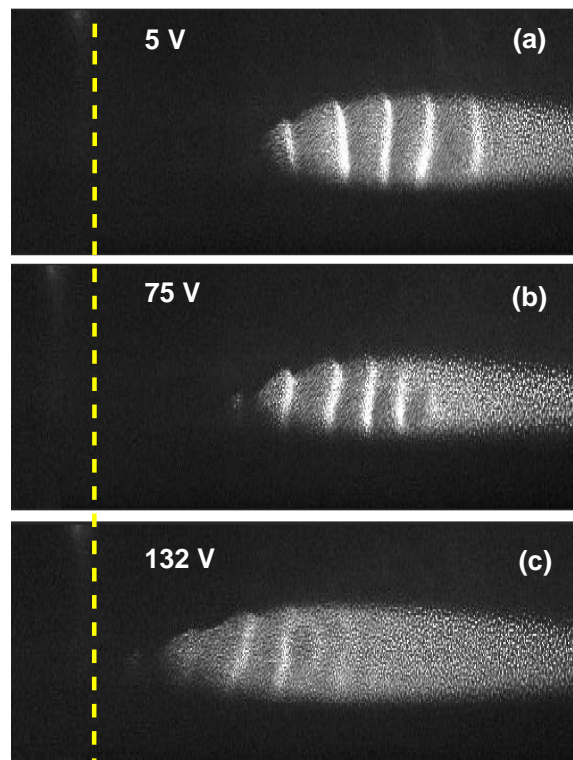


Figure 5.7: Excitation of precursor solitons for (a) 5 V, (b) 75 V, (c) 132 V by varying the voltage across the hill created by the charged wire.

using dust particles as a dynamic micro probes as discussed in Chap. 4.3.3. In this technique, these tracer particles are made to flow over the potential hill and tracking of the individual particle trajectories yields their positions and velocities over the time. The potential of the electrostatic hill is then directly estimated by using

the energy conservation arguments. The height and the width of the potential hill is measured for a wide range of V_{wg} and plotted in Fig. 5.6. Fig. 5.6(a) shows the variation of height (represented by ‘o’) and width (represented by ‘★’) of the potential hill created by the charged object with voltage measured (V_{wg}) across the different resistance connected with the wire in series. It can be seen that the height of the hill decreases and width increases with the increase of V_{wg} . The height of the potential hill is maximum when V_{wg} becomes close to the grounded potential which is negative with respect to the plasma potential and it decreases when the voltage drop across the variable resistance reaches towards the plasma potential which is ~ 300 V for this specific set of experiments. The variation of the height (h) with width (w) of the potential hill created by the wire is plotted in Fig. 5.6(b) and it is seen that the width decreases with an increase of the height of the potential hill. The solid line represents the power law relationship ($h \sim w^{-3.13}$) between the width and height. Further experiments are performed with similar range of V_{wg} to examine the effect of the size of the potential hill on the excitation of forced solitary waves.

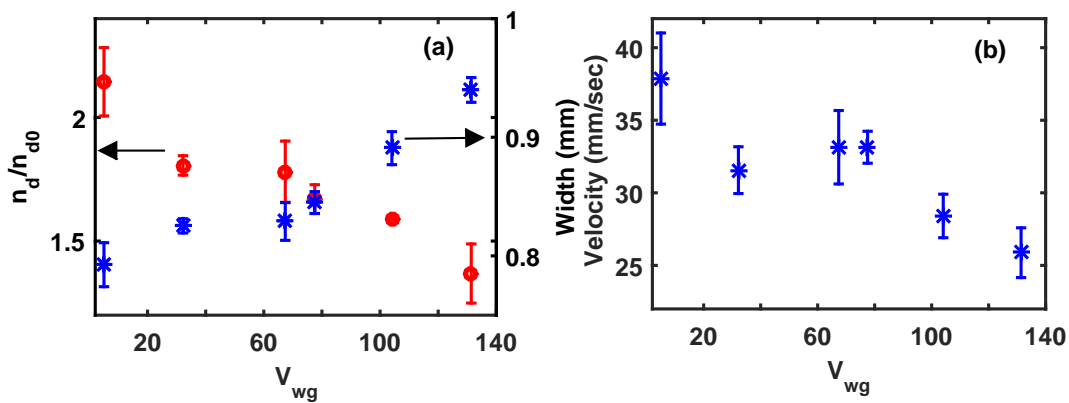


Figure 5.8: Variation of (a) amplitude (represented by red open circles), width (represented by blue star) and (b) velocity of the excited precursor solitons for the case of supersonic fluid flow with the voltage drop V_{wg} across the resistance.

Fig. 5.7 shows typical images of fully developed forced solitary structures. It visually shows how the number, amplitude and width of solitons changes with the wire potential, V_{wg} . Fig. 5.7(a) shows the solitary waves at $p = 11$ Pa and $V = 320$ V when V_{wg} is kept at 5 V which is approximately at grounded potential. The dotted line in this figure represents the location of the wire. For $V_{wg} = 5$ V, five prominent solitary waves get excited which are found to propagate in the upstream direction from the frame of fluid. When the resistance connected to the wire is increased such that $V_{wg} \sim 75$ V, the number of prominent solitary structures decreases to four as shown in Fig. 5.7(b). The number further decreases to two when the V_{wg} is increased to 132 V as shown in Fig. 5.7(c). If the potential of the wire is increased further towards the floating potential, the height of the source object decreases and it is not sufficient to excite any forced solitary structures. We have also found the threshold value, $V_{wg} = 135$ V, beyond which the particles simply flow and do not excite any wave structures. It is also found that the amplitude decreases whereas the width of the fully developed solitons increases with the increase in V_{wg} but the change is not visually appreciable. A more quantitative discussion of the variation of amplitude, width and velocity with V_{wg} is given later in this section. In all these experiments (Fig. 5.7(a-c)), the dust velocity is measured using PIV analysis to make sure that the dust fluid moves supersonically over the wire.

Fig. 5.7 qualitatively shows that the amplitude of the solitary structures decreases whereas width increases with the increase of V_{wg} . For a quantitative analysis of the amplitude (n_d/n_{d0}) of solitary wave, the maximum intensities are extracted from the images later normalized by the equilibrium intensity of dust density. Fig. 5.8(a) shows the variation of this amplitude of forced dust acoustic solitary waves (f-DASw) with V_{wg} . It shows that the amplitude of these excited

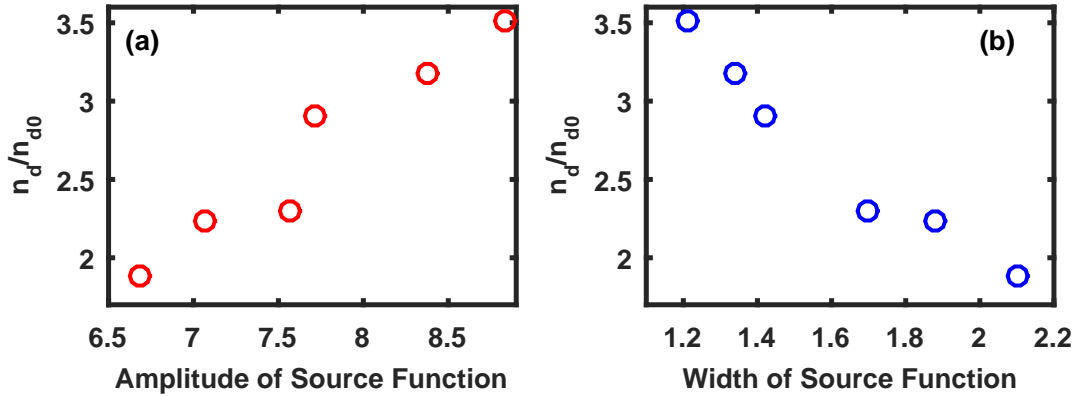


Figure 5.9: Variation of amplitude of solitons with (a) amplitude of source, (b) width of source numerically obtained from the solution of f-KdV.

solitary waves decreases whereas the width increases with the increase in V_{wg} . It can also be seen in Fig. 5.6(a), that the height of the potential hill decreases whereas the width increases with the increase of V_{wg} . It essentially indicates that the amplitude of the solitary structures strongly depends on the size of the potential hill. In addition to that the velocity of the forced dust acoustic wave also decreases with the increase of V_{wg} as shown in Fig. 5.8(b). Hence in our experiments, the solitary wave having higher amplitude propagates with higher velocity which is one of the important properties of a KdV type solitons. Therefore, it can be concluded that the size of the potential hill plays a salient role on the propagation characteristics of a solitary wave.

To model these experimental findings, we have again solved numerically the f-KdV equation (Eq. 5.6) for different values of the amplitude (A_s) and width (G) of the Gaussian source function by choosing the values from the power law relationship derived from the experiments and measured the mean value of the amplitude of solitary structures.

Fig. 5.9 depicts the variation of amplitude of forced solitary waves obtained from numerical solution of f-KdV with the height and width of the source function.

For the present set of numerical simulation, the amplitudes and widths are chosen from the experiments as shown in Fig. 5.6(b). In Fig. 5.9(a) one can see that the amplitude of the excited forced solitary waves decreases with the decrease of amplitude of the source function while it decreases with the increase of width of the source function as shown in Fig. 5.9(b). The first point of Fig. 5.9(a) and last point of Fig. 5.9(b) correspond to a single soliton solution of the equation which is also the threshold conditions for the creation of f-KdV solitons. Further decreasing of A and increasing of G causes only the excitation of wake structures instead of the creation of solitons. Therefore, the findings from the numerical analysis qualitatively support our experimental observations and there is indeed a threshold for the generation of solitons in the f-KdV simulation similar to the experiments.

5.3.4 Effect of shape of charged object on the excitation of precursor solitons

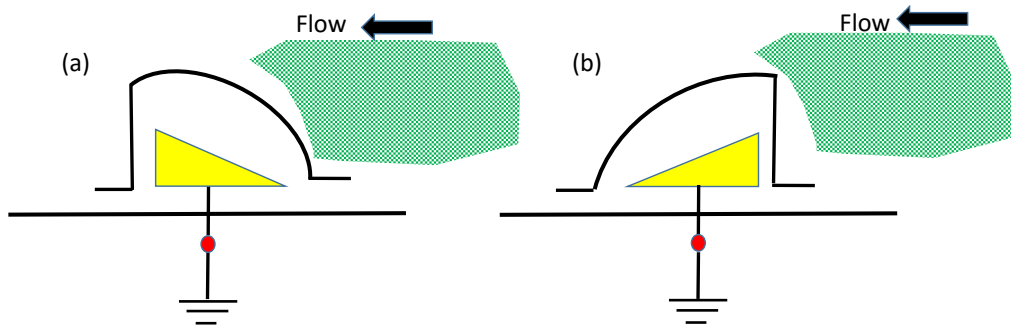


Figure 5.10: Equilibrium configuration of dust cloud before generating the flow for two different shapes of the charged object.

All the above experiments are performed by flowing the dust fluid supersonically over the wire of different sizes (height and width) of the potential hill. As

discussed in Chap. 4, the potential profile around the wire [182] is indeed a Gaussian where the fall of the sheath profile is symmetric and sharp around the object. Next, to investigate the effect of shape of potential profile on the propagation characteristics of forced solitary waves, a triangular shaped object is used in two different configurations as shown in Fig. 5.10(a) and (b). The supersonic flow in the dust fluid is again generated by switching the object from grounded potential to floating potential as described in Fig. 5.2. In the first case (see, Fig. 5.10(a)), the dust fluid flows over the rising slope of the potential profile created by the triangular charged object, whereas in another configuration, dust fluid flows over a steep charged object (see, Fig. 5.10(b)) first and then flows over falling slope. Fig. 5.11(a) shows a typical image of the excited structures when the dust fluid

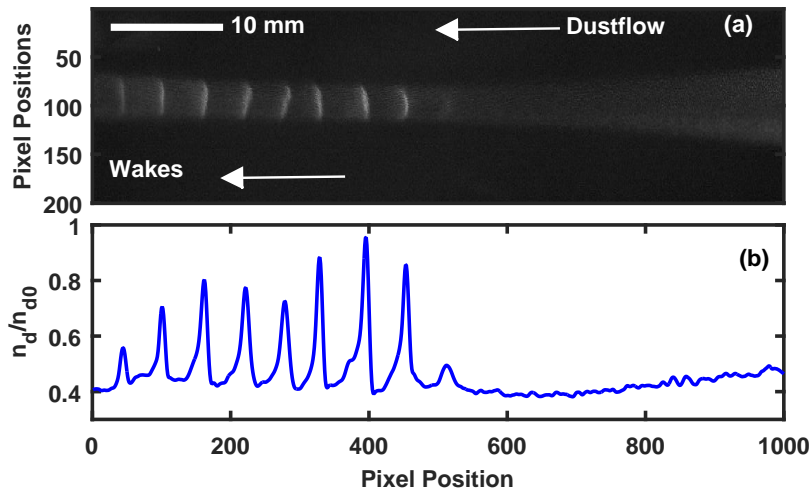


Figure 5.11: (a) Generation of non linear wakes in the direction of flow when the flow is initiated and facing rising slope of the potential hill (b) Intensity profile of Fig. 5.11(a).

supersonically flows over the charged object as shown in Fig. 5.10(a). Interestingly in this configuration, no structures are found to propagate in the upstream direction dissimilar to the case when the object is purely Gaussian (see Fig. 5.4(a)). Instead a series of crests are found to propagate in the down stream direction.

The perturbed dust density profiles (extracted from Fig. 5.11(a)) is plotted in Fig. 5.11(b) to explore the properties of these structures. These smaller amplitude

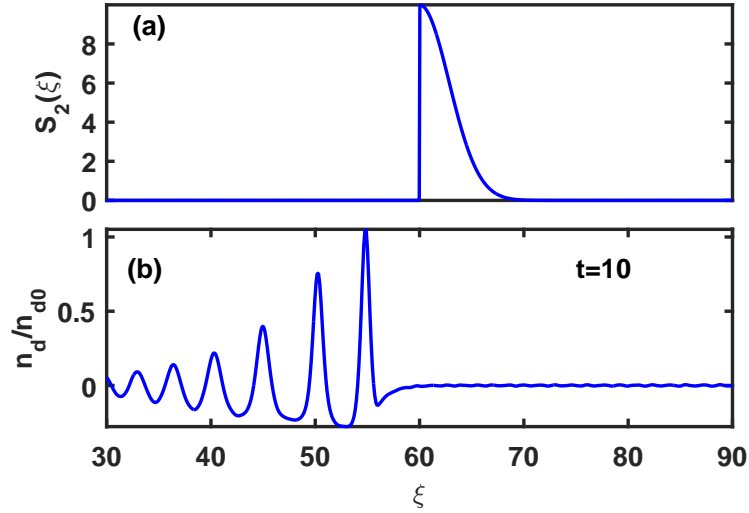


Figure 5.12: Time evolution of numerical solution of f-KdV equation using the source function half Gaussian function as Source function to replicate the triangular shaped object.

crests propagate in the downstream direction with respect to the frame of fluid as wakes. These experimental findings are also compared with numerical solutions of forced-KdV equation (see Eq. 5.6) in which the source function is taken as a half Gaussian with a rising slope as shown in Fig. 5.12(a). In case of the triangular object with flat hypotenuse (Fig. 5.12(a) and Fig. 5.14(a)), the object is replicated by a half Gaussian with a width ($\frac{W}{2} \sim 6$) that is bigger than the source function with a full Gaussian. The choice of the width of the source term is dictated by the size of the sheath that forms around the obstacle. For $p = 11$ Pa and $V = 320$ V the sheath around the grounded wire of 1 mm diameter is ~ 15.5 mm (see first ‘ \star ’ of Fig. 5.6 (a)). For the same discharge condition, the sheath around the triangular charged object (of hypotenuse 65 mm) is ~ 80.5 mm. Hence, $\frac{W}{2}$ for the half Gaussian source function is chosen to be 6 which is approximately 5 times

higher compared to the full Gaussian. Fig. 5.12(b) displays the perturbed dust density profile for a given time when the object moves with supersonic velocity similar to our experimental situation. The solution of f-KdV equation shows only the excitation of wake structures, which propagate in the downstream direction as observed in the experiments.

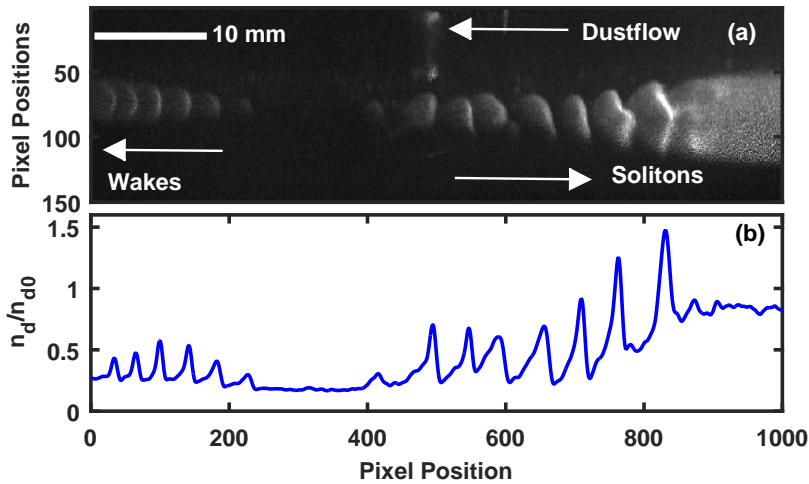


Figure 5.13: (a) Generation of wakes and solitons when the flow faces sharp rise of the potential hill (b) intensity profiles of these wakes and solitons extracted from Fig. 5.13(a).

To investigate further the influence of shapes, the same triangular object is used in reverse configuration as shown in Fig. 5.10(b).

In this configuration, the dust fluid first faces a sharp rise of the potential and then it goes through a monotonic fall in the potential. When the fluid flows supersonically over this object, it excites both precursor solitons in the upstream direction as well as wakes in the downstream direction as shown in Fig. 5.13(a). The perturbed dust density extracted from Fig. 5.13(a) is shown in Fig. 5.13(b). To mimic the experimental observations, the f-KdV equation is again solved numerically by using a half Gaussian object like Fig. 5.12(a) but in the reverse direction as shown in Fig. 5.14(a). The solution of f-KdV also shows the excitation of solitary

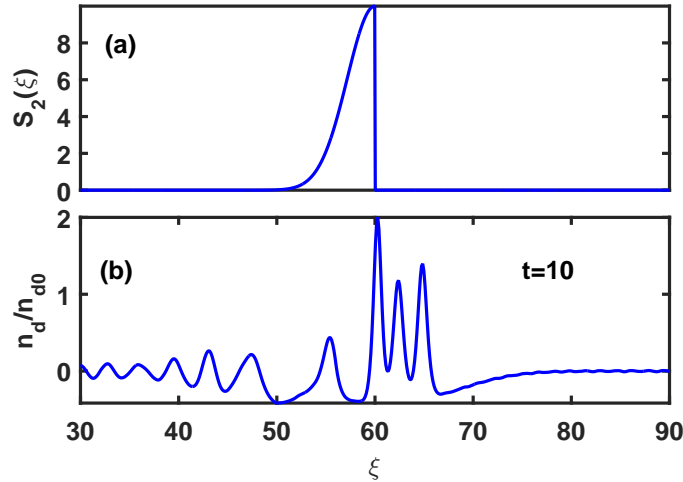


Figure 5.14: (a) Source function (b) Time evolution of numerical solution of f-KdV equation by reversing the source function as shown in Fig. 5.12(a).

waves in the upstream direction and wakes in the downstream direction. Hence, it can be concluded further that the shape of the charged object is also an important parameter which decides the excitation of nonlinear structures. A linear gradient is insufficient to excite the precursor solitons and only gives rise to the customary wakes whereas a sharp gradient excites both.

5.4 Conclusions

A set of experiments are done to investigate in detail the modifications of the propagation characteristics of precursor solitons which get excited when a supersonic flow of dust fluid is made to flow over a stationary charged object of different sizes and shapes. The experiments are performed in the DPEx device in which dusty plasma is created in a DC glow discharge Ar plasma using Kaolin particles. The flow of the dust cloud is initiated by suddenly lowering the height of the potential hill created by a charged object (wire or metallic wedge shaped object). For

the case of subsonic dust fluid flow, only wakes are observed in the downstream direction in the frame of the fluid whereas for a supersonic flow solitary structures are excited in the upstream direction along with the wakes in the downstream direction. The size and shape of the potential profile is varied by connecting a variable resistance in series with a copper wire and by using the triangular object in different orientation with respect to the flow, respectively. The major outcomes of our present work are listed below:

The earlier experiments of Jaiswal *et al.* [48] are repeated to serve as a benchmark. Precursor solitons and wakes are excited by flowing the dust fluid over a charged wire. For the case of subsonic dust fluid flow, only wakes are observed in the downstream direction in the frame of the fluid whereas for a supersonic flow solitary structures are excited in the upstream direction along with the wakes in the downstream direction. The solitary structures are confirmed to have the characteristics of KdV solitons. These observations are then compared with numerical solutions of the forced-KdV (f-KdV) equation by modeling the charged object as a Gaussian source function. The numerical solution of f-KdV equation with the Gaussian object shows the generation of solitonic structures which propagate in the upstream direction whereas the wakes propagate in the downstream direction akin to experimental observation.

To investigate the effect of size of the potential hill on the propagation of precursor solitons, the height of the potential hill is varied by drawing current through a variable resistance. It is found that the amplitude and velocity of the solitons decreased whereas their widths increased with a decrease in the height of potential hill. The number of emitted solitonic structures also decrease with the decrease of the hill height. It is also discovered that there is a threshold height of

the potential hill below which the dust fluid simply flows over the object without exciting any structures.

The f-KdV equation is once again solved numerically by changing the height and width of the Gaussian source function. The numerically obtained amplitudes and widths of solitonic structures follow a similar trend as observed in the experiments.

In another set of experiments, the shape of the potential profiles of the charged object is changed by replacing the wire by a solid triangular shaped object. In this specific set of experiments, the flow is only generated by switching the charged object from ground to floating potential. When the dust fluid flow supersonically over this triangular object facing the linearly increasing slope only wakes are found to be excited in the downstream direction and no nonlinear structures are seen to propagate in the upstream direction. However, when the experiments are carried out by reversing the object so that the dust fluid faced the sharp jump of the potential created by the charged object, both solitons propagating in the upstream direction and wakes propagating in the downstream direction are seen. These results are also modeled and compared qualitatively with the experimental findings by taking the source function to be a half Gaussian in the forward and reverse directions respectively.

Hence, to summarize, the excitation of precursor solitons and their propagation characteristics are found to depend on the shape and size of the potential profiles of the charged object over which the fluid flows. Our experimental findings not only confirm and consolidate earlier experimental observations of precursor solitons but bring to light new fundamental results regarding the excitation process. These insights should prove helpful in interpreting the manifestation of this concept in natural occurrences such as in excitations triggered by solar wind interactions with

the earth and moon or space debris or satellite interactions with the ionospheric plasma. The findings may also stimulate further experimental and theoretical studies towards more fundamental investigations of this yet poorly explored topic in plasma physics.

6

Excitation of pinned solitons

Part of this chapter is submitted in *Phys. Rev. E.*, 2020 by Garima Arora *et al.*.

6.1 Introduction

Solitons are a well known class of stable localized nonlinear structures that have been widely observed and studied in a variety of natural and laboratory settings including ocean waves [183], excitations in optical fibres [184, 185] and semiconductors [186, 187], plasmas systems [30, 31, 80, 84, 88, 188], laser plasma interactions [87, 189, 190], *etc.* A number of model nonlinear evolution equations that are known to be fully integrable yield soliton solutions. The Korteweg-de Vries equation [191–194] is one such nonlinear partial differential equation that has been extensively employed as a model to study low frequency nonlinear wave phenomena in a plasma under conditions of weak dispersion and weak nonlinearity. The

emergent non-linear self-reinforcing wave packets that maintain their shape and identity while propagating at a constant velocity over a large distance are well represented by the exact mathematical soliton solutions of the KdV equation. While the KdV model works well for impulsive excitations of nonlinear pulses where the excitation source provides only an initial perturbation, the model is inadequate to describe experimental situations where the source continues to be operational in a continuous manner. Such is the case for example when a moving object continuously excites waves in a fluid medium. To model such a situation a KdV equation with a driving term - the so called forced-KdV (f-KdV) equation - has been adopted and used successfully in the past to interpret nonlinear phenomena in hydrodynamics e.g. to study nonlinear waves excited by fast moving objects in water [45, 46, 195, 196]. The f-KdV model yields some interesting and novel nonlinear solutions such as precursor solitons that travel ahead of the moving object at a speed faster than the object. These precursors can be excited when the speed of the moving object crosses the sound speed of the medium. The f-KdV model also yields another class of soliton solutions that travel at the same speed as the moving object and remain pinned to the object as an envelope structure. These pinned solitons can be excited at a much higher speed of the object than what is required for the precursor solitons. Precursor solitons in a plasma were recently observed for the first time under controlled laboratory conditions by flowing a dust fluid supersonically over a stationary charged object [48]. In a frame where the fluid is stationary and the object is moving, the solitons were shown to propagate in the upstream direction as precursors while linear wake structures were seen to propagate in the downstream direction [48]. In a subsequent experiment, the propagation characteristics of these nonlinear structures were shown to depend on the

shape and size of the charged object [136] over which the fluid flows. Experimental observations of this fore-wake phenomenon were well explained with the help of the forced KdV model equation [48, 136].

While propagating precursor solitons in plasmas appear to be well established both experimentally and theoretically the topic of pinned solitons has so far not received much attention. The most detailed theoretical study on them over a range of amplitudes, widths and the velocities of the moving charged object has been carried out by Tiwari *et al.* using extensive fluid simulations [50].

This chapter deals with an experimental study on the observation of pinned solitons in a dusty plasma medium. The major difference in the present set of experiments from the past experimental conditions is in the speed of the dust flow which is kept highly supersonic and in the fine tuning of this speed by careful control of the height of the potential barrier created by a biased copper wire placed in the path of the dust flow. The experiments show not only the existence of single humped pinned solitons enveloping the moving source but also multi-humped solutions as predicted in the theoretical studies of Tiwari *et al.* [50]. Our present findings, apart from establishing the experimental existence of these interesting nonlinear structures, should also provide valuable clues for detecting them in natural situations such as in the fore-wake region of the Earth's bow shock where the interaction of the solar wind with the earth can potentially give rise to such structures.

The chapter is organized as follows: In the next section (Sec. 6.2), the experimental set-up and procedure of excitation of pinned solitons along with the wake structures are described. Sec. 6.3 presents the experimental results and discusses the nature and dependence of the pinned solitons as a function of the dust flow

velocity. This section also provides a comparison with theoretical results obtained from a numerical solution of an appropriate f-KdV equation. A brief summary and some concluding remarks are provided in Sec. 6.4.

6.2 Experimental set-up and procedure

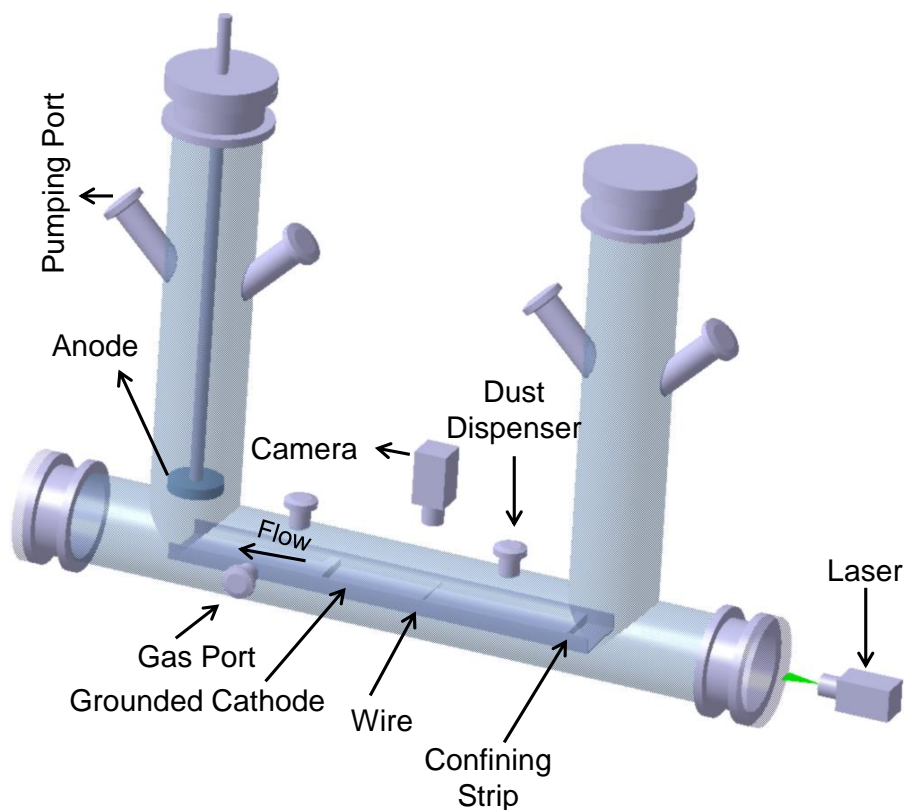


Figure 6.1: A schematic diagram of dusty plasma experimental (DPEX) setup.

Fig. 6.1 shows the schematic diagram of the Dusty Plasma Experimental (DPEX) device in which the experiments have been carried out. It is basically an inverted Π shaped vacuum chamber consisting of a primary cylindrical glass tube which is radially attached with two secondary tubes. There are several radial and axial ports connected with the primary as well secondary chambers to serve various

experimental needs. A disc shaped anode suspended axially from the top of the left secondary chamber and a tray type grounded cathode housed in the primary chamber are used for the production of the plasma. Two confining potential strips are placed on the cathode for confining the dust particles in the axial direction whereas the bent sides of the cathode tray provide radial confinement. A more detailed description of the device along with its associated diagnostics are available in Chap. 2. A biased copper wire of diameter 1 mm and length 50 mm mounted radially on the cathode acts as a stationary charged object for the excitation of pinned structures. The wire can be kept at various potentials ranging from grounded to intermediate as well as at the floating potential by connecting a variable resistor ranging from 10 k Ω – 10 M Ω in series with the wire through a switch. A DC power supply (with a range of 0-1 kV and 0-500 mA) is used to strike the discharge between the electrodes. Micron sized poly-dispersive particles of diameter ranging from 2 to 5 μm are sprinkled on the cathode in between the wire and the right strip for producing a dusty plasma. The average mass of these micron sized dust particles is estimated to be $\sim 8.6 \times 10^{-14}$ kg.

Initially, the chamber is pumped down to a base pressure of 0.1 Pa by fully opening the gate valve attached at the mouth of the pump. The working pressure is set to 9-15 Pa by closing the gate valve to 20% and opening the flow meter attached to the gas port to 5-10 % as shown in Fig. 6.1. An equilibrium pressure inside the chamber is maintained through out the experiments by balancing the pumping rate and the gas flow rate. An Argon plasma is formed between the electrodes by applying a voltage in the range of 290-360 V and the plasma parameters are measured using a single Langmuir probe and an emissive probe over a range of discharge parameters. For the present range of discharge conditions, the plasma

density (n_i) and electron temperature (T_e) come out to be $\sim 0.5-1.5 \times 10^{15}/m^3$ and $2 - 5$ eV, respectively. The profiles of plasma parameters over a wide range of discharge parameters are presented in Chap. 2.

To create a dusty plasma, first the equilibrium pressure $P = 9$ Pa is set by introducing the Ar gas in the chamber and then the applied voltage is increased to 400 V so that a high electric field is created and the particles sprinkled on the cathode get charged. These particles acquire a negative charge in the plasma environment and levitate in the cathode sheath by an exact balance of gravitational and electrostatic forces. The levitated particles are visualised by shining a green laser light and their dynamics are captured by a fast CCD camera looking in the x-z or y-z plane depending upon the experimental requirement. The voltage is then reduced to 300 V at which a highly dense dust cloud is seen in between the grounded wire and the right confining strip. Fig. 6.2(a) shows the y-z plane of the

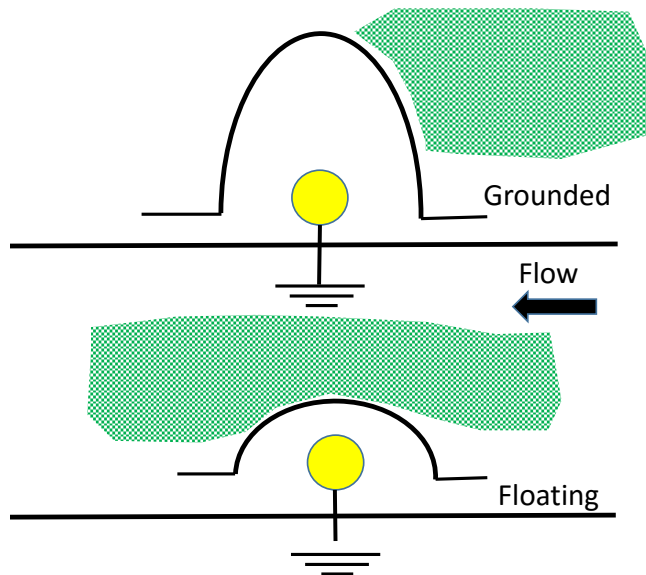


Figure 6.2: (a) Equilibrium configuration of dust cloud before generating the flow. (b) Flow in the dust fluid is initiated from right to left by lowering the potential hill suddenly. The yellow circle represents the location of charged object.

dust fluid, which is confined in between the grounded wire and the right strip. The potential around the grounded wire becomes negative with respect to the surface potential of the dust and as a result the particles remain confined in the potential well created by the wire and the strip and exhibit only thermal motion. The present set of experiments are carried out at a discharge voltage of $V_d = 300$ V and background pressure of 9 Pa. At that discharge condition, the particles are seen to levitate at a height of 2.75 cm from the cathode, which is significantly higher (2.1 cm) compare to the case of our earlier experiments on the excitation of precursor solitons [48,136] in a flowing dusty plasma. That facilitates us to generate a highly supersonic flow, $M(v_f/C_{da}) \sim 1.5 - 3$ in the dust fluid compare to the experiments that we have performed in the past ($M \sim 1.1 - 1.3$).

In addition, as mentioned above, we have performed our experiments at a pressure of 9 pa which is comparatively lower than that of the previous experiments (11–12 Pa). In that pressure regime the dust neutral collision frequency is estimated [62,115] to be 9 s^{-1} , which is almost half (18 s^{-1}) compare to that of the experiments that are carried for the excitation of shock waves reported in Ref. [83]. We choose this lower dust neutral collisional regime so that dissipation becomes less important and hence the possibility of the excitation of shock waves can be avoided. For this specific discharge condition, $n_i \sim 5 \times 10^{14} / \text{m}^3$, $T_e \sim 5$ eV which are measured using a single Langmuir probe. The dust density (n_d) is approximately estimated as $\sim 10^{11} / \text{m}^3$ from the high resolution camera images, whereas the dust temperature (T_d) is estimated by tracking the individual particles of the tail part of the dust cloud for 100 consecutive frames using super Particle Identification Tracking (sPIT) [118] code and comes out to be $T_d \sim 0.6\text{-}1.2$ eV. The charge $Q_d \sim 10^4 e$ is estimated from the Collision Enhanced Plasma Collection [54,55]

(CEC) Model for the present set of discharge conditions. With the help of plasma and dusty plasma parameters, the dust acoustic speed is theoretically estimated to be $C_{da} \sim 22\text{-}25 \text{ mm/s}$ which is in good agreement with earlier measurements of Jaiswal *et al.* [135].

To investigate the propagation characteristics of the nonlinear waves, a highly supersonic flow of the dust fluid ranging from 30 mm/s to 60 mm/s (corresponding to $M=1.5$ to 3) is initiated by altering the confining potential for a particular discharge condition, $p=9 \text{ Pa}$ and $V=300 \text{ V}$. The height of the potential hill is suddenly reduced from grounded potential to an intermediate potential (a potential which is less negative with respect to the surface potential of particle), which generates a flow of the dust fluid from right to left as shown in Fig. 6.2(b). Within a few ms, the dust particles attain a constant velocity due to the neutral drag force [135, 181] and the magnitude of this constant velocity is varied by changing the value of the intermediate potential and it is found that the maximum velocity is achieved when the wire is switched to floating potential. The flow velocity of the dust fluid is estimated using Particle Image Velocimetry (PIV) technique [119]. It is worth mentioning that the same technique of flow generation was used by Jaiswal *et al* [48] to excite precursor solitons in the upstream direction and wakes in downstream direction. In their experiments the range of fluid flow velocity was $M = 1.0 - 1.2$. In the present experiments the fluid velocity is kept higher than these earlier values and the consequent excitations of nonlinear structures studied. The flow technique discussed in Sec. 6.2 is used to generate a flow in the dust fluid with flow velocities ranging from $M \sim 1.5 - 3$ along the axis of the chamber. The initial experiments are carried out by adjusting the resistance value in such a way that the flow velocity of the dust fluid becomes $M \sim 1.5$.

6.3 Results and discussion

6.3.1 Excitation of pinned solitons and wakes

Fig. 6.3(a) shows a snapshot of the wave excitations occurring at this supersonic flow velocity of dust fluid, whereas Fig. 6.3(b) depicts the axial profile of compression factor, which is extracted from Fig. 6.3(a). From Fig. 6.3(a) and Fig. 6.3(b), we see a distinct nonlinear humped structure close to the yellow dashed line which marks the location of the charged object and lower amplitude wake structures to the left of the yellow line. The amplitude (A), width (L) and the parameter (AL^2) of the single humped nonlinear structure are measured for a number of frames and it is found to remain stationary with $A \sim 1.33 \pm 0.07$, $L \sim 0.86 \pm 0.08$ and $AL^2 \sim 0.99 \pm 0.02$ over all these frames. The small values of statistical errors of various parameters essentially confirm that the structure does not change its identity over time. These measurements of solitonic parameters essentially confirm that it has a solitonic character and constitutes a pinned soliton.

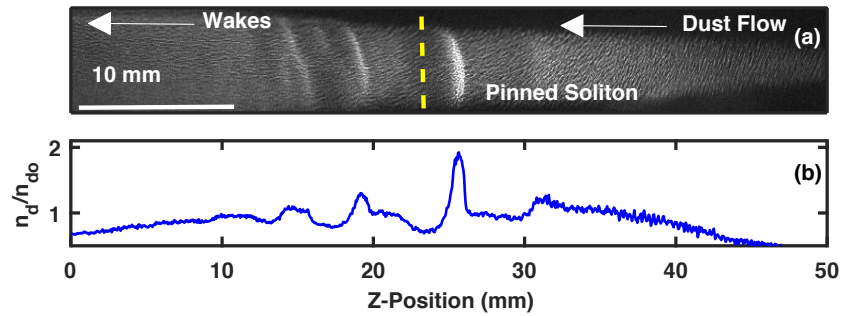


Figure 6.3: (a) A typical experimental image of excitation of single pinned soliton. The dashed vertical line marks the position of the wire. (b) Axial profile of compression factor of density perturbation extracted from 6.3(a).

When the flow velocity of the fluid is increased further to $M = 2.1$ and above, by changing the wire potential under the same discharge conditions, we find a

significant change in the shape of the pinned soliton. As shown in Fig. 6.4 a

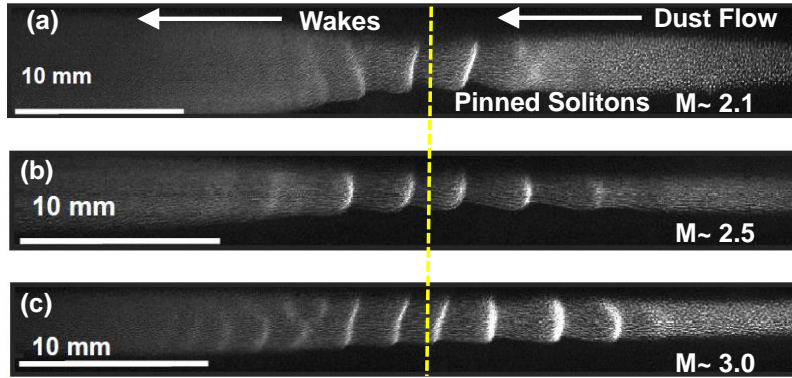


Figure 6.4: Typical images of excitation of (a) double (b) four and (c) many pinned solitons along with the wakes. The yellow dashed line represents the location of the charged object.

variety of multi-humped pinned structures appear for flow velocities $M = 2.1$, 2.5 and 3.0 respectively. Fig. 6.4(a)-(c) clearly shows that the number of humps increases with an increase in the flow velocity. The corresponding intensity profiles of the structures of Fig. 6.4(a)-(c) are plotted in Fig. 6.5(a)-(c). Fig. 6.5(a) shows the profile of a fully developed two humped pinned soliton that remains stationary in the laboratory frame and Fig. 6.5(b) shows the profile for a similar four peaked pinned soliton. It is to be noted that the two and four peaked structures have a symmetric profile around the wire. Interestingly, in the case of $M \sim 3.0$ (see Fig. 6.5(c)), the multi-humped pinned soliton has an asymmetric structure with respect to the wire with the peaks to the right having a higher amplitude compared to the ones at the left. The characteristics of the wakes however remain the same with the increase of flow velocity and are always found to propagate in the direction of flow or in the downstream direction in the frame of the fluid.

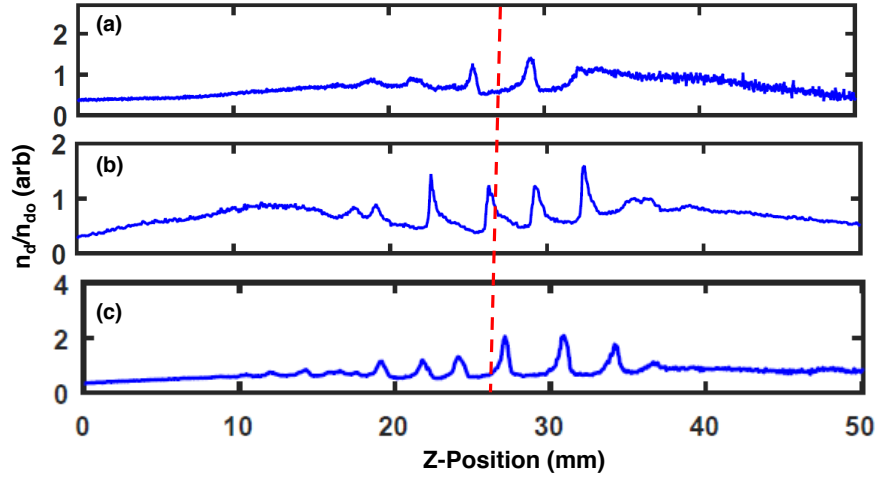


Figure 6.5: Density compression factor of (a) two, (b) four and (c) many sharp peaks extracted from Fig. 6.4(a), (b) and (c). The dashed line represents the location of the wire.

6.3.2 Time evolution of the pinned solitons and wakes

The time evolution of three such solitons (as captured from subsequent frames) for the case of $M = 2.3$ is plotted in Fig. 6.6(a) where the high amplitude structures in the figure represent the solitons whereas the lower amplitude structures on the left are wakes.

Fig. 6.6(a) also shows that the soliton remains nearly stationary in their positions in the laboratory frame of reference as of stationary charged object. In the frame of the fluid, the charged object moves from left to right along with the pinned solitons with the same velocity. The wake structures however are not stationary and propagate in the downstream direction as has been observed earlier in the experiments of Jaiswal *et al.* [48] and also shown in Fig. 6.6(b), which is a zoomed version of Fig. 6.6(a) with only the wakes. To summarize, the highly supersonic fluid flow over a stationary charged object excites non-linear pinned solitons in an upstream direction which maintain their shape and size in the course of time,

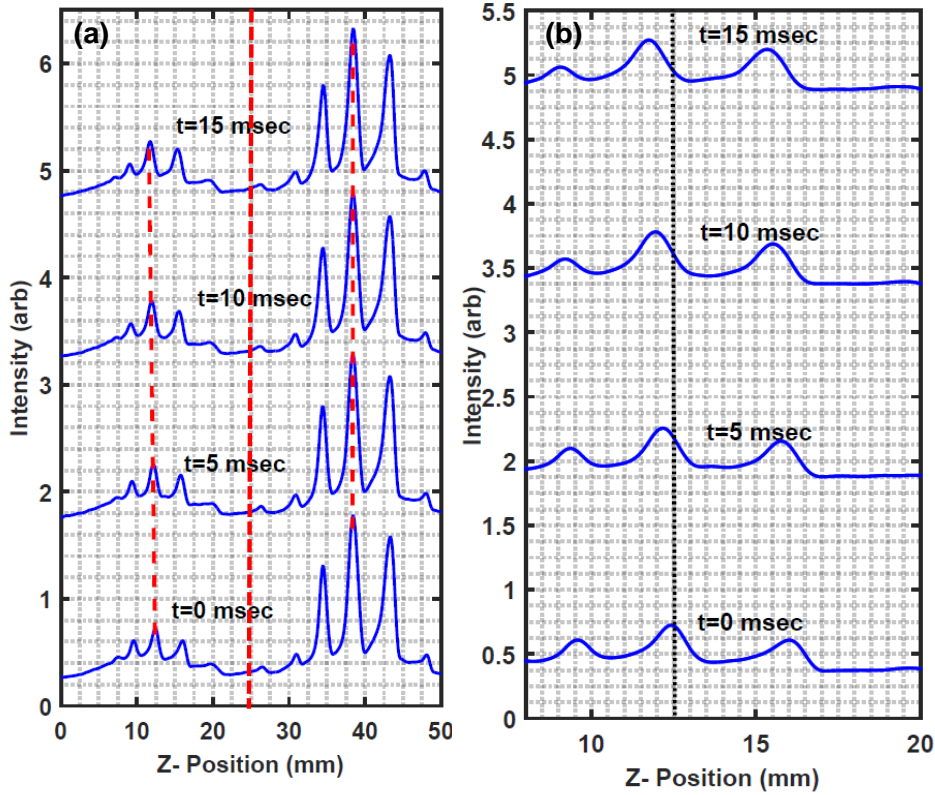


Figure 6.6: (a) Intensity profile of pinned solitons and wakes over time. The dashed lines show that the higher amplitude solitons remain stationary in the laboratory frame, whereas the wakes move along the flow. (b) The zoomed version of Fig. 6.6(a), which clearly shows that the wakes move from right to left.

whereas the wakes propagate in the downstream direction.

To quantify the dependence of the amplitude on the flow velocity the maximum values of the amplitudes of the solitons excited in the range of $M=1.5$ to 3 are plotted against the Mach number in Fig. 6.7. It can be seen that with an increase in M , the maximum amplitude of the excited stationary structures increases. This is in qualitative agreement with the scaling observed in the fluid simulations of pinned solitons carried out by Tiwari *et al.* [50].

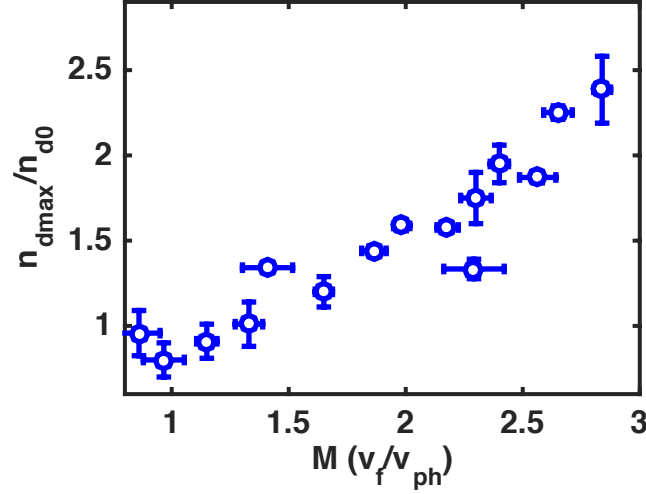


Figure 6.7: Variation of maximum density compression n_{dmax}/n_{d0} with the normalized flow velocity M .

6.3.3 Comparison with model f-KdV equation

For a further qualitative understanding of the experimental results we have solved the f-KdV equation numerically with a Gaussian source term [49] and compared the numerical results with our experimental observations. The detailed derivation of f-KdV equations and its solution is discussed in Chap. 5. The f-KdV equation for a dusty plasma is given by

$$\frac{\partial n_{d1}}{\partial \tau} + An_{d1} \frac{\partial n_{d1}}{\partial \xi} + \frac{1}{2} \frac{\partial^3 n_{d1}}{\partial \xi^3} = \frac{1}{2} \frac{\partial S_2}{\partial \xi}, \quad (6.1)$$

where S_2 represents the source term, n_{d1} is the perturbed dust density normalized to the equilibrium density n_{d0} and $\xi = (z - u_{ph}t)$ is the coordinate in the wave frame moving at phase velocity u_{ph} normalized to the dust acoustic speed. The spatial coordinate z is normalized by the dust Debye length (λ_D) whereas the time is normalized by the inverse of dust plasma frequency (ω_{pd}). The coefficient $A = [\delta^2 + (3\delta + \sigma_i)\sigma_i + \frac{1}{2}\delta(1 + \sigma_i^2)]/(\delta - 1)^2$, where δ and σ are the ratio of ion to

electron density and temperature, respectively. A Gaussian source function is used in the form $S_2(\xi + Ft) = A_s \exp(-(\xi + Ft)/G)^2$ where, A_s and G are the amplitude and width of the source function and $F = 1 - v_d$, with v_d the velocity of source function with respect to the frame of fluid. The pinned solitons are numerically obtained by solving Eq. 6.1 for a Gaussian source with $A_s = 5.5$, $G = 15$ that is made to move with $v_d = 2.0$ in accordance with the experimental condition of $M = 2$.

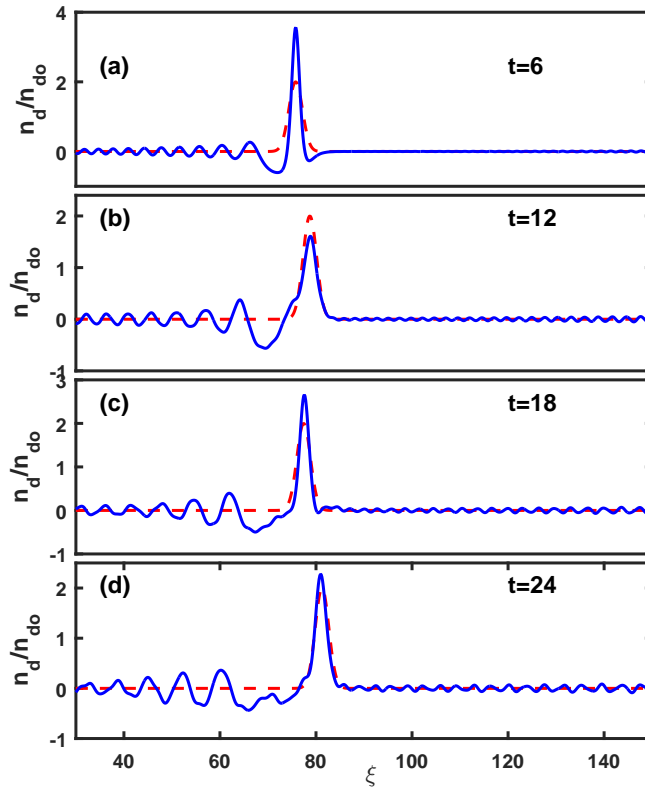


Figure 6.8: Time evolution of pinned solitons (solid lines) as well as a source function (dashed lines) obtained numerically by solving the f-KdV equation.

The time evolution of S_2 and the normalized perturbed dust density n_d/n_{d0} is shown in Fig. 6.8(a)-(d) for $t = 6, 12, 18, 24$, respectively. The red dashed lines in Fig. 6.8 represents the position of the charged object that moves with supersonic

velocity in the fluid frame. The blue solid lines represent the numerical solution of the f-KdV. As can be seen, similar to the experimental results (see Fig. 6.3(b)), a single peaked structure representing a single humped pinned soliton is created near the source and remains stationary with respect to it. The structures to the left of the object consisting of wakes are seen to travel to the left. For further comparisons with the experiment, Eq. 6.1 is solved for different values of the amplitude, width and speed v_d of the source term to investigate the dependence of the nature of the pinned solitons on the source parameters. In the experiments the change in the velocity of the source is brought about by a change in the amplitude and width of the source e.g. the velocity of the source function is increased by increasing its amplitude which in turn increased the width. Keeping that in mind we have changed the amplitude, width and the velocity v_d in the source and then solved the f-KdV equation. The results are shown in Fig. 6.9(a-c) for source parameters with $A_s = 2, 4, 6$, $G = 2, 8, 20$ and $v_d = 1.2, 1.5, 2.2$, respectively at $t = 24$. The solid lines correspond to the stationary structures excited by the respective moving source objects and the dashed line indicates the position of the source. Similar to the experiments, it can be seen that with an increase in the velocity (v_d) of the source functions, the number of peaks of excited pinned soliton increases as does the value of the maximum amplitude. This is once again in conformity with the fluid simulation results of Tiwari *et al.* [50] where they had found that the amplitude as well as the number of modulation peaks of the excited pinned solitons increased with the increase in the source velocity and amplitude.

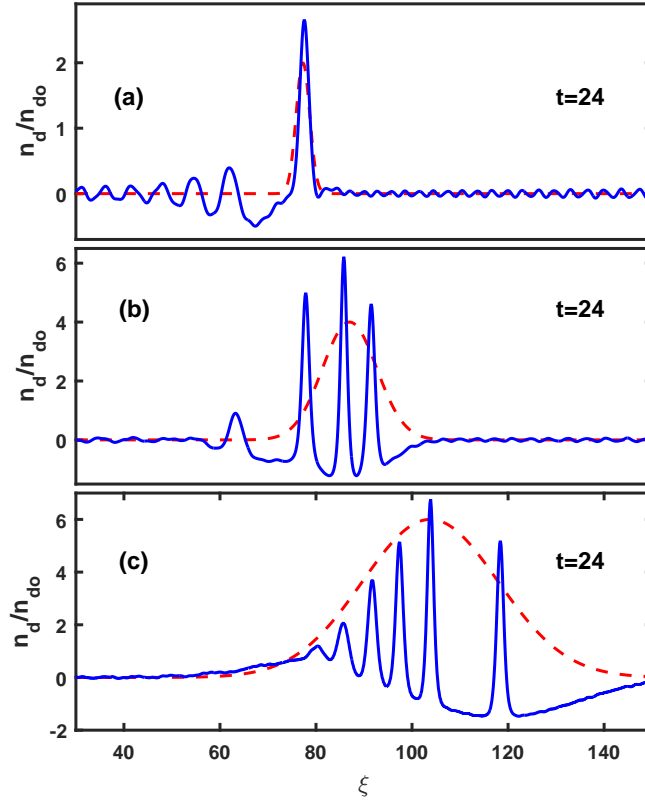


Figure 6.9: A plot for one, three, many pinned solitons (represented by solid line) from the numerical solutions of forced KdV equation for three different amplitude, width and velocity of source functions for $t=24$. Dashed lines represent the source functions.

6.4 Conclusions

To conclude, experimental observations of a new class of stationary solitons, known as pinned solitons, is presented in this chapter. These experiments have been performed in the Dusty Plasma Experimental Device in which a large dust cloud is created in a DC glow discharge Argon plasma. For the purpose of generating a highly supersonic flow in the dust fluid, the discharge voltage and the background pressure are set such that the dust particles levitated at a height far above the cathode. The flow in the dust fluid is generated over the stationary charged object

by changing the height of the potential hill used for the axial confinement. The highly supersonic flow of dust fluid is seen to generate multiple nonlinear stationary structures in the vicinity of the wire. In the frame of the moving fluid, these structures would remain attached to the moving object (wire) and would constitute propagating pinned solitons. The maximum amplitude of the solitonic structures is found to display a nearly parabolic increase with the increase of the fluid flow velocity. In addition, the number of amplitude modulations (peaks) in the density perturbation is also found to increase with the increase in the dust flow velocity. The results are in qualitative agreement with numerical solutions of the forced-KdV equation with a Gaussian source function moving with supersonic velocity. The experimental and numerical results are also in good agreement with past fluid simulation results of Tiwari *et al.* [50]. Our experimental results apart from establishing the first ever existence of pinned solitons in a plasma medium may also prove useful in the detection and interpretation of similar structures that can potentially arise in natural conditions such as in the vicinity of the Earth's bow shock due to the interaction of the supersonic component of the solar wind with the earth or in the ionosphere due to the interaction of fast moving charged space debris objects with the ambient plasma.

7

Excitation of shock waves in an inhomogeneous dusty plasma

Part of this chapter is published in *Phys. Plasmas*, **27**,083703 (2020) by Garima Arora *et al.*.

7.1 Introduction

During the past couple of decades, a dusty plasma, provides an excellent medium for the study of collective phenomena as it supports a wide variety of linear and nonlinear waves and coherent structures. Various extensive theoretical and experimental studies have been carried out on the excitation of linear modes like

Dust Acoustic (DA) Waves [25], Dust Ion Acoustic (DIA) waves [28], Dust Lattice (DL) Waves [73], non-linear modes like Dust Solitary (DS) waves [31, 47, 197], Dust Acoustic Shock (DAS) Waves [81–83] and various coherent structures like voids [35], vortices [198] *etc.*. Dust Acoustic Shock Waves (DASW) [81, 82, 199] constitute an important class of non-linear waves that are frequently found to be excited in laboratory dusty plasmas as well as in astrophysical dusty plasmas [200–202]. Shock waves are highly non-linear structures, which form with a characteristic sudden jump in any one of the physical parameters such as pressure, velocity, temperature and density. These nonlinear waves get excited when the dissipation (due to collisions or viscosity) in the medium plays a significant role along with non-linearity and dispersion. In dusty plasmas, dissipation can arise either from frequent dust-neutral collisions or dust-dust coupling effects. In a weakly coupled dusty plasma, the dissipation comes primarily from the kinematic viscosity due to frequent dust-neutral collisions and/or dust charge fluctuations, whereas for a strongly coupled dusty plasma the bulk and shear viscosity play a crucial role in providing dissipation.

Dust acoustic shock waves have been studied extensively by many researchers worldwide both theoretically [33] and experimentally [81, 82, 199]. Samsonov *et al.* reported shock formation in an RF produced 3D complex plasma under microgravity conditions in the PKE-Nefedov device [32]. Heinrich *et al.* [82] observed self-excited dust acoustic shock waves in a direct current glow discharge dusty plasma that was generated when the dust cloud went through two slits. Nakamura *et al.* [81] and Jaiswal *et al.* [83] reported experimental observations of bow shock and oscillatory shock structures, respectively, in flowing dusty plasmas when the dust fluid was made to flow supersonically around a stationary charged object.

It is to be noted that all these experiments were carried out in a homogeneous dusty plasma medium. However, in an experimental situation, the presence of density inhomogeneity is likely to be significant when one performs experiments in a large sized dusty plasma medium. In the literature there exist a very limited number of theoretical works devoted to the study of shock waves propagating in an inhomogeneous plasma medium [91,92]. They show that due to the presence of inhomogeneities in the plasma density, the relationships between amplitude, width and Mach number of shock waves deviate significantly from those obtained in a homogeneous medium.

Tadsen *et al.* [203] performed experiments to investigate the dependence of the amplitude of spontaneously excited dust acoustic waves in an inhomogeneous plasma having spatial variations of dust charge, ion density, and dust density. To the best of our knowledge, no experiments have been done so far to examine the nature of propagation of dust acoustic shock waves in an inhomogeneous medium. To the best of our knowledge, no experiments have been done so far to examine the nature of propagation of a dust acoustic shock wave in an inhomogeneous medium.

In this chapter, first such experimental investigation to observe the temporal behavior of dust acoustic shock waves as they propagate in an inhomogeneous dusty plasma medium is presented. The experimental results show that the amplitude and width of these shock structures increase when they propagate down a decreasing density profile of the dusty plasma medium. The increase is inversely proportional to the decrease in the background density in a fractional power law manner. We provide a qualitative theoretical understanding of the experimental results by constructing a modified-KdV-Burger model equation that includes dissipation effects arising from both dust neutral collisions and dust-dust coupling

induced viscosity.

The chapter is organized as follows: In Sec. 7.2 the experimental set-up and details of the experimental procedure are described. The details of the creation of dust density gradient is described in Sec. 7.3. Sec. 7.5 contains the experimental findings and a brief discussion. A theoretical model to describe the experiments are discussed in Sec. 7.6. Sec. 7.7 provides a summary and concluding remarks.

7.2 Experimental set-up and procedure

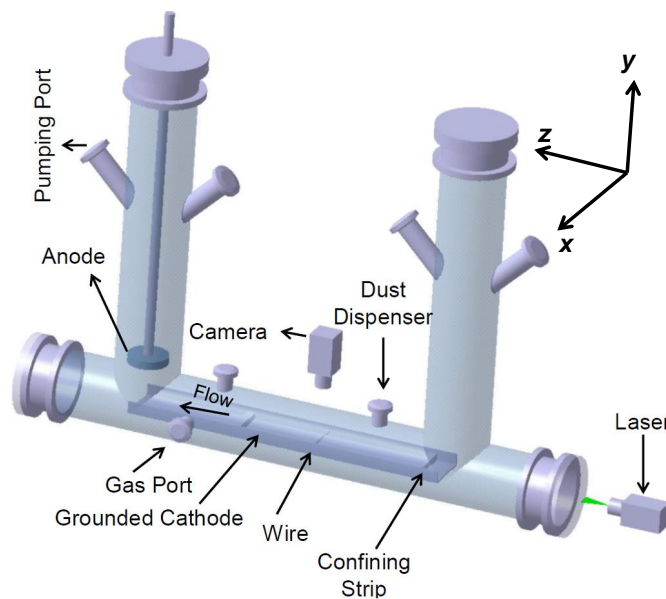


Figure 7.1: A schematic diagram of dusty plasma experimental (DPEX) device.

These experiments are performed in inverted II-shaped Dusty Plasma Experimental (DPEX) Device as discussed in Chap. 2. Figure 7.1 gives a schematic of the DPEX device showing the various radial and axial ports that are used for different experimental needs. The pumping port attached with rotary pump through a gate valve is used to evacuate the chamber whereas the gas port is connected with a flow

meter to feed Argon gas into the vessel in a controlled way. A disc shaped anode and a tray shaped grounded cathode serve as electrodes for the generation of a plasma whereas micron sized poly-dispersive particles of diameter 2-5 μm are used to create a dusty plasma. Two SS cuboid-shaped strips are placed on the cathode in order to confine the charged dust particles in the axial direction. One of these axial confinement strips is kept at the right edge of the cathode whereas the other one is placed at a distance of 28 cm from the first one. The upturned sides of the 6 cm wide cathode tray provide radial confinement. A biased copper wire is mounted radially on the cathode (approximately 20 cm away from the right edge of the cathode) to confine the dust particles axially between the right confining strip and the wire. For a more detailed description of the device and the attached diagnostics the reader is directed to Chap. 2. In the present set of experiments, the copper wire is always kept at the ground potential. A Direct Current (DC) power supply is used for the production of a glow discharge Argon plasma.

To start with, the chamber is evacuated with the help of the rotary pump to attain a base pressure of $p \sim 0.1$ Pa and later the working pressure is set to $p \sim 11$ Pa by adjusting the dynamic equilibrium of the pumping speed and the gas flow rate. In this configuration, the gate valve is opened at $\sim 20\%$ whereas the gas flow meter is opened at 5% . An Argon discharge plasma is then initiated by applying a DC voltage $V_d \sim 330$ V at this working pressure. Plasma parameters such as plasma density (n_i) $\sim 1.5 \times 10^{15} /m^3$, electron temperature (T_e) ~ 4 eV, floating potential (V_f) ~ 290 V and plasma potential (V_p) ~ 310 V with respect to the grounded wire are measured, in the absence of dust particles, by using a single Langmuir probe and emissive probe. The measurement techniques and the axial profiles of different plasma parameters over the range of discharge conditions

are presented in detail in Ref. [115]. As soon as the plasma is initiated, the dust particles of radius (r_d) $\sim 1 - 2.5 \mu\text{m}$ that are sprinkled on the cathode tray prior to the discharge, get negatively charged and levitate in the cathode sheath region by a balance of the sheath electrostatic force and gravitational force in the vertical direction. The vertical height of the cloud bottom varies in the range of 1.3 cm to 1.7 cm depending on the discharge conditions, whereas the vertical width of the cloud is always between 1 cm to 1.2 cm. The average mass of the levitated dust particles is $m_d \sim 8.8 \times 10^{-14}$ kg and the charge (Q_d) acquired by these micro particles at this discharge condition is $\sim 10^4 e$ estimated from a Collision Enhanced Plasma Collection (CEC) model [54, 55] for particles of average radius $2.0 \mu\text{m}$ as discussed in Chap. 2.6.2. A perfectly aligned parallel thin laser sheet (in x-z plane) of width 1 mm illuminates a central slice of the dust cloud consisting of particles of the same size for a given set of discharge conditions. The dynamics of the dust particles are captured by a fast CCD camera having a frame rate of 200 frames/s with a spatial resolution of $42 \mu\text{m}/\text{pixel}$.

7.3 Creation of an inhomogeneous dusty plasma

Since, these experiments are aimed at investigating the propagation characteristics of non-linear waves in an inhomogeneous dusty plasma, we adopt the following sequence of procedures. First a uniform dusty plasma is created between the sheaths of the grounded wire and the right confinement strip by maintaining a dynamic equilibrium of the pumping speed and the gas feeding rate. We then alter this equilibrium by changing the pumping speed to create a pressure gradient. This causes a neutral flow towards the grounded wire and a concomitant flow of the dust particles due to the neutral drag force [137, 181] leading to an accumulation of the

dust particles near the wire. Thus a second dynamic equilibrium state is reached that is maintained by the pressure gradient and the electrostatic repulsion of the sheath around the wire. The whole cloud is still confined between the wire and the right strip due to the sheaths at the two ends but now has a nonuniform distribution of particles. Fig. 7.2(a) displays such a dynamic equilibrium state of the dust cloud

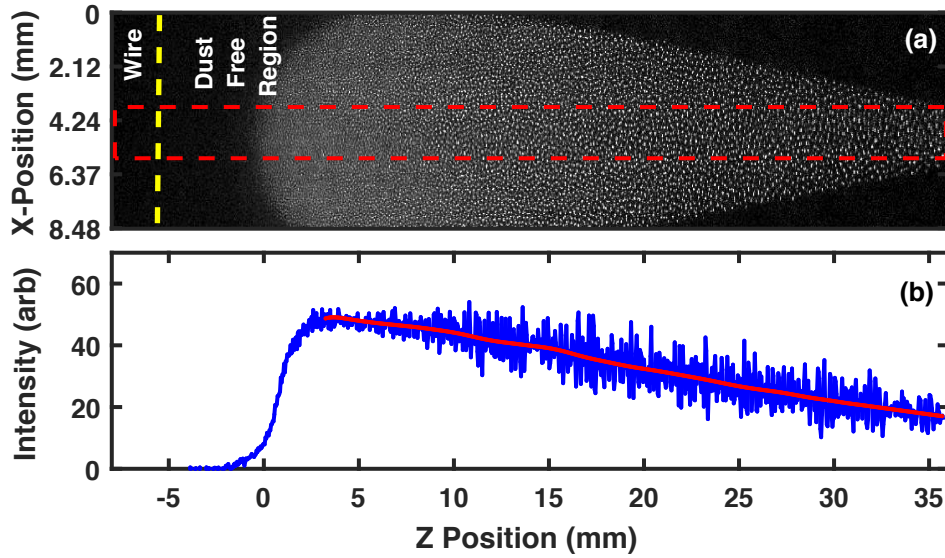


Figure 7.2: (a) An experimental image of equilibrium dust cloud with linear decreasing dust density. (b) Intensity profile extracted from Fig. 7.2 (a).

with a clear indication of the dust density gradient, where the number of particles are more near the grounded wire and less towards the edge of the cathode. It is to be noted that the dust density is inferred from the pixel intensities of an image even in the case of polydisperse particles, provided the size of the dust particles in a particular layer remains the same. This is a standard technique used in the past by several researchers [82, 126, 204]. As mentioned in Sec. 7.2, the particles of same size from the range of polydisperse particles levitate in the particular layer by the balance of gravitation force and the cathode sheath electric force. As we are shining the laser in a particular x-z plane by keeping y-position fixed, it essentially

means that we are capturing the scattered light mostly from monodisperse particles that exist in a particular layer. In Fig. 7.2(a) the dust cloud near the wire is not constituted of smaller dust particles; instead, the number of particles (of the same size) per unit volume is maximum there. Due to the higher dust density in that region, the camera is unable to identify them as separate particles.

The intensity profile of equilibrium dust cloud and the corresponding fitted curve is shown in Fig. 7.2(b). The pixel intensity in Fig. 7.2(b) is plotted by averaging the intensities of 50 pixels in the vertical direction. The area for which the average intensity is calculated is shown by a dashed rectangle in Fig. 7.2(a). This rectangle essentially shows that all the dark spaces (outside the rectangle) of the image does not contribute to the calculation of average pixel intensity. The region of interest is fitted by the solid line in Fig. 7.2(b), where the intensity decreases monotonically if one goes to the right away from the wire. It is worth mentioning that the laser light is kept perfectly parallel to the cathode so that the light scattered from dust particles is not re-scattered from the other plane of the dust cloud. We have taken care that the camera is not being saturated while capturing the images of the equilibrium dust cloud and the excitations of dust acoustic shock waves. We have also verified that the image intensity is linear with dust number density by checking that the camera has a linear response with no offset. The equilibrium spatial density profile is constructed with the help of the intensity profile shown in Fig. 7.2(b) and few measurements of dust density in the tail part of the dust cloud ($z \sim 18 - 32$ mm). The particles are well resolved in this spatial region, which allows us to measure the dust density (see the closed circles in Fig. 7.3). Dust density ($n_{do} = 3/4\pi d^3$) is estimated from the information of inter-particle distance (d) which is defined as the average distance from the reference

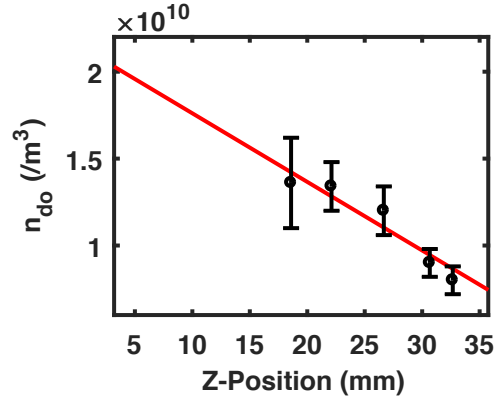


Figure 7.3: Equilibrium dust density extracted from the intensity profile as shown in Fig. 7.2 and few measurements of dust density (closed circles) at z 18–32 mm.

particle to the neighboring particles. We have selected a reference particle at a particular axial location and measured the distance to all its neighboring particles and calculated the average value. To improve the statistics in the measurements, again a new reference particle is chosen at the same axial location but a different x position, and the same procedure is performed to get the statistical mean and standard deviation. The statistical error on the measurements of the dust density at the axial location 18–26 mm are quite high since the resolution is very poor. By assuming the linear response of the camera and using the measured values of dust density near $z \sim 18 - 32$ mm, the intensity profile (solid line of Fig. 7.2(b)) is then calibrated to dust density profile (see the solid line in Fig. 7.3) in the region where the light intensity decreases linearly. As shown in Fig. 7.3, the equilibrium dust density falls nearly monotonically from $\sim 2 \times 10^{10} / \text{m}^3$ to $\sim 0.7 \times 10^9 / \text{m}^3$.

7.4 Excitation of Dust Acoustic Shock Waves

The shock waves are then excited in this nonuniform dusty plasma medium by creating a sudden jump in the dust density. The compression in the dust density

near the grounded wire is generated by flowing the dust fluid from right to left using a Single Gas Injection (SGI) technique. In this technique, the dynamic equilibrium is further perturbed by a short pressure pulse to excite the dust density waves. The pressure pulse is generated by tweaking the gas flow at the Gas Port (as shown in Fig. 7.1) for a short interval (~ 500 ms). Due to the abrupt pressure drop near the gas port, the neutrals rush axially towards the pump and carry the dust particles along from right to left. When the gas flow rate is restored to its initial value the dust particles come back to their original positions. The details of this technique of flow generation in the dust fluid and measurements of the flow velocity are available in greater detail in Chap. 2.7 and 2.8. In case of smaller change in the gas flow rate, the dust particles move slowly towards the pump and stop far away from the wire. When the change in the gas flow rate is sufficiently high, the dust particles simply overcome the potential barrier created by the wire. Details of such a study of the dust dynamics can be found in in Chap. 3. If the gas flow rate is moderately high so that the dust particles cannot overcome the barrier but instead start accumulating near the wire then that creates a sudden jump in dust density. As discussed above, when the gas flow rate is restored to its initial value, the dust particles come back to their initial positions and the dust cloud takes the original shape. The short intense density perturbation gives rise to a large amplitude propagating dust acoustic wave which takes the form of a nonlinear propagating wave train of shock structures - an asymmetric waveform of connected saw-teeth structures [205]. The wave forms propagate an average distance of 30-40 mm in the course of the average time of 0.20-0.35 s with a velocity ranging from 5-12 cm/s depending upon their amplitude and width. For the present set of discharge conditions, the dust neutral collision frequency (ν_{dn}) comes out to be ~ 11 Hz [62], whereas the wave frequency of linear

dust acoustic waves is measured to be ~ 21 Hz. However, it is to be noted that the wave is sustained for approximately 1.5 to 2 s after the initial excitation by the gas which is almost one order higher than the damping time ($2/\nu_{dn}$) ~ 180 ms, for a linear wave. Partly this is due to the nonlinear nature of these waves and the growth they experience as they travel down the density gradient but could also be possibly due to the additional energy drive from streaming ions present in the experiment. The details of these excited nonlinear structures and their propagation characteristics in the in-homogeneous dust density are discussed in Sec. 7.5.

7.5 Experimental Results

7.5.1 Characterisation of Dust Acoustic Shock Waves

A typical snapshot image of the series of excited Dust Acoustic Shock Waves (DASWs) in an inhomogeneous dusty plasma is shown in Fig. 7.4(a), whereas Fig. 7.4(b) represents the corresponding intensity profiles of the density crests of DASWs. One can see clearly from both the subplots that these structures have different amplitudes and widths at different axial locations (along the Z-direction). In addition, it can also be seen that the distance between the crests of the structures keeps on increasing as one moves away from the wire. The sharpness of the peaks, the high compression factor, the saw-teeth nature of their individual density profiles and their high propagation speeds ($\sim 5 - 12$ cm/s) compared to the dust acoustic speed ($\sim 1.5 - 3.5$ cm/sec) indicate that these structures are indeed non-linear shock formations. To examine the symmetry of the wavefronts, we have calculated a symmetric parameter, defined as the ratio (R) of the half widths at half maximum. We have chosen five wave fronts widely separated and located at

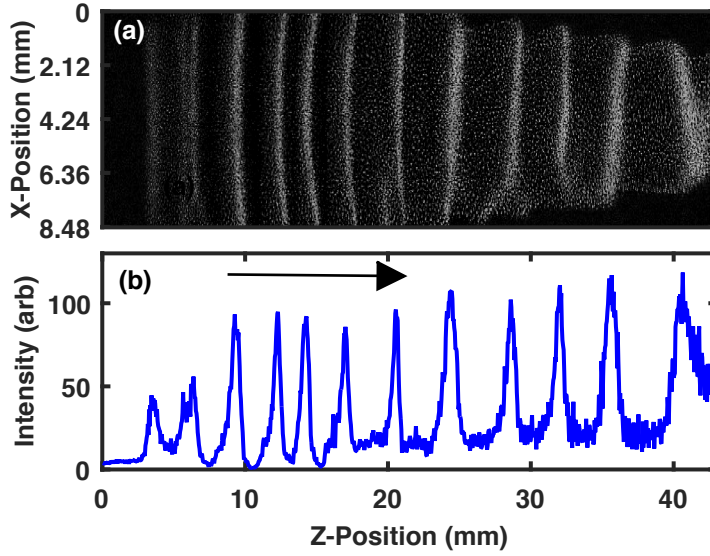


Figure 7.4: (a) Experimental image of density crests in an inhomogeneous dust cloud. (b) Intensity profile of high amplitude density crests extracted from Fig. 7.4(a). The arrow represents the direction of propagation of the shock fronts.

a different axial location for a given frame and then estimate R for these wave-fronts for 20 frames. For our experimental wave forms, the value of R comes out to be $\sim 1.204-1.402$, whereas its value varies within $\sim 0.912-1.024$ for the case of linear dust acoustic waves [206] and $\sim 0.954-1.006$ for the case of non-linear dust acoustic waves [126,207]. In contrast to these linear and nonlinear waves, the value of R for dust acoustic shock waves yields a higher value of $R \sim 1.62 - 2.05$ over time [82]. It essentially ensures that the structures excited in our experiments are indeed asymmetric in shape and significantly deviate from the conventional symmetrical structures observed in the excitation of linear or nonlinear dust acoustic waves like solitons and cnoidal waves. These nonlinear dust acoustic saw-teeth structures are formed due to a sudden change in the dust density near the wire.

They actually constitute a nonlinear traveling wave with steepened crests - in other words a wave train with saw-teeth shaped periodic (shock [205]) structures.

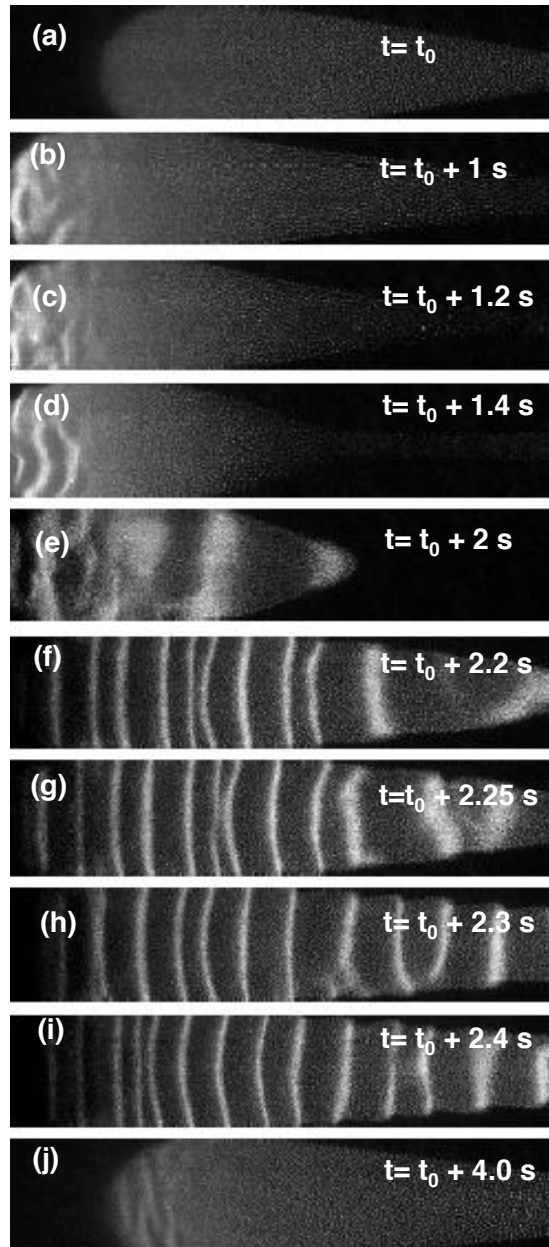


Figure 7.5: Sequence of images: (a) Stable unperturbed inhomogeneous dust cloud, (b–e) spontaneously excited dust acoustic waves in the compressed dust cloud, (f–i) excitation and propagation of nonlinear shock waves. (j) image of dust cloud when the gas flow rate is restored.

This is the nonlinear state of a dust acoustic plane wave excited by the perturbation induced by the act of density compression near the wire and its subsequent relaxation. The sequence of events is as follows (see Fig. 7.5): In the initial stage (depicted in Fig. 7.5(a)) when the inhomogeneous dust cloud is not perturbed there is no spontaneous excitation of any dust acoustic waves (DAWs). Fig. 7.5(b)–(e) show that the DAW excitation occurs after the dust density is momentarily compressed near the wire to create a large density perturbation and as this perturbation moves down the density gradient. Once excited the nonlinear DAW continues to be generated and to travel from left to right at a speed a few times larger than the dust acoustic speed as shown in Fig. 7.5(f)–(i). Fig. 7.5(j) shows that the dust cloud takes approximately its original shape and position (other than the excitations) when the gas flow rate is restored. We do not fully understand what causes the continuous generation of the wave after the initial perturbation ceases but we do observe them experimentally for a long time. A possible continuous driver of these waves could be the ion streaming which is always present in our experiment [208] because of asymmetric configuration of the electrodes. The streaming of ions can be the energy source sustaining the nonlinear wave propagation once the pressure perturbation has initiated the large amplitude DAW. It is worth mentioning that these nonlinear structures are not solitary waves as they do not maintain a constant solitonic parameter ($Amplitude \times Width^2$) over time as seen in earlier experiments of Samsonov *et al.* [31]. Instead, one can see from Fig. 7.4(a) and (b) that the higher amplitude density crests get excited with higher width, which clearly show that these excited structures are not Dust Acoustics Solitary Waves.

7.5.2 Merging of two shock fronts

We have next carried out an experiment to study the merging of two such wave fronts are carried out in a homogeneous dusty plasma. Fig. 7.6 shows one of the events where the merging of two shock structures are presented. The higher amplitude crest propagates from behind with a velocity, $v_s \sim 70$ mm/s and collides with a crest of lower amplitude propagating with a velocity, $v_s \sim 40$ mm/s at $t=40$ ms which are then merged and move together. Interestingly, the newly

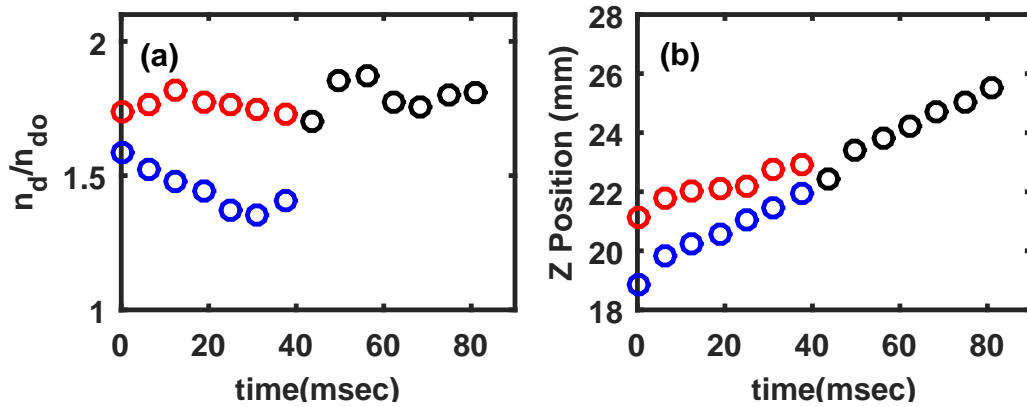


Figure 7.6: (a) Amplitude and (b) Space time graph of two colliding non-linear waves.

formed crest moves with a higher amplitude and greater velocity $v_s \sim 75$ mm/s with respect to the original two colliding crests as shown in Fig. 7.6(a). Figure 7.6(b) displays the space-time plot of these two colliding waves, which also depicts the merging of these two density crests at $t = 40$ ms and propagates till $t = 80$ ms. As merging of two waves is one of the characteristics of shock waves [82], hence the present findings in our experiments essentially proves that these nonlinear waves can be identified as Dust Acoustic Shock Waves (DASW).

7.5.3 Modification on the propagation characteristics of DASWs due to dust density inhomogeneity

To study the modification in the propagation characteristics due to the inhomogeneity in the equilibrium dust density, we carry out a detailed analysis of the evolution of the dust acoustic shock waves when they are excited in an inhomogeneous dusty plasma. Figure 7.7(a) shows the time evolution of one of the shock fronts in intervals of 0.1 s. The shock front is represented by the density compression

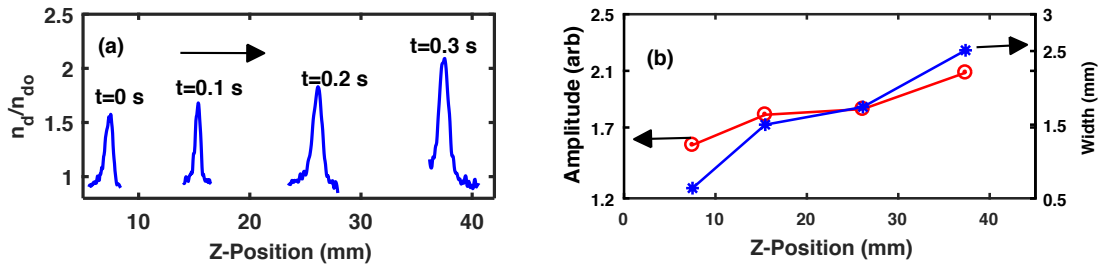


Figure 7.7: (a) Time evolution of shock wave front in space. (b) Variation of amplitude and width of that particular shock front in space as shown in Fig. 7.7(a).

sion factor, defined by the standard expression $n_d(z)/n_{do}(z) \sim I(z)/I_o(z)$ [82, 209], where $n_d(z)$ is the instantaneous dust density and $n_{do}(z)$ is the background equilibrium dust density at the same z -location, whereas $I(z)$ and $I_o(z)$ are the intensities of the perturbed dust cloud and background equilibrium dust cloud, respectively. It is clear from the figure that the shock front propagates from left to right (i.e. away from the wire) and while propagating, the compression factor n_d/n_{do} of that particular shock front increases due to the decrease in the dust density. Figure 7.7(b) shows a quantitative analysis of the amplitude and width of shock wave front while it propagates. One can clearly see that the amplitude of a particular shock front increases and width broadens up in the course of propagation. In addition, as seen in Fig. 7.7(a), the wave front progressively travels longer distances

(7.90 mm, 10.73 mm and 11.4 mm) for a given time duration of 0.1 s. It essentially indicates that the wave front propagates with a higher velocity as it moves through a lower density medium. As is well known from theoretical and experimental studies of nonlinear waves like cnoidal waves, solitons etc., the speed of a nonlinear wave depends on its amplitude [30, 177, 199, 210]. The change in amplitude is inversely proportional to the equilibrium values of both the dust charge and the dust density as discussed in past theoretical studies [92, 211, 212]. Thus the existence of a density gradient and charge gradient can change the amplitude and thereby change the velocity of the wave. The two gradients are related - a dust density gradient can lead to a dust charge gradient [54]. In our experiments, the dust density drops from 2×10^{10} to $0.7 \times 10^{10} / m^3$ over a distance of 35 mm. Using the Collision Enhanced Plasma Collection (CEC) model [54] we have calculated the corresponding change in dust charge over the same distance and found it to change from 1.50×10^{-15} to 1.53×10^{-15} C. Thus while the percentage change in dust density is $\sim 65\%$ the corresponding change in charge is only $\sim 2\%$. Therefore the influence of the dust charge density can be taken to be negligible and the principle effect on the amplitude comes from the density gradient - it increases as it travels towards a region of lower density and consequently its speed increases. This is consistent with the experimental observation.

The shock parameters, namely the amplitude and the width are obtained by following the technique used by Heinrich *et al.* [82] and Annibaldi *et al.* [209]. For a given z , the amplitude is estimated by $n_d/n_{do} - 1$, whereas the shock width (or thickness) is defined as the difference between the steep edge point and the peak point of a shock front. It is to be noted that all the shock fronts are considered for different experimental shots and their amplitudes and widths are calculated

by binning the space along the axial direction and this is plotted in Fig. 7.8. It shows that as the shock waves propagate from higher density (nearby the wire) to lower density (far away from the wire), both the amplitudes (see Fig. 7.8(a)) and the widths (see Fig. 7.8(b)) follow the same increasing trend. These present findings are in contrast to a homogeneous dusty plasma where it is found that both the amplitude and width of shock waves decrease in course of time due to the presence of strong dissipation in the medium [82]. However in our experiments, the

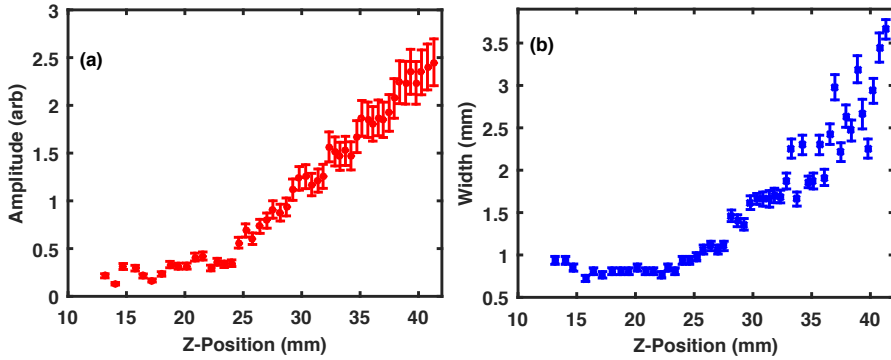


Figure 7.8: Variation of (a) amplitude and (b) width of shock fronts along z -position.

wave train with its large amplitude (due to the manner of its excitation) is highly nonlinear and experiences both growth (due to propagation in a decreasing density gradient) and damping due to dust-dust correlations (viscosity) and dust-neutral interactions (collisions). The combination of these factors lead to a propagating steady state wave form with the characteristics of an asymmetric (steepened) wave form that we observe in the experiments. The increasing profile of shock amplitude is in agreement with past theoretical predictions of Zhang *et al.* [92]. However, the increasing trend of shock thickness (width) with the density inhomogeneity has not been observed or studied earlier.

In order to distinguish between the inhomogeneity effects on a linear perturba-

tion and that on a nonlinear structure like our present shock structures we have compared the plot of the experimental compression factor with that of a hypothetical linear compression factor as it propagates in an inhomogeneous medium. The compression factor of a linear perturbation would increase as n_d^{-1} by the very definition of the factor. This is shown in Fig 7.9 where the curve with ‘o’ symbol represents the estimated compression factor of a linear wave propagating down a density gradient. The ‘*’ symbol shows the experimentally obtained compression factor of the shock fronts at different spatial locations and the trend shows a significant deviation from the linear result thereby establishing that the propagation characteristics of the dust acoustic shock wave is distinctly different in an inhomogeneous medium as compared to a linear wave. The solid line fitted to the experimental data shows the scaling of the peak amplitude (n_{dmax}/n_{do}) to be proportional to $1/(n_{do})^{5/4}$. The amplitude scaling is similar to that predicted theoretically by Singh *et al.* [211, 212] for nonlinear dust acoustic waves.

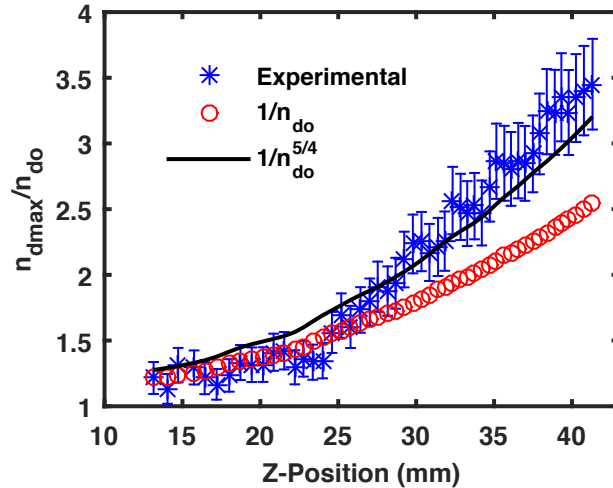


Figure 7.9: Spatial variation of compression factors obtained experimentally and theoretically.

7.6 Theoretical Modelling

To model our experimental results, we have derived analytically a modified KdV-Burger equation in an inhomogeneous dusty plasma. As discussed in Sec. 7.2 and Sec. 7.5, our experimental conditions ensure that there is no significant axial variation of dust size and dust charge in the dust layer under investigation. We have therefore ignored such variations in our theoretical model. Instead, we have only considered the effect of dust density gradient to study the propagation characteristics of dust acoustic shock waves in an inhomogeneous dusty plasma. Furthermore the experimental results pertain to shock front propagation in the axial direction only and so our theoretical model is restricted to one dimensional wave motion. For the dust acoustic wave dynamics the inertia of electrons and ions can be neglected as they are lighter than the dust component. Under these conditions, the electrons and ions are governed by Boltzmann distributions defined by their respective temperatures T_e and T_i as:

$$n_e = n_{eo} \exp\left(\frac{e\phi}{T_e}\right), \quad (7.1)$$

$$n_i = n_{io} \exp\left(-\frac{e\phi}{T_i}\right), \quad (7.2)$$

where ϕ is the electrostatic potential. It has been reported in the earlier experiments of Jaiswal *et al.* [115] that the plasma density remains nearly constant along the axial direction. Hence, the equilibrium electron (n_{eo}) and ion (n_{io}) densities are taken to be constant in the theoretical model. In the theoretical model, the dust particle motion is assumed to be adiabatic and as a result, we use the γ -model to express the dust pressure (p_d) as $\nabla p_d = \gamma_d T_d \nabla n_d$, where γ_d , T_d and n_d are

the adiabatic constant, the dust temperature and the instantaneous dust density respectively. The governing fluid equations for such a system can be written as:

$$\frac{\partial n_d}{\partial t} + \frac{\partial(n_d v_d)}{\partial x} = 0, \quad (7.3)$$

$$\frac{\partial v_d}{\partial t} + v_d \frac{\partial v_d}{\partial x} - \frac{Z_d e}{m_d} \frac{\partial \phi}{\partial x} + \nu_{dn} v_d + \gamma_d v_{td}^2 \frac{1}{n_d} \frac{\partial n_d}{\partial x} = \frac{\eta_l}{n_d} \frac{\partial^2 v_d}{\partial x^2}, \quad (7.4)$$

$$\frac{\partial^2 \phi}{\partial x^2} + 4\pi e(n_i - n_e - Z_d n_d) = 0, \quad (7.5)$$

where $v_{td} = \sqrt{\frac{T_d}{m_d}}$ and $n_d, v_d, \phi, m_d, Z_d, v_{td}$ are the density, velocity, electrostatic potential, mass, charge, and thermal velocity of the charged particles respectively. The dust velocity v_d used in the continuity and momentum equations (in Eqns. 7.3 and 7.4) is the instantaneous velocity of the perturbed dust fluid element - the perturbation that leads to the formation of the nonlinear dust acoustic wave. In the model calculation we have ignored the gas flow velocity assuming it to be much smaller than the dust acoustic speed [211, 212]. The other parameters come from the background properties of the medium with $\nu_{dn}, \eta_l, n_i, n_e$, representing the dust-neutral collision frequency, viscosity and the background electron and ion densities respectively. The coupling between the dust particles provides bulk viscosity [75] in the medium which plays the role of dissipation. Due to this reason, the strong coupling induced viscosity is included in the momentum equation. In addition, the effect of frequent dust neutral collisions is also considered in the momentum equation (Eq. 7.4) through the inclusion of the fourth term, by which the waves experience collisional damping while propagating.

A suitable set of stretched coordinates for the inhomogeneous plasmas can be defined by

$$\xi = \epsilon^{1/2} \left(\int^x \frac{dx'}{\lambda(x')} - t \right), \quad \eta = \epsilon^{3/2} x, \quad (7.6)$$

where ϵ is the smallness parameter and λ is the velocity of the moving frame which can be determined self consistently $\eta_o = \epsilon^{1/2}\eta_l$ and $\nu_{dn} = \epsilon^{3/2}\nu_o$. Since we are considering only spatial gradients so,

$$\frac{\partial n_{do}}{\partial \xi} = 0; \quad \frac{\partial \lambda}{\partial \xi} = 0; \quad \frac{\partial \phi_o}{\partial \xi} = 0; \quad \frac{\partial v_{do}}{\partial \xi} = 0. \quad (7.7)$$

Using equations (6)–(7) into equations (3)–(5) we obtain the continuity equation in the form,

$$-\lambda \frac{\partial n_d}{\partial \xi} + \frac{\partial(n_d v_d)}{\partial \xi} + \epsilon \lambda \frac{\partial(n_d v_d)}{\partial \xi} = 0, \quad (7.8)$$

and the momentum equation becomes,

$$\begin{aligned} & -\lambda^2 \frac{\partial v_d}{\partial \xi} + \lambda v_d \frac{\partial v_d}{\partial \xi} + v_d \epsilon \lambda^2 \frac{\partial v_d}{\partial \eta} - \frac{Z_d e \lambda}{m_d} \frac{\partial \phi}{\partial \xi} - \frac{Z_d e \lambda^2 \epsilon}{m_d} \frac{\partial \phi}{\partial \eta} + \frac{\lambda \gamma_d v_{td}^2}{n_d} \frac{\partial n_d}{\partial \xi} + \lambda^2 \epsilon \nu_o v_d \\ & + \frac{\lambda^2 \epsilon \gamma_d v_{td}^2}{n_d} \frac{\partial n_d}{\partial \eta} = \frac{\eta_o}{n_d} \epsilon \frac{\partial^2 v_d}{\partial \xi^2} + \frac{2\lambda \eta_o \epsilon^2}{n_d} \frac{\partial^2 v_d}{\partial \xi \partial \eta} - \frac{\eta_o \epsilon^2}{n_d} \frac{\partial \lambda}{\partial \eta} \frac{\partial n_d}{\partial \xi} + \frac{\eta_o \epsilon^3}{n_d} \frac{\partial^2 v_d}{\partial \eta^2}. \end{aligned} \quad (7.9)$$

The Poisson equation is now given as:

$$\begin{aligned} & \epsilon \frac{\partial^2 \phi}{\partial \xi^2} + 2\epsilon^2 \lambda \frac{\partial^2 \phi}{\partial \xi \partial \eta} - \epsilon^2 \frac{\partial \lambda}{\partial \eta} \frac{\partial \phi}{\partial \xi} + \epsilon^3 \lambda^2 \frac{\partial^2 \phi}{\partial \eta^2} \\ & + 4\pi \lambda^2 \left(n_{io} \exp\left(\frac{-e\phi}{T_i}\right) - n_{eo} \exp\left(\frac{e\phi}{T_e}\right) - Z_d n_d \right) = 0. \end{aligned} \quad (7.10)$$

We next expand the dependent variables n_d, v_d and ϕ in terms of the smallness parameter ϵ as

$$\psi = \psi_o + \epsilon \psi_1 + \epsilon^2 \psi_2 + \dots \quad (7.11)$$

The first order equations in ϵ of continuity, momentum and Poisson equation leads

to the self consistent relation,

$$\lambda = v_{do} + \sqrt{(C_{da}^2 + \gamma_d v_{td}^2)}, \quad (7.12)$$

where $\mu = \sqrt{(C_{da}^2 + \gamma_d v_{td}^2)}$. In order to derive a modified KdV Burger equation for the in-homogeneous dusty plasma we equate the coefficients of ϵ^2 to zero. The final modified KdV-Burger (m-KdV-Burger) equation governing the shock propagation in a nonuniform dusty plasma can be expressed by:

$$\frac{\partial n_{d1}}{\partial \eta} + A \frac{\partial^3 n_{d1}}{\partial \xi^3} + B n_{d1} \frac{\partial n_{d1}}{\partial \xi} + C \frac{n_{d1}}{2} = D \frac{\partial^2 n_{d1}}{\partial \xi^2}. \quad (7.13)$$

The terms of Eq. 7.13 having the coefficients A , B and D represent dispersive, non-linear and dissipative contributions that normally appear in the KdV Burger equation. The term proportional to ‘ C ’ in the model equation arises due to the dust density inhomogeneity and dust-neutral collisions. The detailed expressions for the coefficients are:

$$A = \frac{1}{2n_{do}C_{da}}, \quad (7.14)$$

$$B = \frac{C_{da}^3 T_e}{2n_{do}^2 Z_d e} \left[\frac{1}{Z_d^2} (\sigma_{ei}^2 n_{io} - n_{eo}) - \frac{3Z_d n_{do}}{C_{da}^4} \right], \quad (7.15)$$

$$C = \frac{1}{2n_{do}} \frac{\partial n_{do}}{\partial \eta} + \frac{\nu_o}{2C_{da}}, \quad (7.16)$$

$$D = \frac{\eta_o}{2C_{da}^3 n_{do}}. \quad (7.17)$$

As the background dust density (n_{do}) is a function of the axial distance all the coefficients including C_{da} are also functions of the axial distance. In Eq. 7.13 as well as in the above coefficients, normalized quantities are used where space is

normalized by $\sqrt{\frac{\epsilon_0 k_B T_e}{n_{io} e^2}}$, time is normalized by $\sqrt{\frac{m_d \epsilon_0}{n_{io} e^2}}$, velocity is normalized by $\sqrt{\frac{k_B T_e}{m_d}}$ and density is normalized by n_{io} . The normalizations are the same as used in references [211, 212] with ϵ_0 and k_B being the permittivity of free space and Boltzmann constant, respectively. While calculating the above coefficients, we have used the experimental values of $T_e = 4\text{eV}$, $n_{io} = 1.5 \times 10^{15} \text{ m}^{-3}$, $Z_d = 10^4$, $\nu_0 = 11 \text{ Hz}$, $\eta_0 = 0.2$ [83] and $\sigma_{ei} = T_e/T_i = 133$ for $T_i = 0.03 \text{ eV}$. A general solution of this equation, even numerically, is quite challenging. So to make some progress and make contact with the experimental results, we have solved this equation locally for constant coefficients at different points of the density profiles and corresponding different values of the coefficients. Fig. 7.10 shows

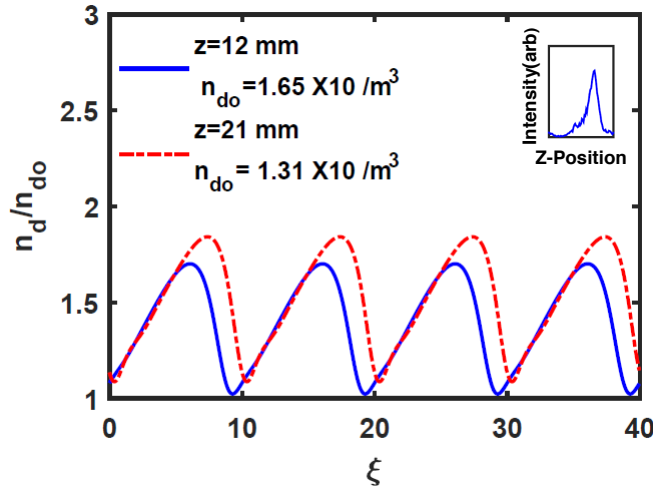


Figure 7.10: Typical shock wave train obtained from the numerical solution of m-KdV-Burger equation. Inset shows the same that is obtained experimentally.

typical such numerical solutions of Eq. 7.13, by assuming a uniform dusty plasma with a density value corresponding to the experimental value at $z = 12 \text{ mm}$ (solid line) and $z = 21 \text{ mm}$ (dashed line). In other words, the solutions are obtained by calculating the corresponding values of A, B, C and D for these two points and assuming them to remain constant. These plots show that the modified KdV-

Burger equation admits solutions that qualitatively describe the profile of our experimentally observed sawteeth structures and represent nonlinear propagating wave trains [205] resulting from the balance of nonlinear steepening, nonlinear growth due to the inhomogeneity, dispersive broadening and dissipative damping due to dust-dust correlations and dust neutral collisions. The inset in Figure 7.10 shows the experimentally obtained profile of a single shock front extracted from the experimental image shown in Fig. 7.3(a). One can see that the numerically obtained profile of a single shock front is very similar to that of the experimental profile. To see the change in amplitude as well as the width of the sawtooth profile as a function of z we have used such local solutions over the entire range of the density profile, namely from 2.0×10^{10} to $0.7 \times 10^{10} / \text{m}^3$, and plotted the values of the amplitudes and widths in Fig. 7.11. The corresponding values of the coefficients vary in the range $A = 0.0383$ to 0.1466 , $B = 0.4595$ to 1.7588 , $C = 0.4931$ to 0.7648 and $D = 0.0008$ to 0.0073 . One can now clearly see, that as in the experiments, the amplitude and width of a single shock structure increases when it propagates down the density gradient. Thus the m-KdV Burger model provides a good qualitative description of the present experimental results.

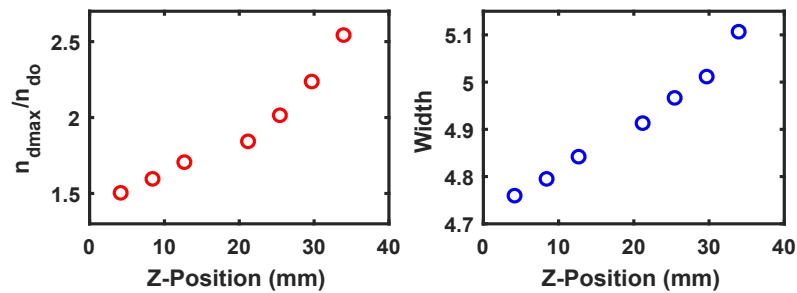


Figure 7.11: (a) Amplitude and (b) Width profile estimated from the numerical solution of m-KdV Burger equation.

7.7 Conclusions

To summarize, we have carried out for the first time a systematic experimental study on the excitation and propagation of non-linear dust acoustic shock waves in an inhomogeneous dusty plasma. The experiments are done in the Dusty Plasma Experimental (DPEX) device in which a direct current glow discharge Argon plasma is formed. A dusty plasma of Kaolin particles is then formed in between an axial confining strip and a grounded copper wire which is installed radially at the midway of the cathode. The inhomogeneity in the dust density is then created by inducing an imbalance of the dynamical equilibrium between the pumping speed and the gas flow rate. A sudden increase of dust density is created by compressing the dust cloud using a single gas injection technique that led to the excitation of a series of nonlinear structures. These structures are characterized by a high compression factor, sharp peaks and a single saw-tooth like profile which are all signatures of a shock wave. The amplitude and the widths of these shock waves are measured along the axial direction from the wire where the equilibrium dust density falls monotonically. It is found that the amplitude increases and width broadens up as the shock structure propagates down the dust density gradient. To provide some theoretical understanding of our experimental findings we have developed a model equation in the form of a modified KdV-Burger. The model takes account of the density inhomogeneity of the dust component, the bulk viscosity due to dust-dust coupling and damping due to dust-neutral collisions. Numerical solutions of this equation at various density values show spatial profiles as well as variations in the amplitude and width of shock like structures that closely resemble the experimental results. The results, obtained under controlled laboratory

conditions, can help in extending our basic understanding of shock structures in inhomogeneous media and may also find useful applications in the interpretation in related phenomena in astrophysical situations.

Bibliography

- [1] P. K. Shukla and B. Eliasson. *Rev. Mod. Phys.*, 81:25–44, Jan 2009.
- [2] Gregor E. Morfill and Alexei V. Ivlev. *Rev. Mod. Phys.*, 81:1353–1404, Oct 2009.
- [3] Rhian Jones and Ed Scott. *Chondrules and the protoplanetary disk*. Cambridge University Press, 1996.
- [4] CK Goertz. Dusty plasmas in the solar system. *Reviews of Geophysics*, 27(2):271–292, 1989.
- [5] J Blum, A-C Levasseur-Regourd, O Muñoz, RJ Slobodrian, and A Vedernikov. Dust in space. *Europhysics news*, 39(3):27–29, 2008.
- [6] Larry W Esposito. Planetary rings. *Reports on Progress in Physics*, 65(12):1741, 2002.
- [7] Gary S Selwyn, J Singh, and RS Bennett. In situ laser diagnostic studies of plasma-generated particulate contamination. *Journal of Vacuum Science & Technology A: Vacuum, Surfaces, and Films*, 7(4):2758–2765, 1989.
- [8] Sergej V Vladimirov and Kostya Ostrikov. Dynamic self-organization phenomena in complex ionized gas systems: new paradigms and technological aspects. *Physics Reports*, 393(3-6):175–380, 2004.
- [9] Indrajit Roy, Tymish Y Ohulchanskyy, Dhruba J Bharali, Haridas E Pudarav, Ruth A Mistretta, Navjot Kaur, and Paras N Prasad. Optical tracking of organically modified silica nanoparticles as dna carriers: a nonvi-

-
- ral, nanomedicine approach for gene delivery. *Proceedings of the National Academy of Sciences*, 102(2):279–284, 2005.
- [10] E Stoffels, IE Kieft, and REJ Sladek. Superficial treatment of mammalian cells using plasma needle. *Journal of Physics D: Applied Physics*, 36(23):2908, 2003.
- [11] Mounir Laroussi, DA Mendis, and M Rosenberg. Plasma interaction with microbes. *New Journal of Physics*, 5(1):41, 2003.
- [12] J Winter. Dust in fusion devices-experimental evidence, possible sources and consequences. *Plasma physics and controlled fusion*, 40(6):1201, 1998.
- [13] WP West, BD Bray, and J Burkart. Measurement of number density and size distribution of dust in dIII-d during normal plasma operation. *Plasma physics and controlled fusion*, 48(11):1661, 2006.
- [14] H. Ikezi. *The Physics of Fluids*, 29(6):1764–1766, 1986.
- [15] A Barkan, Robert L Merlino, and N D’angelo. *Phys. Plasmas*, 2(10):3563–3565, 1995.
- [16] C. Dietz, R. Bergert, B. Steinmüller, M. Kretschmer, S. Mitic, and M. H. Thoma. fcc-bcc phase transition in plasma crystals using time-resolved measurements. *Phys. Rev. E*, 97:043203, Apr 2018.
- [17] Hubertus M Thomas and Gregor E Morfill. Melting dynamics of a plasma crystal. *Nature*, 379(6568):806–809, 1996.

-
- [18] André Schella, Matthias Mulsow, and André Melzer. Recrystallization in finite 3-d dust clouds. *IEEE Transactions on Plasma Science*, 42(10):2682–2683, 2014.
- [19] Giedrius Kudelis, Hauke Thomsen, and Michael Bonitz. Heat transport in confined strongly coupled two-dimensional dust clusters. *Physics of Plasmas*, 20(7):073701, 2013.
- [20] V Nosenko, S Zhdanov, AV Ivlev, G Morfill, J Goree, and A Piel. Heat transport in a two-dimensional complex (dusty) plasma at melting conditions. *Physical review letters*, 100(2):025003, 2008.
- [21] VE Fortov, OS Vaulina, OF Petrov, MN Vasiliev, AV Gavrikov, IA Shakova, NA Vorona, Yu V Khrustalyov, AA Manohin, and AV Chernyshev. Experimental study of the heat transport processes in dusty plasma fluid. *Physical Review E*, 75(2):026403, 2007.
- [22] D. Samsonov, J. Goree, Z. W. Ma, A. Bhattacharjee, H. M. Thomas, and G. E. Morfill. Mach cones in a coulomb lattice and a dusty plasma. *Phys. Rev. Lett.*, 83:3649–3652, Nov 1999.
- [23] D. Samsonov, J. Goree, H. M. Thomas, and G. E. Morfill. Mach cone shocks in a two-dimensional yukawa solid using a complex plasma. *Phys. Rev. E*, 61:5557–5572, May 2000.
- [24] Chun-Shang Wong, J Goree, Zach Haralson, and Bin Liu. Strongly coupled plasmas obey the fluctuation theorem for entropy production. *Nature Physics*, 14(1):21–24, 2018.

-
- [25] A. Barkan, R. L. Merlino, and N. D'Angelo. *Physics of Plasmas*, 2(10):3563–3565, 1995.
- [26] N.N. Rao, P.K. Shukla, and M.Y. Yu. *Planetary and Space Science*, 38(4):543 – 546, 1990.
- [27] N.N. Rao, P.K. Shukla, and M.Y. Yu. Dust-acoustic waves in dusty plasmas. *Planetary and Space Science*, 38(4):543 – 546, 1990.
- [28] P K Shukla and V P Silin. *Physica Scripta*, 45(5):508, 1992.
- [29] Frank Melandso/. Lattice waves in dust plasma crystals. *Physics of Plasmas*, 3(11):3890–3901, 1996.
- [30] P. Bandyopadhyay, G. Prasad, A. Sen, and P. K. Kaw. Experimental study of nonlinear dust acoustic solitary waves in a dusty plasma. *Phys. Rev. Lett.*, 101:065006, Aug 2008.
- [31] D. Samsonov, A. V. Ivlev, R. A. Quinn, G. Morfill, and S. Zhdanov. Dissipative longitudinal solitons in a two-dimensional strongly coupled complex (dusty) plasma. *Phys. Rev. Lett.*, 88:095004, Feb 2002.
- [32] D. Samsonov, G. Morfill, H. Thomas, T. Hagl, H. Rothermel, V. Fortov, A. Lipaev, V. Molotkov, A. Nefedov, O. Petrov, A. Ivanov, and S. Krikalev. Kinetic measurements of shock wave propagation in a three-dimensional complex (dusty) plasma. *Phys. Rev. E*, 67:036404, Mar 2003.
- [33] P. K. Shukla and A. A. Mamun. Dust-acoustic shocks in a strongly coupled dusty plasma. *IEEE Transactions on Plasma Science*, 29(2):221–225, April 2001.

-
- [34] E. Thomas, K. Avinash, and R. L. Merlino. Probe induced voids in a dusty plasma. *Physics of Plasmas*, 11(5):1770–1774, 2004.
- [35] D. Samsonov and J. Goree. *Phys. Rev. E*, 59:1047–1058, Jan 1999.
- [36] A. M. Lipaev, S. A. Khrapak, V. I. Molotkov, G. E. Morfill, V. E. Fortov, A. V. Ivlev, H. M. Thomas, A. G. Khrapak, V. N. Naumkin, A. I. Ivanov, S. E. Tretschnev, and G. I. Padalka. Void closure in complex plasmas under microgravity conditions. *Phys. Rev. Lett.*, 98:265006, Jun 2007.
- [37] J. Goree, G. E. Morfill, V. N. Tsytovich, and S. V. Vladimirov. Theory of dust voids in plasmas. *Phys. Rev. E*, 59:7055–7067, Jun 1999.
- [38] Manjit Kaur, Sayak Bose, P. K. Chattopadhyay, Devendra Sharma, J. Ghosh, and Y. C. Saxena. Observation of dust torus with poloidal rotation in direct current glow discharge plasma. *Physics of Plasmas*, 22(3):033703, 2015.
- [39] Mangilal Choudhary, S. Mukherjee, and P. Bandyopadhyay. Experimental observation of self excited co-rotating multiple vortices in a dusty plasma with inhomogeneous plasma background. *Physics of Plasmas*, 24(3):033703, 2017.
- [40] Daniel H. E. Dubin. The phonon wake behind a charge moving relative to a two-dimensional plasma crystal. *Physics of Plasmas*, 7(10):3895–3903, 2000.
- [41] O. Havnes, F. Li, F. Melandso/, T. Aslaksen, T. W. Hartquist, G. E. Morfill, T. Nitter, and V. Tsytovich. Diagnostic of dusty plasma conditions by the observation of mach cones caused by dust acoustic waves. *Journal of Vacuum Science & Technology A*, 14(2):525–528, 1996.

-
- [42] A. A. Mamun, P. K. Shukla, and G. E. Morfill. Theory of mach cones in magnetized dusty plasmas with strongly correlated charged dust grains. *Phys. Rev. Lett.*, 92:095005, Mar 2004.
- [43] Lu-Jing Hou, You-Nian Wang, and Z. L. Mišković. Theoretical study of laser-excited mach cones in dusty plasmas. *Phys. Rev. E*, 70:056406, Nov 2004.
- [44] N. J. Zabusky and C. J. Galvin. *Journal of Fluid Mechanics*, 47(4):811–824, 1971.
- [45] T Yao-Tsu Wu. Generation of upstream advancing solitons by moving disturbances. *Journal of fluid mechanics*, 184:75–99, 1987.
- [46] MG Sun. The evolution of waves created by a ship in a shallow canal. *The 60th Anniversary Volume Mechanics Essays*, pages 17–25, 1985.
- [47] Abhijit Sen, Sanat Tiwari, Sanjay Mishra, and Predhiman Kaw. *Advances in Space Research*, 56(3):429 – 435, 2015. Advances in Asteroid and Space Debris Science and Technology - Part 1.
- [48] Surabhi Jaiswal, P. Bandyopadhyay, and A. Sen. *Phys. Rev. E*, 93:041201, Apr 2016.
- [49] Abhijit Sen, Sanat Tiwari, Sanjay Mishra, and Predhiman Kaw. Nonlinear wave excitations by orbiting charged space debris objects. *Advances in Space Research*, 56(3):429 – 435, 2015. Advances in Asteroid and Space Debris Science and Technology - Part 1.

-
- [50] Sanat Kumar Tiwari and Abhijit Sen. Wakes and precursor soliton excitations by a moving charged object in a plasma. *Physics of Plasmas*, 23(2):022301, 2016.
- [51] Sanat Kumar Tiwari and Abhijit Sen. Fore-wake excitations from moving charged objects in a complex plasma. *Physics of Plasmas*, 23(10):100705, 2016.
- [52] Padma K Shukla and AA Mamun. *Introduction to dusty plasma physics*. CRC Press, 2015.
- [53] J E Allen. *Physica Scripta*, 45(5):497, 1992.
- [54] S. A. Khrapak, S. V. Ratynskaia, A. V. Zobnin, A. D. Usachev, V. V. Yaroshenko, M. H. Thoma, M. Kretschmer, H. Höfner, G. E. Morfill, O. F. Petrov, and V. E. Fortov. Particle charge in the bulk of gas discharges. *Phys. Rev. E*, 72:016406, Jul 2005.
- [55] S. A. Khrapak and G. E. Morfill. Grain surface temperature in noble gas discharges: Refined analytical model. *Physics of Plasmas*, 13(10):104506, 2006.
- [56] H. Ikezi. *Phys. Fluids*, 29(6):1764–1766, 1986.
- [57] TG Northrop and TJ Birmingham. Plasma drag on a dust grain due to coulomb collisions. *Planetary and space science*, 38(3):319–326, 1990.
- [58] Michael S. Barnes, John H. Keller, John C. Forster, James A. O’Neill, and D. Keith Coultas. *Phys. Rev. Lett.*, 68:313–316, Jan 1992.

-
- [59] S. A. Khrapak, A. V. Ivlev, G. E. Morfill, and H. M. Thomas. *Phys. Rev. E*, 66:046414, Oct 2002.
- [60] S. A. Khrapak, A. V. Ivlev, S. K. Zhdanov, and G. E. Morfill. *Physics of Plasmas*, 12(4):042308, 2005.
- [61] SA Khrapak, AV Ivlev, SK Zhdanov, and GE Morfill. *Physics of plasmas*, 12(4):042308, 2005.
- [62] Paul S. Epstein. *Phys. Rev.*, 23:710–733, Jun 1924.
- [63] H Vestner and L Waldmann. Generalized hydrodynamics of thermal transpiration, thermal force and friction force. *Physica A: Statistical Mechanics and its Applications*, 86(2):303–336, 1977.
- [64] GM Jellum, JE Daugherty, and DB Graves. Particle thermophoresis in low pressure glow discharges. *Journal of applied physics*, 69(10):6923–6934, 1991.
- [65] Bin Liu, John Goree, Vladimir Nosenko, and Laifa Boufendi. *Physics of Plasmas*, 10(1):9–20, 2003.
- [66] S Hamaguchi and RT Farouki. Plasma–particulate interactions in nonuniform plasmas with finite flows. *Physics of plasmas*, 1(7):2110–2118, 1994.
- [67] F Melandsø, T Aslaksen, and O Havnes. A new damping effect for the dust-acoustic wave. *Planetary and space science*, 41(4):321–325, 1993.
- [68] JB Pieper and J Goree. Dispersion of plasma dust acoustic waves in the strong-coupling regime. *Physical review letters*, 77(15):3137, 1996.
- [69] PK Shukla. Dust acoustic wave in a thermal dusty plasma. *Physical Review E*, 61(6):7249, 2000.

-
- [70] P K Shukla and V P Silin. Dust ion-acoustic wave. *Physica Scripta*, 45(5):508, 1992.
- [71] Ioannis Kourakis and Padma Kant Shukla. Modulational instability and localized excitations of dust-ion acoustic waves. *Physics of Plasmas*, 10(9):3459–3470, 2003.
- [72] Xue Jukui and Lang He. Modulational instability of cylindrical and spherical dust ion-acoustic waves. *Physics of Plasmas*, 10(2):339–342, 2003.
- [73] Frank Melandso/. *Physics of Plasmas*, 3(11):3890–3901, 1996.
- [74] Frank Melandso/. *Phys. Plasmas*, 3(11):3890–3901, 1996.
- [75] PK Kaw and A Sen. Low frequency modes in strongly coupled dusty plasmas. *Physics of Plasmas*, 5(10):3552–3559, 1998.
- [76] J. Pramanik, G. Prasad, A. Sen, and P. K. Kaw. Experimental observations of transverse shear waves in strongly coupled dusty plasmas. *Phys. Rev. Lett.*, 88:175001, Apr 2002.
- [77] P Bandyopadhyay, G Prasad, A Sen, and PK Kaw. Driven transverse shear waves in a strongly coupled dusty plasma. *Physics Letters A*, 372(33):5467–5470, 2008.
- [78] JX Ma and Jinyuan Liu. Dust-acoustic soliton in a dusty plasma. *Physics of plasmas*, 4(2):253–255, 1997.
- [79] Padma K Shukla and AA Mamun. Dust-acoustic shocks in a strongly coupled dusty plasma. *IEEE transactions on plasma science*, 29(2):221–225, 2001.

-
- [80] Y. Nakamura, H. Bailung, and P. K. Shukla. Observation of ion-acoustic shocks in a dusty plasma. *Phys. Rev. Lett.*, 83:1602–1605, Aug 1999.
- [81] Y. Saitou, Y. Nakamura, T. Kamimura, and O. Ishihara. Bow shock formation in a complex plasma. *Phys. Rev. Lett.*, 108:065004, Feb 2012.
- [82] J. Heinrich, S.-H. Kim, and R. L. Merlino. Laboratory observations of self-excited dust acoustic shocks. *Phys. Rev. Lett.*, 103:115002, Sep 2009.
- [83] S. Jaiswal, P. Bandyopadhyay, and A. Sen. *Physics of Plasmas*, 23(8):083701, 2016.
- [84] Y. Nakamura, H. Bailung, and P. K. Shukla. Observation of ion-acoustic shocks in a dusty plasma. *Phys. Rev. Lett.*, 83:1602–1605, Aug 1999.
- [85] PK Shukla and Bengt Eliasson. Nonlinear dynamics of large-amplitude dust acoustic shocks and solitary pulses in dusty plasmas. *Physical Review E*, 86(4):046402, 2012.
- [86] Sandeep Kumar, Sanat Kumar Tiwari, and Amita Das. Observation of the korteweg-de vries soliton in molecular dynamics simulations of a dusty plasma medium. *Physics of Plasmas*, 24(3):033711, 2017.
- [87] PK Kaw, A Sen, and T Katsouleas. Nonlinear 1d laser pulse solitons in a plasma. *Physical review letters*, 68(21):3172, 1992.
- [88] R. Heidemann, S. Zhdanov, R. Sütterlin, H. M. Thomas, and G. E. Morfill. Dissipative dark soliton in a complex plasma. *Phys. Rev. Lett.*, 102:135002, Mar 2009.

-
- [89] AA Mamun and PK Shukla. Nonlinear waves and structures in dusty plasmas. *Plasma physics and controlled fusion*, 47(5A):A1, 2005.
- [90] MR Gupta, Susmita Sarkar, Samiran Ghosh, M Debnath, and Manoranjan Khan. Effect of nonadiabaticity of dust charge variation on dust acoustic waves: Generation of dust acoustic shock waves. *Physical Review E*, 63(4):046406, 2001.
- [91] De-long Xiao, JX Ma, and Yang-fang Li. Dust-acoustic shock waves: Effect of plasma density gradient. *Physics of plasmas*, 12(5):052314, 2005.
- [92] Li-Ping Zhang, Dong-Ao Li, and Hong-Mei Du. Propagation of shock structures in inhomogeneous dusty plasmas with dust size distribution and nonadiabatic dust charge fluctuation. *Indian Journal of Physics*, pages 1–8, 2019.
- [93] Q-Z Luo, N D'Angelo, and RL Merlino. Experimental study of shock formation in a dusty plasma. *Physics of Plasmas*, 6(9):3455–3458, 1999.
- [94] A Gavrikov, I Shakhova, A Ivanov, O Petrov, N Vorona, and V Fortov. Experimental study of laminar flow in dusty plasma liquid. *Physics Letters A*, 336(4-5):378–383, 2005.
- [95] TM Flanagan and J Goree. Gas flow driven by thermal creep in dusty plasma. *Physical Review E*, 80(4):046402, 2009.
- [96] M Schwabe, LJ Hou, S Zhdanov, AV Ivlev, HM Thomas, and GE Morfill. Convection in a dusty radio-frequency plasma under the influence of a thermal gradient. *New Journal of Physics*, 13(8):083034, 2011.
- [97] Yoshifumi Saitou and Osamu Ishihara. Dynamic circulation in a complex plasma. *Physical review letters*, 111(18):185003, 2013.

-
- [98] H Kählert, J Carstensen, M Bonitz, H Löwen, F Greiner, and A Piel. Magnetizing a complex plasma without a magnetic field. *Physical review letters*, 109(15):155003, 2012.
- [99] Torben Reichstein, Jochen Wilms, and Alexander Piel. Dust streaming in toroidal traps. *IEEE Transactions on Plasma Science*, 41(4):759–763, 2012.
- [100] Ya-feng He, Bao-quan Ai, Chao-xing Dai, Chao Song, Rui-qi Wang, Wen-tao Sun, Fu-cheng Liu, and Yan Feng. Experimental demonstration of a dusty plasma ratchet rectification and its reversal. *Phys. Rev. Lett.*, 124:075001, Feb 2020.
- [101] MA Fink, SK Zhdanov, MH Thoma, H Höfner, and GE Morfill. Pearl-necklace-like structures of microparticle strings observed in a dc complex plasma. *Physical Review E*, 86(6):065401, 2012.
- [102] Akanksha Gupta, R Ganesh, and Ashwin Joy. Kolmogorov flow in two dimensional strongly coupled dusty plasma. *Physics of Plasmas*, 21(7):073707, 2014.
- [103] V Nosenko and J Goree. Shear flows and shear viscosity in a two-dimensional yukawa system (dusty plasma). *Physical review letters*, 93(15):155004, 2004.
- [104] KA Pacha, JR Heinrich, S-H Kim, and RL Merlino. Observation of the taylor instability in a dusty plasma. *Physics of Plasmas*, 19(1):014501, 2012.
- [105] J Ashwin and R Ganesh. Kelvin helmholtz instability in strongly coupled yukawa liquids. *Physical review letters*, 104(21):215003, 2010.
- [106] Gregor E Morfill, Milenko Rubin-Zuzic, Hermann Rothermel, Alexei V Ivlev, Boris A Klumov, Hubertus M Thomas, Uwe Konopka, and Victor Steinberg.

- Highly resolved fluid flows:“liquid plasmas” at the kinetic level. *Physical review letters*, 92(17):175004, 2004.
- [107] John K Meyer and Robert L Merlino. Transient bow shock around a cylinder in a supersonic dusty plasma. *Physics of Plasmas*, 20(7):074501, 2013.
- [108] S. Jaiswal, M. Schwabe, A. Sen, and P. Bandyopadhyay. *Physics of Plasmas*, 25(9):093703, 2018.
- [109] Harish Charan and Rajaraman Ganesh. Supersonic flows past an obstacle in yukawa liquids. *Physics of Plasmas*, 25(4):043706, 2018.
- [110] A Melzer, S Nunomura, D Samsonov, ZW Ma, and J Goree. Laser-excited mach cones in a dusty plasma crystal. *Physical Review E*, 62(3):4162, 2000.
- [111] V Nosenko, J Goree, ZW Ma, and A Piel. Observation of shear-wave mach cones in a 2d dusty-plasma crystal. *Physical review letters*, 88(13):135001, 2002.
- [112] P Bandyopadhyay, K Jiang, R Dey, and GE Morfill. Effect of polarization force on the mach cones in a complex plasma. *Physics of Plasmas*, 19(12):123707, 2012.
- [113] P Bandyopadhyay, R Dey, Sangeeta Kadyan, and Abhijit Sen. Dynamics of compressional mach cones in a strongly coupled complex plasma. *Physics of Plasmas*, 21(10):103707, 2014.
- [114] Sanat Kumar Tiwari and Abhijit Sen. *Physics of Plasmas*, 23(2):022301, 2016.

-
- [115] S. Jaiswal, P. Bandyopadhyay, and A. Sen. *Review of Scientific Instruments*, 86(11):113503, 2015.
- [116] Jaiswal Surabhi. *Nonlinear excitations in flowing complex plasmas*. PhD thesis, Institute for Plasma Research, 2016.
- [117] J P Sheehan and N Hershkowitz. *Plasma Sources Science and Technology*, 20(6):063001, 2011.
- [118] Y. Feng, J. Goree, and Bin Liu. *Review of Scientific Instruments*, 78(5):053704, 2007.
- [119] W Thielicke and EJ Stamhuis. Pivlab-time-resolved digital particle image velocimetry tool for matlab (version: 1.35). *J. Open Res. Software*, 2(1):e30, 2014.
- [120] EI Toader, A Fredriksen, and A Aanesland. Characterization of a high-density electron-cyclotron resonance plasma source operating in nitrogen. *Review of scientific instruments*, 74(7):3279–3283, 2003.
- [121] VA Godyak, RB Piejak, and BM Alexandrovich. Electron energy distribution function measurements and plasma parameters in inductively coupled argon plasma. *Plasma Sources Science and Technology*, 11(4):525, 2002.
- [122] A Barkan, N D'angelo, and Robert L Merlino. *Physical review letters*, 73(23):3093, 1994.
- [123] Elden C Whipple. Potentials of surfaces in space. *Reports on progress in Physics*, 44(11):1197, 1981.
- [124] S Ratynskaia. *Phys. Rev. Lett.*, 93:085001, 2004.

-
- [125] S. A. Khrapak and G. E. Morfill. *Phys. Plasmas*, 13(10):104506, 2006.
- [126] RL Merlino, JR Heinrich, SH Kim, and JK Meyer. *Plasma Physics and Controlled Fusion*, 54(12):124014, 2012.
- [127] Harish Charan and Rajaraman Ganesh. *Physics of Plasmas*, 23(12):123703, 2016.
- [128] S. Nunomura, D. Samsonov, and J. Goree. *Phys. Rev. Lett.*, 84:5141–5144, May 2000.
- [129] A. Melzer, S. Nunomura, D. Samsonov, Z. W. Ma, and J. Goree. *Phys. Rev. E*, 62:4162–4176, Sep 2000.
- [130] Edward Thomas and Jeremiah Williams. *Phys. Rev. Lett.*, 95:055001, Jul 2005.
- [131] S. V. Vladimirov, S. A. Khrapak, M. Chaudhuri, and G. E. Morfill. *Phys. Rev. Lett.*, 100:055002, Feb 2008.
- [132] J. F. O’Hanlon, Jungwon Kang, L. K. Russell, and L. Hong. *IEEE Transactions on Plasma Science*, 22(2):122–127, Apr 1994.
- [133] V Yaroshenko, S Ratynskaia, S Khrapak, MH Thoma, M Kretschmer, H Höfner, GE Morfill, A Zobnin, A Usachev, O Petrov, et al. *Physics of plasmas*, 12(9):093503, 2005.
- [134] C. Zafiu, A. Melzer, and A. Piel. *Physics of Plasmas*, 9(11):4794–4803, 2002.
- [135] S Jaiswal, P Bandyopadhyay, and A Sen. Flowing dusty plasma experiments: generation of flow and measurement techniques. *Plasma Sources Science and Technology*, 25(6):065021, nov 2016.

-
- [136] Garima Arora, P. Bandyopadhyay, M. G. Hariprasad, and A. Sen. Effect of size and shape of a moving charged object on the propagation characteristics of precursor solitons. *Physics of Plasmas*, 26(9):093701, 2019.
- [137] S Jaiswal, P Bandyopadhyay, and A Sen. *Plasma Sources Science and Technology*, 25(6):065021, 2016.
- [138] U Konopka. Wechselwirkungen geladener staubteilchen in hochfrequenzplasmen phd thesis ruhr university, 2000.
- [139] Mierk Schwabe, Sergey Zhdanov, T Hagl, Peter Huber, AM Lipaev, VI Molotkov, VN Naumkin, Milenko Rubin-Zuzic, PV Vinogradov, Erich Zähringer, et al. *New Journal of Physics*, 19(10):103019, 2017.
- [140] Francis F Chen. *Introduction to plasma physics*. Springer Science & Business Media, 2012.
- [141] R N Franklin. *J. Appl. Phys. D*, 36(22):R309, 2003.
- [142] K. F. Stephens and C. A. Ordonez. *J. Appl. Phys.*, 85(5):2522–2527, 1999.
- [143] R A Behbahani, T D Mahabadi, M Ghoranneviss, M F Aghamir, S E Namini, A Ghorbani, and M Najafi. *Plasma Phys. Control. Fusion*, 52(9):095004, 2010.
- [144] Angela Douglass, Victor Land, Ke Qiao, Lorin Matthews, and Truell Hyde. *Phys. Plasmas*, 19(1):013707, 2012.
- [145] Robert L. Merlino. *Am. J. Phys.*, 75(12):1078–1085, 2007.
- [146] Lewi Tonks and Irving Langmuir. *Phys. Rev.*, 34:876–922, Sep 1929.

-
- [147] J P Sheehan and N Hershkowitz. *Plasma Sources Sci. Technol*, 20(6):063001, 2011.
- [148] M. J. Goeckner, J. Goree, and T. E. Sheridan. *Phys. Fluids B*, 4(6):1663–1670, 1992.
- [149] Paul D. Goldan. *Phys. Fluids*, 13(4):1055–1059, 1970.
- [150] Allen H. Boozer. *The Physics of Fluids*, 19(8):1210–1216, 1976.
- [151] Vara Prasad Kella, Payal Mehta, A. Sarma, J. Ghosh, and P. K. Chattopadhyay. *Rev. Sci. Instrum.*, 87(4):043508, 2016.
- [152] Roman Schrittwieser, Codrina Ionita, Petru Balan, Ramona Gstrein, Olaf Grulke, Thomas Windisch, Christian Brandt, Thomas Klinger, Ramin Madani, George Amarandei, and Arun K. Sarma. *Rev. Sci. Instrum.*, 79(8):083508, 2008.
- [153] Richard A. Gottscho and Mary L. Mandich. *J. Vac. Sci. Technol.*, 3(3):617–624, 1985.
- [154] M. J. Goeckner, Shamim M. Malik, J. R. Conrad, and R. A. Breun. *Phys. Plasmas*, 1(4):1064–1074, 1994.
- [155] H Kersten, H Deutsch, M Otte, G.H.P.M Swinkels, and G.M.W Kroesen. *Thin Solid Films*, 377-378:530 – 536, 2000. International Conference on Metallurgic Coatings and Thin Films.
- [156] R Basner, F Sigeneger, D Loffhagen, G Schubert, H Fehske, and H Kersten. *New J. Phys.*, 11(1):013041, 2009.

-
- [157] A A Samarian and B W James. *Plasma Phys. Control. Fusion*, 47(12B):B629, 2005.
- [158] Peter Hartmann, Anikó Zs Kovács, Jorge C Reyes, Lorin S Matthews, and Truell W Hyde. *Plasma Sources Sci. Technol.*, 23(4):045008, 2014.
- [159] B. M. Annaratone, T. Antonova, H. M. Thomas, and G. E. Morfill. *Phys. Rev. Lett.*, 93:185001, Oct 2004.
- [160] G Schubert, M Haass, T Trottenberg, H Fehske, and H Kersten. *Contrib. Plasma Phys.*, 52(10):827–835, 2012.
- [161] Sergey V Vladimirov, Kostya Ostrikov, and Alex A Samarian. *Physics and applications of complex plasmas*. World Scientific, 2005.
- [162] G. Schubert, R. Basner, H. Kersten, and H. Fehske. *Eur. Phys. J. D*, 63(3):431–440, Aug 2011.
- [163] B M Annaratone, M Glier, T Stuffer, M Raif, H M Thomas, and G E Morfill. *New J. Phys.*, 5(1):92, 2003.
- [164] Edward Thomas Jr. *Phys. Plasmas*, 8(1):329–333, 2001.
- [165] Edward Thomas Jr. *Phys. Plasmas*, 9(1):17–20, 2002.
- [166] Edward Thomas Jr. *IEEE Trans Nucl Sci.*, 30(1):88–89, 2002.
- [167] Edward Thomas Jr. *New J. Phys.*, 5(1):45, 2003.
- [168] Edward Thomas Jr, Jeremiah D Williams, and Jennifer Silver. *Phys. Plasmas*, 11(7):L37–L40, 2004.
- [169] Edward Thomas Jr. *Phys. Plasmas*, 13(4):042107, 2006.

-
- [170] S. Jaiswal, P. Bandyopadhyay, and A. Sen. *Rev. Sci. Instrum.*, 86(11):113503, 2015.
- [171] J Goree. *Plasma Sources Sci. Technol.*, 3(3):400, 1994.
- [172] De-Bo Huang, OJ Sibul, WC Webster, JV Wehausen, De-Ming Wu, and TY Wu. Ships moving in the transcritical range. In *Proc. Conf. on Behaviour of Ships in Restricted Waters, Varna, Bulgaria*, pages 26–1, 1982.
- [173] RC ERTEKIN. Ship-generated solitons. *Proc 15th Symp on Naval Hydrodynamics, Hamburg, Germany, Aug 1985*, 1985.
- [174] RC Ertekin, WC Webster, and JV Wehausen. Waves caused by a moving disturbance in a shallow channel of finite width. *Journal of Fluid Mechanics*, 169:275–292, 1986.
- [175] Hung-Lung A Huang. *Dynamics of surface waves in coastal waters*. Springer, 2010.
- [176] A. Barkan, R. L. Merlino, and N. D’Angelo. Laboratory observation of the dust-acoustic wave mode. *Physics of Plasmas*, 2(10):3563–3565, 1995.
- [177] NN Rao and PK Shukla. Nonlinear dust-acoustic waves with dust charge fluctuations. *Planetary and Space Science*, 42(3):221–225, 1994.
- [178] G. E. Morfill, H. M. Thomas, U. Konopka, H. Rothermel, M. Zuzic, A. Ivlev, and J. Goree. Condensed plasmas under microgravity. *Phys. Rev. Lett.*, 83:1598–1601, Aug 1999.
- [179] A Usachev, A Zobnin, O Petrov, V Fortov, M Thoma, M Kretschmer, S Ratynskaia, R Quinn, H Hoefner, and G Morfill. The project

- “plasmakristall—4”(pk-4)—a dusty plasma experiment in a combined dc/rf (i) discharge plasma under microgravity conditions. *Czechoslovak Journal of Physics*, 54(3):C639, 2004.
- [180] Lu-Jing Hou, Z. L. Mišković, Ke Jiang, and You-Nian Wang. Energy loss of a charged particle moving over a 2d strongly coupled dusty plasma. *Phys. Rev. Lett.*, 96:255005, Jun 2006.
- [181] Garima Arora, P. Bandyopadhyay, M. G. Hariprasad, and A. Sen. Microdynamics of neutral flow induced dusty plasma flow. *Physics of Plasmas*, 26(2):023701, 2019.
- [182] Garima Arora, P. Bandyopadhyay, M. G. Hariprasad, and A. Sen. A dust particle based technique to measure potential profiles in a plasma. *Physics of Plasmas*, 25(8):083711, 2018.
- [183] AL New and RD Pingree. Large-amplitude internal soliton packets in the central bay of biscay. *Deep Sea Research Part A. Oceanographic Research Papers*, 37(3):513–524, 1990.
- [184] M Gedalin, TC Scott, and YB Band. Optical solitary waves in the higher order nonlinear schrödinger equation. *Physical review letters*, 78(3):448, 1997.
- [185] Hermann A Haus and William S Wong. Solitons in optical communications. *Reviews of modern physics*, 68(2):423, 1996.
- [186] Stephane Barland, Jorge R Tredicce, Massimo Brambilla, Luigi A Lugiato, Salvador Balle, Massimo Giudici, Tommaso Maggipinto, Lorenzo Spinelli, Giovanna Tissoni, Thomas Knoedl, et al. Cavity solitons as pixels in semiconductor microcavities. *Nature*, 419(6908):699, 2002.

-
- [187] Barland Stephane, Jorge R Tredicce, Brambilla Massimo, Luigi A Lugiato, Balle Salvador, Giudici Massimo, Maggipinto Tommaso, Lorenzo Spinelli, Tissoni Giovanna, Knödl Thomas, et al. Cavity solitons as pixels in semiconductor microcavities. *Nature*, 419(6908):699–702, 2002.
- [188] Norman J Zabusky and Martin D Kruskal. Interaction of "solitons" in a collisionless plasma and the recurrence of initial states. *Physical review letters*, 15(6):240, 1965.
- [189] Sita Sundar, Amita Das, Vikrant Saxena, Predhiman Kaw, and Abhijit Sen. Relativistic electromagnetic flat top solitons and their stability. *Physics of Plasmas*, 18(11):112112, 2011.
- [190] Atul Kumar, Chandrasekhar Shukla, Deepa Verma, Amita Das, and Predhiman Kaw. Excitation of kdv magnetosonic solitons in plasma in the presence of an external magnetic field. *Plasma Physics and Controlled Fusion*, 61(6):065009, 2019.
- [191] Diederik Johannes Korteweg and Gustav De Vries. Xli. on the change of form of long waves advancing in a rectangular canal, and on a new type of long stationary waves. *The London, Edinburgh, and Dublin Philosophical Magazine and Journal of Science*, 39(240):422–443, 1895.
- [192] Robert M Miura. The korteweg–devries equation: A survey of results. *SIAM review*, 18(3):412–459, 1976.
- [193] Hiroyuki Ikezi. Experiments on ion-acoustic solitary waves. *The Physics of Fluids*, 16(10):1668–1675, 1973.

-
- [194] John N. Dinkel, Claude Setzer, Sunil Rawal, and Karl E. Lonngren. Soliton propagation and interaction on a two-dimensional nonlinear transmission line. *Chaos, Solitons , Fractals*, 12(1):91 – 96, 2001.
- [195] Seung-Joon Lee, George T Yates, and T Yaotsu Wu. Experiments and analyses of upstream-advancing solitary waves generated by moving disturbances. *Journal of Fluid Mechanics*, 199:569–593, 1989.
- [196] Benjamin J. Binder, Mark G. Blyth, and Sanjeeva Balasuriya. Non-uniqueness of steady free-surface flow at critical froude number. *EPL (Europhysics Letters)*, 105(4):44003, 2014.
- [197] P. Bandyopadhyay, G. Prasad, A. Sen, and P. K. Kaw. *Phys. Rev. Lett.*, 101:065006, Aug 2008.
- [198] D. A. Law, W. H. Steel, B. M. Annaratone, and J. E. Allen. *Phys. Rev. Lett.*, 80:4189–4192, May 1998.
- [199] A Usachev, A Zobnin, O Petrov, V Fortov, M H Thoma, H Höfner, M Fink, A Ivlev, and G Morfill. Externally excited planar dust acoustic shock waves in a strongly coupled dusty plasma under microgravity conditions. *New Journal of Physics*, 16(5):053028, 2014.
- [200] RS Steinolfson and S Cable. Venus bow shocks at unusually large distances from the planet. *Geophysical research letters*, 20(8):755–758, 1993.
- [201] JT Gosling, JR Asbridge, SJ Bame, and IB Strong. Vela 2 measurements of the magnetopause and bow shock positions. *Journal of Geophysical Research*, 72(1):101–112, 1967.

-
- [202] AA Vidotto, J Llama, M Jardine, Ch Helling, and K Wood. Shock formation around planets orbiting m-dwarf stars. *Astronomische Nachrichten*, 332(9-10):1055–1061, 2011.
- [203] Benjamin Tadsen, Franko Greiner, and Alexander Piel. On the amplitude of dust-density waves in inhomogeneous dusty plasmas. *Physics of Plasmas*, 24(3):033704, 2017.
- [204] T. M. Flanagan and J. Goree. Observation of the spatial growth of self-excited dust-density waves. *Physics of Plasmas*, 17(12):123702, 2010.
- [205] G. B. Whitham. *Linear and Nonlinear Waves*. Wiley, New York, 1974.
- [206] Mangilal Choudhary, S Mukherjee, and P Bandyopadhyay. Propagation characteristics of dust–acoustic waves in presence of a floating cylindrical object in the dc discharge plasma. *Physics of Plasmas*, 23(8):083705, 2016.
- [207] Jeremiah D Williams. Spatial evolution of the dust-acoustic wave. *IEEE Transactions on Plasma Science*, 41(4):788–793, 2012.
- [208] MG Hariprasad, P Bandyopadhyay, Garima Arora, and A Sen. Experimental observation of a dusty plasma crystal in the cathode sheath of a dc glow discharge plasma. *Physics of Plasmas*, 25(12):123704, 2018.
- [209] SV Annibaldi, AV Ivlev, U Konopka, S Ratynskaia, HM Thomas, GE Morfill, AM Lipaev, VI Molotkov, OF Petrov, and VE Fortov. Dust-acoustic dispersion relation in three-dimensional complex plasmas under microgravity. *New Journal of Physics*, 9(9):327, 2007.
- [210] S. K. Sharma, A. Boruah, and H. Bailung. *Phys. Rev. E*, 89:013110, Jan 2014.

- [211] SV Singh and NN Rao. Linear and nonlinear dust-acoustic waves in inhomogeneous dusty plasmas. *Physics of Plasmas*, 5(1):94–99, 1998.
- [212] SV Singh and NN Rao. Effect of dust charge inhomogeneity on linear and nonlinear dust–acoustic wave propagation. *Physics of Plasmas*, 6(8):3157–3162, 1999.

Thesis Highlight

Name of the Student: Garima Arora

Name of the CI/OCC: Institute for Plasma Research, Gandhinagar

Enrolment No.: PHYS06201504004

Thesis Title: Laboratory studies of stationary and non-stationary structures in flowing complex plasmas

Discipline: Physical Sciences

Sub-Area of Discipline: Plasma Physics

Date of viva voce: 3th September, 2020

In this thesis work, the experimental excitation of non-linear waves in a flowing complex plasma is investigated. These experiments are carried out in the Dusty Plasma Experimental (DPEX) device in

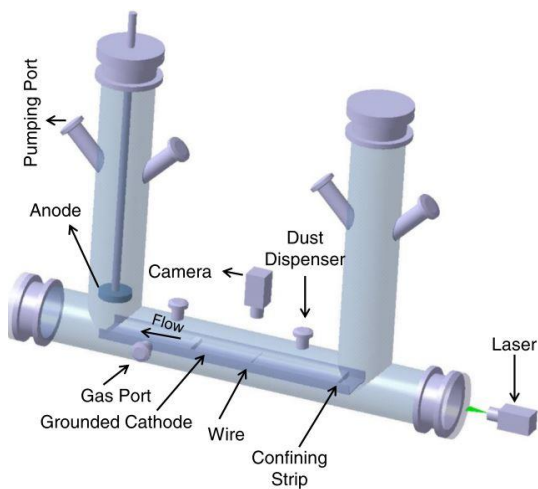


Fig. Schematic of Dusty Plasma Experimental (DPEX) device

which a DC glow discharge Argon plasma is produced in between a circular anode and a grounded tray cathode as shown in Fig 1. A dusty plasma is then generated either using mono-dispersive MF particles or poly-dispersive Kaolin particles. The flow in the dust fluid ranging from subsonic to supersonic is generated over a charged object using different techniques. Subsonic flow of dust fluid generates normal wake patterns whereas a slightly supersonic flow leads to excitations of various structures in the fore-wake region called precursor solitons. The shape and size of the charged object plays an important role to determine the characteristics of the precursor solitons and there exists a threshold value of object height below which the dust fluid simply flows over the object

without exciting any nonlinear structures. The measurement of shape and size of the charged object is done by new technique called dust as a dynamic microprobe. Generation of highly supersonic flow changes the complete dynamics of fore wake structures which leads to the excitation of stationary structures called pinned solitons (see Fig. 2(a)), which remains attached with the object from the frame of fluid. The experimental findings of precursor and pinned solitons are qualitatively compared with the numerical model of the forced-KdV equation. The study of nonlinear structure (shown in Fig. 2(b)) in an inhomogeneous dusty plasma is also carried out by investigating the propagation characteristics (amplitude, width and velocity) of shock waves when they travel downhill along a density gradient. The modified-KdV-Burger equation is derived for such a case and numerically solved for a dusty plasma medium with a dust density gradient and where the dissipation effect comes from the strong coupling induced viscosity as well as neutral damping.

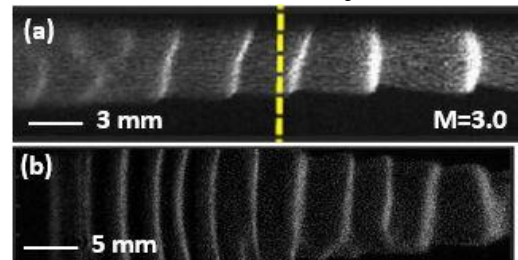


Fig-2 Experimental images of (a) pinned solitons and (b) shock waves